SCUOLA DI DOTTORATO

UNIVERSITÀ DEGLI STUDI DI MILANO-BICOCCA

Department of

Physics

PhD program in Physics and Astronomy Cycle XXXI

Curriculum in Plasma physics

Fast neutron-based instruments for application to fusion and spallation sources

Surname: Feng Name: Song

Registration number: 811340

Tutor: Dr. Marco Tardocchi

Co-tutor: Prof. Giuseppe Gorini

Coordinator: Prof. Marta Calvi

ACADEMIC YEAR 2017/2018

Two roads diverged in a wood, and I–
I took the one less traveled by,
And that has made all the difference.
– Robert Frost

Abstract

As the increasing interest in MeV range neutrons for applied physics studies, the development of dedicated fast neutron-based instruments, which have the capabilities to deal with complex background and to measure high counting rate (MHz), is demanded. Fast neutron measurements are especially playing key roles in plasma diagnostics on thermonuclear fusion experiments and in study of neutron damage at spallation sources, on which neutrons are produced by the DD or DT fusion reactions and by spallation reactions with high energy protons incident on heavy target, respectively.

This thesis presents the development both on a fast response scintillation detector that has been developed as a neutron emission monitor for deuterium beam diagnostics on large current negative beam test facility (like ELISE and SPIDER), and on the design and test of Telescope Proton Recoil (TPR) neutron spectrometers dedicated for neutron spectrum measurements on the fast neutron beam line ChipIr at ISIS. These instruments have been studied at accelerator-based platforms, tested at the ISIS spallation neutron source, as well as been applied in dedicated experiments on ELISE. Development of the two types of fast neutron-based instruments in applications to fusion and spallation neutron sources are presented in the following two parts:

(1). Measurement of the deuterium beam-target neutron emission that occurs when the deuterium beam penetrates in the metallic dump of the NBI (neutral beam injection) prototype has been proposed as a means of diagnostics on beam homogeneity at SPIDER and MITICA. In order to derive the deuterium beam profile by measuring the produced neutrons from the $D(d,n)^3He$ reactions between the deuterium beam and deuterons previously implanted in the beam dump, a relative model should be built to predict the neutron emission based on understanding the process of deuterium implantation in dump, and to aid the CNESM detection system which is based on the GEM technique for beam profile diagnostics in SPIDER. To this end, a calibrated EJ301 liquid scintillation detector has been developed and used on ELISE to measure the time trace of neutron emission and to benchmark calculations based on the Local Mixing Model (LMM), which has been successfully applied to describe the deuterium implantation in the dump. The scintillation detector shows good capabilities on neutron/gamma-rays discrimination and radioactive resistance. By relatively comparing with the measurements of neutron emission on ELISE, LMM based calculations by employing diagnostics of the Infra-red (IR) camera and calorimeter have been found showing an overestimation of neutron emission in beam power range up to 950 kW, which is approaching the maximum capabilities allowed by the ELISE facility and towards the beam power expected at SPIDER. The quantitative determination of the discrepancy, which might be resulted by diffusion effects beyond the so far LMM, has been confirmed. An empirical correction, which is based on the temperature difference of the dump and could be applied for the neutron diagnostics at SPIDER, has been derived. In particular, a similar liquid scintillator will be installed at SPIDER as a neutron emission monitor.

(2). On the atmospheric-like fast neutron beam-line ChipIr, which is designed for electronics radiation studies (e.g. single event upset, SEU) at ISIS, direct measurement of the neutron spectrum and flux distribution could be used for characterizing the neutrons profile and benchmarking the simulations. As the challenges of high intensity neutrons (>10^6 n·cm^{-2}·s^{-1} with $E_n > 10$ MeV), wide energy range and complex background, TPR neutron spectrometers have been proposed as an effective way by applying the $\Delta E - E$ technique and coincidence analysis. In this thesis, two types of TPR spectrometers based on silicon detectors (silicon-based TPR) and a YAP scintillator together with silicon detectors (scintillator-based TPR), respectively, have been designed and tested. The two prototypes of scintillator-based TPR, which were designed for long-term measurements as the good radioactive resistance of YAP scintillators, are consisting of a silicon detector and a 2.54 cm thick YAP scintillator, and two silicon detectors and a 2.54 cm thick YAP scintillator (triple coincidence TPR), respectively. The response of the used YAP scintillator to protons has been studied up to 80 MeV with the cyclotron accelerator at the INFN-LNS. Two scintillator-based prototypes have been tested on ChipIr and ROTAX beam line, respectively. Very serious pulses pile-up effect was found on the YAP crystal (>70%) on the ChipIr beam line. With the collimator installed on the ROTAX beam line for incident neutrons, the triple coincidence TPR shows a good capability on charged particles discrimination and background suppression. The prototype of silicon-based TPR, which consists of four silicon detectors, has been tested on the ROTAX beam line. The recoil proton spectrum using the silicon-based TPR prototype on the ROTAX beam-line has been obtained. Results show the possible of high intense neutrons measurements by using the silicon-based TPR for its high coincident ability and non-sensitively to background (especially γ -rays).

List of publications

This thesis is based on the following papers, which are referred to in the text by their Roman numerals:

I) M. Nocente, **S. Feng**, D. Wünderlich, F. Bonomo, G. Croci, U. Fantz, B. Heinemann et al. Experimental investigation of beam-target neutron emission at the ELISE neutral beam test facility. *Fusion Engineering and Design* **123** (2017): 843-846.

II) **S. Feng**, M. Nocente, D. Wünderlich, F. Bonomo, G. Croci, U. Fantz, B. Heinemann, W. Kraus, I. Mario, A. Muraro, R. Pasqualotto, M. Rebai, M. Tardocchi and G. Gorini. Neutron measurements at the ELISE neutral beam test facility and implications for neutron based diagnostics at SPIDER. *Review of Scientific Instruments*, **89** (2018): 10I139.

III) **S. Feng**, C. Cazzaniga, T. Minniti, M. Nocente, C. Frost, G. Gorini, A. Muraro, S. Romano, and M. Tardocchi. Response of a telescope proton recoil spectrometer based on a YAP: Ce scintillator to 5–80 MeV protons for applications to measurements of the fast neutron spectrum at the ChipIr irradiation facility. *Nuclear Instruments and Methods in Physics Research Section A: Accelerators, Spectrometers, Detectors and Associated Equipment.* **912** (2018): 36–38.

Contents

Chapter 1

Introduction

> *If the radiance of a thousand suns were to burst into the sky,*
> *that would be like the splendor of the mighty One...*
> *...I am become Death, the shatterer of worlds.*
> – – "The Bhagavad-Gita"
> *J. Robert Oppenheimer quoted after the first atomic bombing*

1.1 Needs for fast neutron measurements

The neutron (symbol n), which was discovered by James Chadwick in 1932 [1], is a subatomic particle with a mass slightly larger than that of a proton. Free neutrons are produced by nuclear processes and nowadays are utilized not only in fundamental research, but also for energy production, nuclear non-proliferation, therapy of cancer, imaging, material analysis, etc. In somewhat of an oversimplification, we divide neutrons into two categories on the basis of their energy, either "fast neutrons" or "slow neutrons". The energy dividing line is based on reference [2], i.e. at about 0.5 eV, or about the energy of the abrupt drop in absorption cross section in cadmium (the cadmium cutoff energy). As the fast neutrons, they have been produced and utilized by human to a lot of applications. For instance,

- for energy production. Fast neutron reactors [3], fusion reactor systems [4] and the accelerator driven systems (ADSs) [5, 6] are getting more and more attractions. Nuclear waste from fission reactors could be transmuted by those fast neutron-based advanced systems with which long-term demanding on energy can be satisfied and very low CO_2 will be produced at the same time;

- for radiation hardness studies [7]. Fast neutrons are usually produced by spallation reactions to mimic the atmospheric neutron spectrum with high intensity for single event effects (SEEs) study, which is usually caused by neutrons and results in the micro-electronic devices failure;
- for cancer therapy [8–10]. Fast neutron radiotherapy is entering a new era in which dedicated hospital-based generators with isocentric beam capability are replacing treatment facilities based on fixed beams extracted from physics accelerators;
- for nuclear non-proliferation [11–14]. Fast neutron imaging technique is applied for checking nuclear materials or explosives in arms control and nonproliferation applications;
- for cross section measurements [15]; The subject of the interaction of neutrons with matter contains an astonishing diversity of phenomena. The measure of the interaction of neutrons with matter is the neutron cross section, and the great range of phenomena is reflected in the range of types of cross sections that can be measured. Therefore, the measurements of neutron induced reactions play a fundamental role in nature, especially for astrophysics and nuclear technology.

As neutrons carry no net electric charge (experimental limits: $(-2 \pm 8) \times 10^{-22}$ e [16]), therefore, on one hand, they cannot be accelerated by electric field; on the other hand, they can be totally invisible to a detector of common size [2]. Because neutrons cannot interact in matter by means of the coulomb force, which dominates the energy loss mechanisms for charged particles and electrons, thus considering the small volume of nuclei they usually have deep penetration in matter. Specific description of the interaction of neutrons with matter and the means of detection we used in this thesis are detailed in chapter 2.

With the increasing interest in MeV range neutrons for applied physics studies, the development of dedicated fast neutron-based instruments, which has the capabilities to deal with complex background and to measure high counting rate (MHz), is demanded. Fast neutron measurements are especially playing key roles in plasma diagnostics on thermonuclear fusion experiments and in study of neutron damage at spallation sources, on which neutrons are produced by the deuterium-deuterium (DD) or deuterium-tritium (DT) fusion reactions and by spallation reactions with high energy protons incident on heavy target, respectively. In this thesis, we encompass both on fast response scintillator-based detectors to measure the time trace of neutron emission on high current/intensity negative beam test facility (like ELISE or SPIDER), and on the design and test of

Telescope Proton Recoil (TPR) neutron spectrometers dedicated for neutron spectrum measurements on the fast neutron beam line ChipIr at ISIS.

The background and the aims of developing the two kinds of neutron-based instruments in applications to fusion and spallation neutron sources are presented in the following two sections.

1.2 Fast neutrons as neutral beam injector diagnostics

1.2.1 Magnetic confinement fusion and the tokamak

Nuclear energy can be released not only from the fission of heavy nuclei but also from the fusion of light nuclei. Nuclear fusion is an important option for a clean and safe solution for our long-term energy needs. The quest for controlled fusion energy has been ongoing for over a half century. In conceptual designs, controlled nuclear fusion can be achieved in many ways which are mostly based on the tokamak device, the theta pinch, the magnetic mirror and the laser-pellet inertial-confinement system [4, 17]. The extremely required high temperature or high density for the fusion reaction have been routinely achieved in several magnetic-fusion machines [18–26] and also in laser-driven inertial-confinement fusion systems [27–29].

To realize fusion on earth much higher reaction probabilities are needed – reactions between isotopes of hydrogen and helium have this property. The simplest of these is the so-called deuterium-tritium (DT) reaction which can be realized at temperatures around 150 million °C, for instance, in tokamak. The magnetic approach dates into the 1940s and has seen the majority of development since then. It is usually considered more promising for practical power production. A charged particle in a strong magnetic field is bound to the magnetic field lines as a result of the Lorentz force. In a straight and uniform magnetic field, it follows a helical (corkscrew) path around a field line. This motion can be split into a circular motion, with a radius of gyration (also known as the Larmor radius) and a linear motion of the centre of the circle (the guiding centre), with a velocity along the field line. The simplest magnetic field geometry one can think of for plasma confinement is that of a straight cylinder. However, this geometry has the problem that plasma particles escape at both ends. Since the early days of controlled fusion research, a lot of schemes have been in use to generate the rotational transform [30]: the tokamak, the stellarator, the mirror machine, Z-pinch, etc.

The tokamak configuration [31] has essentially undergone a selection process culminating in the ITER device, a fusion device with a planned fusion power output of 500 MW in pulses of 400 s, and future demonstration (DEMO) reactor designs. ITER should provide answers to remaining important questions on the integration of physics and technology, through a full-size demonstration of a tenfold power multiplication, and on nuclear safety aspects.

1.2.2 Neutral beam injectors and the test facilities for ITER

As the limitation of technology to confine the plasma well, the plasma density is quite low in tokamak compared the one in stars (like sun). In order to reach energy balance in tokamak, the hot plasma must be sustained at extreme temperatures in a controlled way to make enough fusion reactions happened and to extract enough energy, which is ruled by the Lawson's criterion [32]. As the confined plasma cannot be heated to the temperatures needed for occurring enough fusion reactions with only the Ohmic heating since its heating efficiency decreases with increasing temperature, auxiliary heating systems are needed. Neutral beam injection (NBI) is one of the ways to heat the plasma by shooting uncharged high-energy particles into the plasma where, by way of collision, they transfer their energy to the plasma particles. At the same time, the NBI system could provide the needed fuel for plasma.

The process of neutral beam injection in tokamak is that: ionize atoms to positive or negative particles; accelerate charged particles by electric field; then neutralize them and deflect un-neutralized particles, otherwise the charged ions would be deflected by the magnetic field of the plasma cage. In neutral beam injection systems, the ions pass through a cell containing gas where they recover their missing electrons and then be injected as fast neutral particles into the plasma, as ilustrated in figure 1.1 (a).

The required power for ITER NBI systems is about 33 - 50 MW (16.5 MW × 2 or 3 injectors). Each NBI accelerates a 40 A beam of negative deuterons to 1 MeV, and delivers neutralised deuterium to the plasma up to one hour [35, 36]. In order to obtain so high beam energy the use of negative ions is mandatory. This is because the neutralisation efficiency of positive ions drops significantly with increasing energy, while it remains at acceptable values for negative ions, which can be found in the experimental investigation as shown in figure 1.1 (b). However, there is no experience by now to accelerate negative ions to such high energy with such high current. In order to

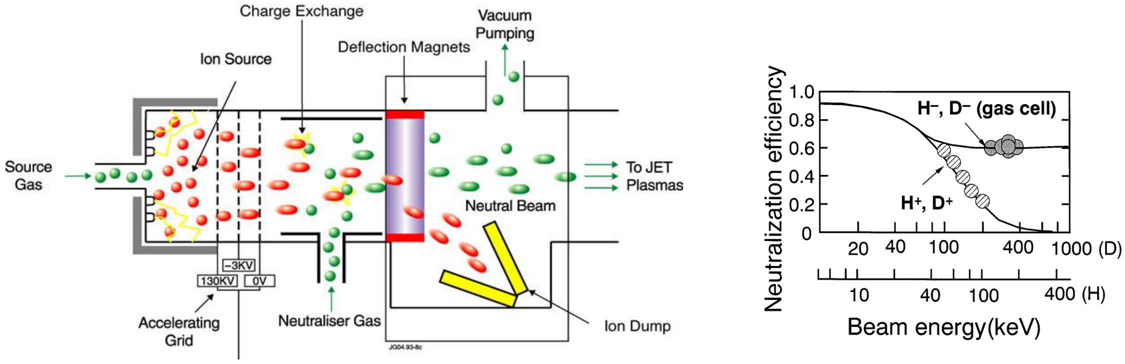

(a) **(b)**

Figure 1.1: (a): Schematic of the NBI operating principle in JET, extracted from ref. [33]; (b): Neutralisation efficiency for hydrogen ions as a function of energy, extracted from ref. [34].

investigate challenging physics and technology issues in advance of the installation of the neutral beam equipment at ITER, the ITER Neutral Beam Test Facility (NBTF), called PRIMA (Padova Research on ITER Megavolt Accelerator), is underway in Padova, Italy [37, 38].

1.2.3 Diagnostics of deuterium beam divergence with neutrons

PRIMA [39] includes the negative ion source SPIDER (Source for Production of Ion of Deuterium Extracted from Rf plasma) and the full power injector MITICA (Megavolt ITER Injector & Concept Advancement). SPIDER will have to demonstrate extracted current density of $> 285 A/m^2$, with co-extracted electron fraction < 1 in deuterium and ±10% uniformity. MITICA will also have to achieve ≤ 7 mrad divergence. Proper operation of source and accelerator is verified mainly by measuring the beam properties. Inside this challenging development path it is proving essential to well diagnose the accelerated beam, in particular to estimate the beam uniformity and divergence from its intensity profile. Overall injector performance can then be studied by correlating the physics of the source with the beam characteristics in the actual NBI geometry, investigating the optimum operational space.

A set of beam diagnostics [40,41] has been designed for SPIDER including the cooling water calorimetry, a short pulse instrumented calorimeter, beam emission spectroscopy, visible tomography, and neutron imaging. The neutron imaging detection system, called CNESM (Close-contact Neutron Emission Mapping) [42], is under development with the aim to resolve the horizontal beam intensity profile in MITICA and one of the eight beamlets groups in SPIDER. This is achieved by the evaluation of the neutron emission due to interaction of the deuterium beam with the deuterons implanted in the beam dump surface [43–46]. The CNESM detection system, which is based on GEM (gas electron multiplier) technology especially designed to provide a spatial resolution approaching the size of individual beamlets, will be placed right behind the SPIDER and MITICA beam dump [47–50], as shown in figure 1.2. By detecting the produced neutrons in the beam penetration direction, the beam intensity map on the dump can be derived, which is useful for diagnostic on beam divergence.

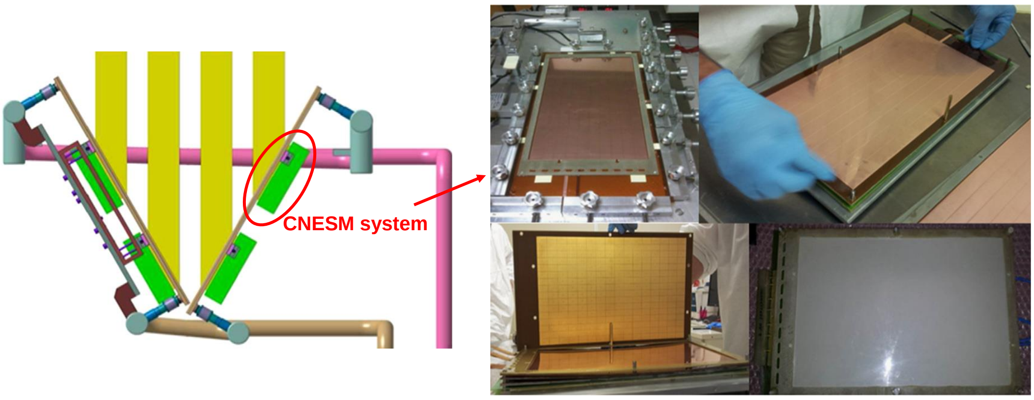

Figure 1.2: Left: Schematics of the SPIDER beamdump (Top view). The beam dump is tilted by 60° relative to the beam axis (yellow). The CNESM detectors (green) are placed right behind the beam dump; Right: Assembly of the detector. Both figures are extracted from ref. [49].

In SPIDER, CNESM will be benchmarked by STRIKE, an inertially cooled calorimeter as the main diagnostics for the beam profile mainly based on Infra-red (IR) measurements. As IR measurements cannot be used on MITICA due to engineering constraints, the experience gained at SPIDER will be instrumental to make CNESM the reference system for deuterium beam profile measurements on MITICA. As what the CNESM system measure is the intensity of neutrons produced from deuterium beam-target reactions, in order to obtain the intensity of incident deuterium beam and aid the detector development, the physics behind neutron emission from the D(d, n)^{3}He beam-target reactions by impinging large current (tens of ampere) negative deuterium ions on must be investigated first. This is one of tasks in this thesis. We firstly developed a scintillator-based neutron detector to measure the time trace of neutron emission from the beam-target reaction at the ELISE (Extration from a Large Ion Source Experiment) test facility, and then applied a model to describe the deuterium implantation in dump and calculated the neutron emission for relatively comparing with measurements. The detailed configuration of the deuterium beam-target experiment and its application for beam diagnostics on SPIDER have been introduced in chapter 3.

1.3 Fast neutrons for radiation hardness studies at spallation sources

Galactic cosmic rays and solar rays constantly penetrate the earth's atmosphere and produce particle cascades, consisting mainly of neutrons [51], which can interact with the silicon structure in a semiconductor device and cause adverse behavior. Figure 1.3 (left) shows the interaction of primary rays with atmosphere and the produced secondary particles. The main contribution of the secondary particles is neutron and its share increase with decreasing altitude, as shown in the right panel of figure 1.3.

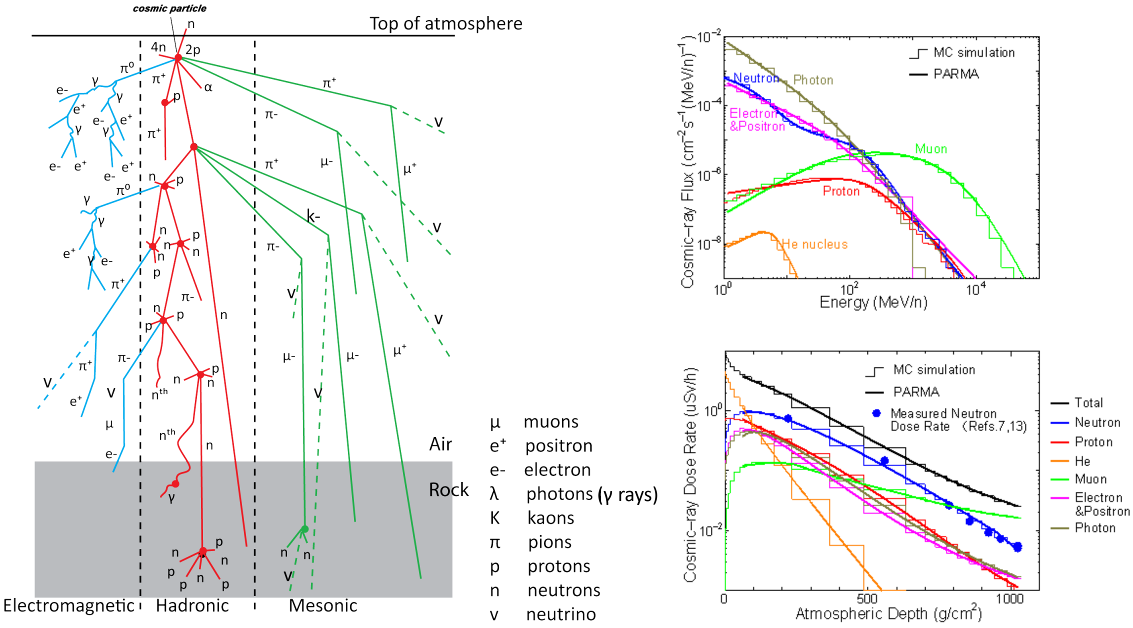

Figure 1.3: Left: Schematics of the interaction of cosmic rays with atmosphere and the produced secondary particles [52]; Right: Altitude dependence of cosmic-ray dose rates in Tokyo [53].

The energy level associated with these atmospheric neutrons are considered high energy, i.e. above 1 MeV and up to a few GeV [54, 55]. Such neutrons have been associated with causing Single Event Effects (SEEs) in electronics which is now a known safety and reliability issue for avionics equipment [56–58]. In recent years microelectronics devices and systems are towarding high intensity, faster and more functionality. Greater vulnerability, combined with an ever greater prevalence of embedded microelectronic devices, has meant that SEEs problems have started to inevitably emerge as a serious issue for terrestrial ground based electronics [59,60]. The effects of atmospheric radiation at both the component and system levels is necessary to be evaluated experimentally and used as an input into the system safety analysis. As the neutron intensity at ground level is too low for SEEs study, e.g. the atmospheric neutron flux is 300 times greater at typical aircraft altitudes with respect to the ground level, the electronics industry has therefore been increasing demanding the use of intense accelerator-based neutron facilities in which a few hours test equals many thousands of hours in the real environment. Currently, several neutron test facilities are in operation [61, 62] (e.g. ICE House of LANSCE [63], TRIUMF (Tri-University Meson Facility) in Canada [64], ANITA (Atmospheric-like Neutrons from thIck TArget) neutron facility in Uppsala, Sweden [65], the 30-deg white neutron beam at RCNP cyclotron facility [66]) or in design (e.g. the atmospheric-like neutron beam line at CSNS [67, 68], a new beam-line proposed at the Oak Ridge National Laboratory [55,69]) to quantify the susceptibility of a device to atmospheric radiation and in the parts selection process. In order to mimic the high intensity atmospheric neutron spectrum as similar as possible, a spallation neutron source is usually needed [62].

1.3.1 The ISIS spallation neutron source

Spallation reaction is a process in which a light projectile (proton, neutron, or light nucleus) with the kinetic energy from several hundreds of MeV to several GeV interacts with a heavy nucleus (e.g., lead) and causes the emission of a large number of hadrons (mostly neutrons) or fragments. The number of neutrons produced per one beam particle is called multiplicity. Neutron multiplicity as a function of the proton beam energy and target material shows roughly linear dependence on the target mass number A (in the range $12 < A < 238$) and slow increase with incident proton energy E_p (in the range $0.2 < E_p < 2$ GeV) [70]. The average neutron multiplicities are about 21 and 118 for 1 GeV and 7 GeV protons incident on lead [71], respectively. As the high neutron production of spallation neutron sources, increasing interest has been noticed during the past 30 years [72]. Currently operating pulsed spallation neutron sources are: ISIS in UK (1985), SINQ in Switzerland (1996), JSNS in Japan (2008), SNS in USA (2010), and CSNS in China (2017). Combined with state-of-the-art neutron instrumentation, they have a diverse potential for both scientific research and diverse applications.

ISIS neutron source is a pulsed neutron source which is situated at the Rutherford Appleton Laboratory (RAL) of the Science and Technology Facilities Council (STFC) in UK. Neutrons here are produced by proton-induced spallation on a Tungsten-Tantalum target. Incident protons are in two bunches, 70 ns wide and 322 ns apart, and are accelerated through a Linac and a synchrotron up to 800 MeV with a frequency of 50 Hz. Produced neutrons are moderated and are focused into the various beam lines. The nature of the moderators is different from one beam-line to another so that they provide a neutron spectrum specific for each beam-line. There are a lot of instruments currently on the target station 1 and 2 to perform experiments in diverse science areas such as physics, chemistry, materials engineering, earth sciences, biology and archaeology. In order to study the fast neutron irradiation hardness, tests have previously been performed on the VESUVIO beam-line, and now a new beam-line, ChipIr [61], is in operation [73,74].

1.3.2 ChipIr: a dedicated fast neutron facility for accelerated SEE testing

The new beam-line ChipIr has been built on the target station 2 at the ISIS neutron source of the RAL for neutron irradiation experiments on electronic and avionic devices and systems [61,75]. ChipIr is dedicated to provide a fast neutron spectrum that mimics the atmospheric one with approximately $10^8 - 10^9$ times higher intensity at ground level [76]. Like every beam line at the ISIS neutron source, ChipIr has an independent shutter so that its neutron beam can be closed and opend while the accelerator is running. The shutter position therefore has been optimized to provide the maximum neutron flux. The LANSCE-equivalent fluency rate at ChipIr was measured to be 4.9×10^6 $\mathrm{cm^{-2} \cdot s^{-1}}$ at 40 μA proton current to Target station 2 with collimated beam size of 70 × 70 $\mathrm{mm^2}$, reproducible to within 3% [60]. This is a relative measurement with respect to LANSCE, which is a reference irradiation facility for electronics cited in JEDEC [77] and IEC [78, 79] standards. Figure 1.4 shows the calculated fast neutron spectrum of ChipIr compared to LANSCE and the atmospheric one increased by a factor of 10^9. Here the spectral shape comes from Monte Carlo simulations, but the intensity comes from the value measured with the ISEEM [60] and activation foils [80].

Independent direct measurements of the neutron spectrum on the ChipIr beam line are needed because as far the neutron energy spectrum and the flux spatial distribution of

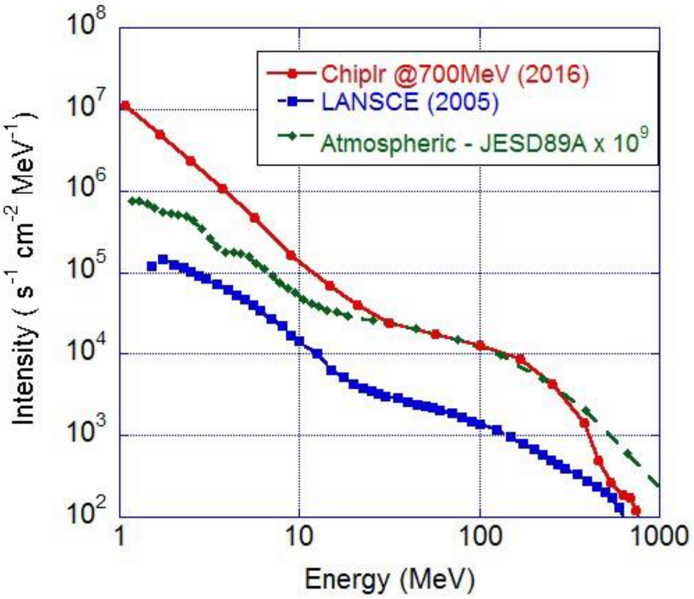

Figure 1.4: Neutron spectrum of ChipIr compared with the atmospheric and LANSCE spectra. Extracted from ref. [60].

fast neutron beam-lines are mainly determined on the basis of Monte Carlo calculations that try to reproduce the complexity of nuclear and intra-nuclear interactions up to 800 MeV. Direct measurements of these quantities could characterize the neutron flux distribution and neutron spectrum, for providing users a “real time” measured neutron spectrum (also flux), benchmarking the simulations, and for a better understanding of the underlying physics of this kind of facilities. To this end, a telescope proton recoil neutron spectrometer has been developed for its simple response function to neutrons and its capability of suppressing background in intense neutron/γ-ray field.

1.4 Outline of the dissertation

This dissertation is devoted to the development of utilizing fast neutrons in applications to fusion and spallation sources, more specifically, is dedicated on large current negative deuterium beam diagnostics and on characterizing the fast neutron beam lines at ISIS.

The first part of the thesis, which is consisting of chapter 1 and chapter 2, presents the motivation, background, introduction on fast neutrons as neutral beam injector diagnostics and for radiation hardness studies at spallation neutron sources, and the introduction on fast neutron measurements, especially the detection methods that we applied in this thesis.

Chapter 3 presents the experiments of neutron emission from deuterium beam-target reactions at the ELISE facility. The developed liquid scintillator-based detection system and the measurements of time trace of neutron emission have been detailed. The local mixing model of describing deuterium implantation for predicting the neutron emission has been presented and been applied to calculate the neutron yield for relative comparing with measurements. Results analysis and its implications for deuterium beam diagnostics on SPIDER are then presented.

Chapter 4 reports the development of a telescope proton recoil (TPR) neutron spectrometer that designed for fast neutron measurement on ChipIr beam line at ISIS. Some different TPR prototypes based on silicon detectors with/without a YAP scintillator have been calibrated and tested on some neutron platforms. The capability of the TPR spectrometers have been investigated followed by their prospects for neutron measurements on the ChipIr beam line.

As a conclusion, the status of the project and its outlook have been summarized in chapter 5. Some of related work has been published in peer-reviewed journals. The papers are summarized and attached in the last part (Synopsis of attached papers) of the dissertation.

Chapter 2

Fast Neutron Measurements

The most incomprehensible thing about the world is that
it is at all comprehensible.
– Albert Einstein

2.1 Interaction of fast neutrons with matter

Neutrons are neutral and don't interact with matter by means of the coulomb force, thus, they cannot be detected directly as an output of electrical signals. The half-life of free neutrons decaying to protons is 877.7 ± 0.7 seconds [81] (the most precise measurement of the neutron lifetime to date), which means that we cannot detect neutrons by measuring their decayed protons in applications. Therefore, we have to understand the interaction of neutrons with matter and convert the neutron signals to electrical signals. The mainly interactions are through two processes [82]: elastic collisions and nuclear reactions. For slow neutrons detection, those neutron-induced reactions that produce charged particles can be utilized, like the most commonly used reactions:

$$^1_0n +^{10} B \longrightarrow^7 Li +^4_2 He + 2.8MeV \tag{2.1}$$

$$^1_0n +^6_3 Li \longrightarrow^3_2 He +^3_1 H + 4.78MeV \tag{2.2}$$

$$^1_0n +^3_2 He \longrightarrow^3 H +^1 H + 0.765MeV \tag{2.3}$$

$$^1_0n +^{235} U \longrightarrow fission+ \approx 200MeV \tag{2.4}$$

All these reactions have high cross sections for low energy neutrons. However, the probability of most neutron-induced reactions potentially useful in detectors drops off rapidly as the neutron energy increases [2]. Meanwhile, the importance of scattering becomes greater because the neutron can transfer an appreciable amount of energy in one collision. The secondary radiations in this case are recoil nuclei, which have picked up a detectable amount of energy from neutron collisions. The most efficient moderator is hydrogen because the neutron can lose up to all its energy in a single collision with a hydrogen nucleus. For heavier nuclei, only a partial energy transfer is possible (e.g. equation 2.5 shows the associated energy transferred to protons after one collision).

If the energy of the fast neutron is sufficiently high, inelastic scattering with nuclei can take place in which the recoil nucleus is elevated to one of its excited states during the collision. The nucleus quickly de-excites, emitting γ-rays, and the neutron loses a greater fraction of its energy than it would in an equivalent elastic collision. Inelastic scattering and the subsequent secondary γ-rays play an important role in the shielding of high-energy neutrons but are an unwanted complication in the response of most fast neutron detectors based on elastic scattering. To separate neutrons from γ-rays, n/γ discrimination is needed, as introduced in subsection 2.2.3.

Based on understanding the interaction of fast neutrons with matter, a lot of corresponding detection methods have been developed: counters based on neutron moderation (Bonner spheres, the long counters, etc.), detectors based on fast neutron-induced reactions (LiI(Eu) scintillator, ^{3}He proportional counters, neutron activation methods, etc.), ToF (time of flight) technique, and detectors utilizing fast neutron scattering (proton recoil scintillators, proton recoil telescopes, etc.). No signal detector or spectrometer works perfectly on fast neutron detection in a complex neutron field to satisfy all required demindings, the choice of a particular detection method is always a compromise among these and other factors. In this thesis, we applied an energy calibrated EJ301 [83] (organic) liquid scintillator as a fast neutron emission monitor for deuterium beam diagnostics as its good capability in n/γ-rays discrimination and radiactive resistance. To surpress the background on the fast neutron beam line ChipIr, a $\Delta E - E$ technique based telescope proton recoil (TPR) spectrometer has been developed with silicon detectors and scintillators together with a plastic neutron convertor to measure the fast neutron spectrum. YAP (inorganic) scintillators [84, 85] have been chosen as the full energy deposition detector (E detector) as its good capabilities of radiation resistance, fast response and high light output.

In the following two sections, the principles of fast neutron detection based on scintillators and TPR spectrometers are introduced.

2.2 Scintillation detectors

The detection of ionizing radiation by the scintillation light produced in certain materials is one of the oldest techniques on record [2]. The scintillation process remains one of the most useful methods available for the detection and spectroscopy of a wide assortment of radiations. The process of neutron detection with a scintillator is that: neutrons interact with the scintillator and excite the atoms and molecules; the atoms quickly de-excite to lower states and re-emit the absorbed energy in form of light; then a coupled electronic light sensor, like a photomultiplier tube (PMT), absorbs the light and re-emits it in form of electrons via the photoelectric effect; at the end the subsequent multiplication of those electrons results in an electrical pulse which can then be analyzed and yield meaningful information about the incident neutrons that originally struck the scintillator. In this process the PMT can be replaced by a silicon photomultiplier (SiPM). Because the array of photodiodes inside the SiPM, which are reverse-biased with sufficient voltage to operate in avalanche mode, could enable each pixel of the array to be sensitive detecting incoming photons by the excitation of charge carriers directly in the silicon.

An ideal scintillation material should possess the following properties:

- It should convert the kinetic energy of incident particles into detectable light with a high scintillation efficiency;
- This conversion should be linear, i.e. the light yield should be proportional to deposited energy over as wide a range as possible;
- The medium should be transparent to the wavelength of its own emission for good light collection;
- The decay time of the induced luminescence should be short so that fast signal pulses can be generated;
- The material should be of good optical quality and subject to manufacture in sizes large enough to be of interest as a practical detector.
- Its index of refraction should be near that of optical glass to permit efficient coupling of the scintillation light to a PMT or other light sensor.

The most widely applied scintillators can be categorized to organics and inorganics based on their ingredients. The inorganics tend to have the best light output and linearity, but are relatively slow in response time. Organic scintillators are generally faster but yield less light. The intended application also has a major influence on choosing suitable scintillators. The high Z-value of the constituents and high density of inorganic crystals favor their choice for γ-ray spectroscopy (because of high density of electrons), whereas organics are often preferred for beta spectroscopy and fast neutron detection (because of the hydrogen content).

2.2.1 Organic and inorganic scintillators

1. Organic scintillators

The fluorescence process in organics arises from transitions in the energy level structure of a single molecule and therefore can be observed from a given molecular species independent of its physical state. A large category of practical organic scintillators is based on organic molecules with certain symmetry properties that give rise to what is known as a π-electron structure [86]. As the spacing between vibrational states of the molecule is large (in order 0.15 eV) compared with average thermal energies (0.025 e V), nearly all molecules at room temperature are in the lowest vibrational state of the ground electronic state. In most organic scintillators, the fluorescence decay time is a few nanoseconds, which thus show a relatively fast prompt scintillation.

Because of the widespread application of organic scintillators in neutron physics and fast time measurements, many types of organic scintillators have been developed, e.g. liquid organic scintillators, plastic scintillators. The EJ301 liquid organic scintillator used in this thesis is a commercial product in which the liquid scintillator is sealed in a glass container then it can be handled in the same manner as solid scintillators. As its lack of a solid structure that could be damaged by exposure to intense neutron radiation, the detector is expected to be more resistant to radiation damage effects than crystalline or plastic scintillators.

2. Inorganic scintillators

The scintillation mechanism in inorganic materials depends on the energy states determined by the crystal lattice of the material. Electrons have available only discrete bands of energy in materials classified as insulators or semiconductors. The lower band, called the valence band, represents those electrons that are essentially bound at lattice sites, whereas the conduction band represents those electrons that have sufficient energy to be free to migrate throughout the crystal. There exists an intermediate band of energies, called the forbidden band, in which electrons can never be found in the pure crystal.

Absorption of energy can result in the elevation of an electron from its normal position in the valence band across the gap into the conduction band, leaving a hole in the normally filled valence band. A charged particle passing through the detection medium will form a large number of electron-hole pairs created by the elevation of electrons from the valence to the conduction band. The positive hole will quickly drift to the location of an activator site and ionize it, because the ionization energy of the impurity will be less than that of a typical lattice site. Meanwhile, the electron is free to migrate through the crystal and will do so until it encounters such an ionized activator. At this point the electron can drop into the activator site, creating a neutral configuration that can have its own set of excited energy states.

After decades of relatively slow evolution, the world of inorganic scintillators has undergone a renaissance that began in the mid-1980s and continues through the present time. Stimulated by the surprising discovery of some new materials that offer excellent light yields and/or fast decay times, a large number of potential scintillation materials have undergone recent testing and evaluation in laboratories around the world. In this thesis, a YAP inorganic scintillator has been chosen as the full energy deposition detector in a TPR neutron spectrometer as its capabilities of good radiation resistance, fast response time and high energy resolution.

2.2.2 Response to neutrons and light collection

Fast neutrons interacting with scintillators usually generate charged particles (recoil protons, heavy ions, or electrons). A charged particle might lose a fraction of the kinetic energy in the scintillator by converting into fluorescent energy. The fraction of the lost particle energy that is converted depends on both the particle type and its energy. In some cases, the scintillation efficiency may be independent of energy, leading to a linear dependence of light yield on initial energy. As the dependence of the light yield of scintillators on the type of particle, a special nomenclature is sometimes used to describe the absolute light yield. The term, MeV electron equivalent (MeV_{ee}) is introduced to place the light yield on an absolute basis. The particle energy required to generate 1 MeV_{ee} of light by definition is 1 MeV for fast electrons but is several MeV for heavy charged particles because of their reduced light yield per unit energy.

In any scintillation detector, one would like to collect the largest possible fraction of the light emitted isotropically from the track of the ionizing particle. Two effects arise in practical cases that lead to less than perfect light collection: optical self-absorption within the scintillator and losses at the scintillator surfaces. With the exception of very large scintillators (many centimeters in dimension) or rarely used scintillation materials (e.g., ZnS), self-absorption is usually not a significant loss mechanism. Therefore, the uniformity of light collection normally depends primarily on the conditions that exist at the interface between the scintillator and the container in which it is mounted.

The light collection conditions affect the energy resolution of a scintillator in two distinct ways. First, the statistical broadening of the response function will worsen as the number of scintillation photons that contribute to the measured pulse is reduced. The best resolution can therefore be achieved only by collecting the maximum possible fraction of all photons emitted in the scintillation event. Second, the uniformity of the light collection will determine the variation in signal pulse amplitude as the position of the radiation interaction is varied throughout the scintillator. Perfect uniformity would ensure that all events depositing the same energy, regardless of where they occur in the scintillator, would give rise to the same mean pulse amplitude. With ordinary scintillators of a few centimeters in dimension, uniformity of light collection is seldom a significant contributor to the overall energy resolution.

2.2.3 Neutron/γ-ray discrimination

Since the shapes of the pulses change with the nature of the incident radiation, then there will be some differences in shapes after amplifing and integrading. Most shape differences arise because of differences in the time profile of the current produced in the detector by a radiation interaction. The fluorescence emission contains a fast component and a slow component. The fraction of light produced in these two groups depends on the exciting particles. In organic scintillators, neutrons produce scattered protons through elastic scattering. Protons have a short range and generate a high concentration of triplet states, which decay by delayed fluorescence. By contrast, γ-ray produce scattered electrons which have a longer range than protons and generate a lower concentration of triplet states (electrons are more likely to produce excited singlet states, which decay by prompt fluorescence). The difference in the pulse shape of the signal as a result of the ratio of prompt to delayed fluorescence produced by different types of radiation makes pulse shape discrimination (PSD) possible. n/γ-ray discrimination based on this principle was suggested and demonstrated in 1960s [87, 88] and now has been applied in digital analysis [89, 90].

Classically, the most often used analog PSD techniques for neutron/γ-ray discrimination are [91]: rise time technique, zero crossing technique and charge comparison technique. In this thesis, the charge comparison technique PSD by comparing the long/short gate charge integration of the signal has been applied on the EJ301 scintillator, as shown in figure 2.1 (Left), where average neutron and γ-ray signals from the measurement of the 2.5 MeV quasi-monoenergetic neutron field have been presented. The short integration Q_s and long integration Q_l are obtained by integrating the pulse in a time interval t_s and t_l from a self-set starting point where the pulse amplitude is about 20% of the peak value in this case. By choosing the time interval $t_s = 15$ ns and $t_l = 40$ ns, neutron and γ-ray events are clearly separated in the two dimensional distribution of Q_s vs. Q_l, as shown in figure 2.1 (Right).

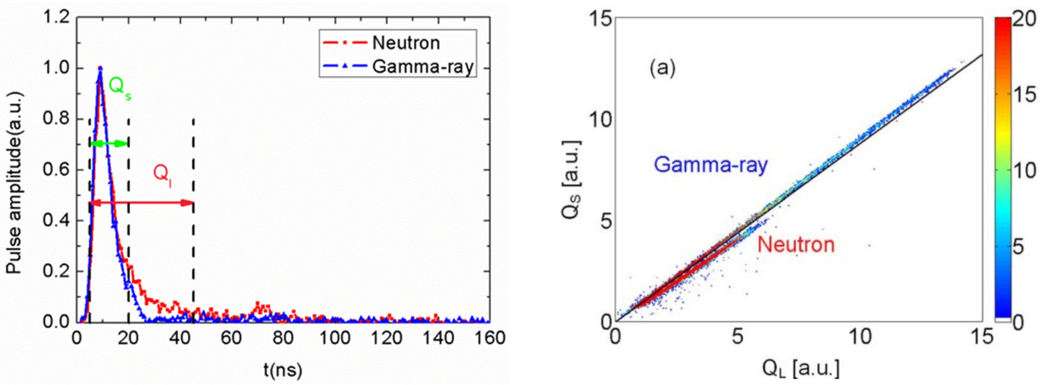

Figure 2.1: Neutron-γ ray discrimination on the used EJ301 scintillator. The right figure is extracted from reference [92].

2.3 Telescope Proton Recoil neutron spectrometers

2.3.1 Principle of neutron detection

Fast neutron detectors are commonly based on measuring the recoil of charged light nuclei. In order to generate charged particles for fast neutrons, the converter containing hydrogen (such as polyethylene (PE) or polypropylene) is usually used by utilizing the elastic scattering on hydrogen. For neutron spectroscopy purposes, it would be preferable if the response function were a simple narrow peak to avoid the problems of spectrum unfolding otherwise required [2]. Telescope proton recoil (TPR) neutron spectrometer is the device which is based on a narrow selection of recoil directions to approach the ideal narrow response peak. A typical TPR spectrometer is consisting of a thin layer of PE to convert neutrons into protons and a high resolution proton detector.

However, in order to reduce backgrounds from competing reactions and other unwanted events, multiple detectors are often used for coincidence analysis. A schematic diagram of a $\Delta E - E$ TPR neutron spectrometer is shown in figure 2.2. By operating the two detectors in coincidence, only particles incident from the direction of the radiator can be selected. The energy sum of the two coincident signals will be proportional to the incident neutrons.

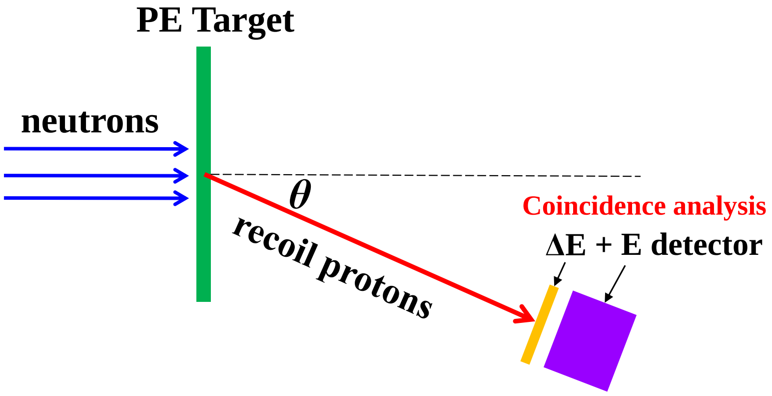

Figure 2.2: Schematic of a typical $\Delta E - E$ TPR neutron spectrometer.

As the convertor used for TPR is usually polyethylene instead of pure hydrogen, then the recoil protons are mostly produced by the elastic scattering of neutrons on light nuclei (etc., C and H). If the neutron energy (E_n) is not very high, then the relativistic effect is ignorable and the energy of recoil protons (E_p) observed at an angle of θ with respect to the incident neutron direction can be given simply by equation 2.5.

$$E_p = \left(\frac{\cos\theta + \sqrt{A^2 - \sin^2\theta}}{1 + A} \right)^2 E_n \tag{2.5}$$

where A is the atomic mass number of atoms on PE target (A = 1 for Hydrogen and 12 for Carbon).

Detectors are usually positioned at a small angle with respect to the neutron direction to get enough high intensity of recoil protons. Some designs [93] even put the proton detector at the incident neutron direction ($\theta = 0$), but others choose a finite observation angle to avoid neutron-induced background events in the detector from the primary beam. A TPR neutron spectrometer can vary a lot according to demanding, like the neutron energy range, energy resolution, detection efficiency and the background suppression etc. [94]. More detailed configurations on TPR design have been introduced in section 4.1.

2.3.2 Particles discrimination

1. $\Delta E - E$ technique

The $\Delta E - E$ technique is applicable for particles discrimination when particles with kinetic energy E pass through the first detector and are stopped in the second one. The energy deposition of charged particles on the two detectors is different for different particles, due to their different stopping powers in detectors. The Bethe formula [95] describes the mean energy loss per distance of charged particles (protons, alpha particles, atomic ions) when they passing through a layer of matter. Equation 2.6 shows the non-relativistic version

$$-\frac{dE}{dx} = \frac{4\pi e^4 z^2 NZ}{m_e v^2} ln \frac{2m_e v^2}{I} \tag{2.6}$$

where v and z are the velocity and charge of the incident charged particle; N and Z are the number density and atomic number of the absorber atoms; m_e is the electron rest mass and e is the electronic charge. The parameter I represents the average excitation and ionization potential of the absorber and is normally treated as an experimentally determined parameter for each element.

Equation 2.6 is generally valid for different types of charged particles provided their velocity remains large compared with the velocities of the orbital electrons in the absorbing atoms. For a $\Delta E - E$ TPR spectrometer, the energies deposited by charged particles on the two detectors allow to produce identification (ID) maps mathematically described by the Equation 2.6, where the bending radius of each ID depends on the charge and mass of the ion species only. This makes particle identification possible [96].

2. Pulse shape discrimination

Theoretically, the low energy threshold measured by a $\Delta E - E$ telescope is the kinetic energy of the incident charged particle which just enable it passing through the first detector (ΔE). Practically, as the rest energy of charged particles after passing through the first detector should be significantely larger than the electronic noise of the second detector, the detected low energy threshold is relatively high [97]. For instance, a $200\mu m$ thick silicon detector could completely stop about 4.8 MeV protons or 19 MeV α particles [98], then the detectable low energy threshold might be relative high by using it as a ΔE detector in applications. If we just simply decease the thickness of the first detector, then the dynamic range for particle identification will be small. This is because high energetic charged particles lose a few energy on a thin layer then it will be difficult for detection. In order to reduce the low energy threshold for particle identification in telescopes or arrays, the pulse-shape discrimination (PSD) method has been applied for semi-conductor detectors, especially for silicon detectors [99–106].

Indeed, because of the different stopping powers, different particles with the same kinetic energy produce different energy loss “profiles” along the detector depth and this results in different charge collection times, i.e. in different pulse shapes [107]. The time dependence of the current signal in semiconductors is ruled essentially by two phenomena: the charge carrier dissociation (the plasma erosion time) and the duration of the drift of the electrons and holes towards the appropriate electrodes, which depends on electric field strength and carrier mobilities [108]. Figure 2.3 shows the electronic filed of a double sided silicon detector and the movement of the holes and electrons. When two different types of particles incident with the same energy on a silicon detector, from the rear (particles entering through the lower electric fields side) or front (particles entering through the high electric fields side) side, the pulse shape discrimination at variance is very sensitive to the detector mounting [108]. In case of rear side injection, the identification with the “energy vs. charge rise time” PSA method presents energy thresholds which are significantly lower than in the case of front side injection.

Nowadays, the digital pulse-shape analysis (DPSA) for charged particles which are fully stopped in silicon detector has been developed which is benefited from the digital signal processing made possible by a new digital sampling electronics [108, 109]. However, one limitation of the PSD technique is still the finite energy threshold for particle identification [102]. This threshold is caused by an unexpected decrease of the total charge-collection time for ions with a short range, in spite of the fact that the particle tracks are located in a region of very low electric field.

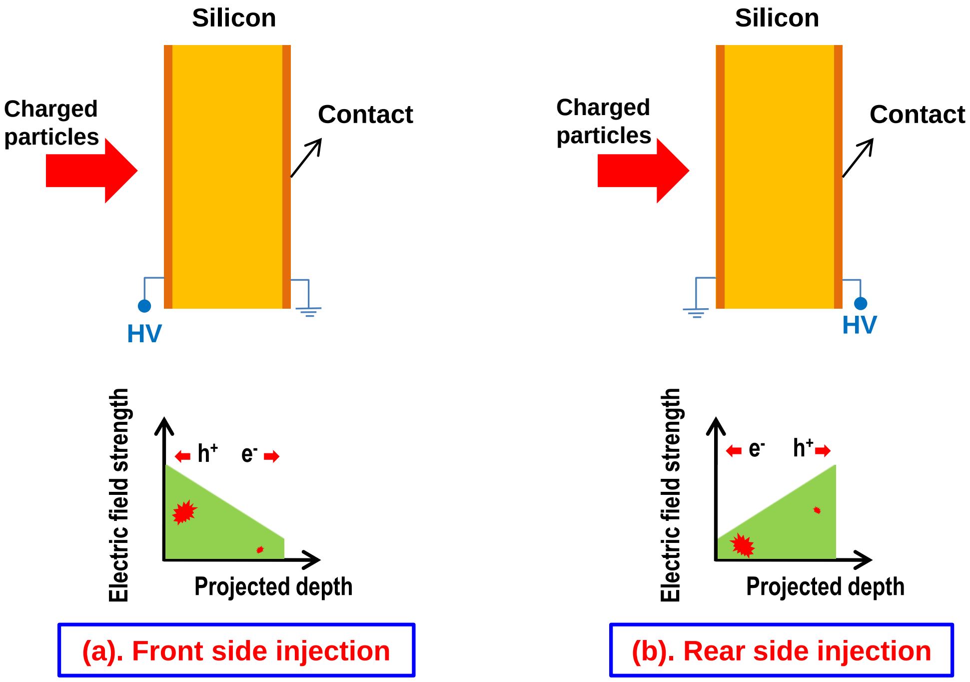

Figure 2.3: Schematic diagram of a double sided silicon detector with its electric filed distribution for charged particles detection. Left: charged particles entering from the front (high electric field) side; Right: charged particles entering from the rear (low electric field). For two types of same charged particles incident with same kinetic energy, the penetration depth of the heavier one is lower than the lighter one, and that results the different raise time on pulse shape.

Chapter 3

Neutron Emission from Beam-target Reactions

> *I have discovered a truly marvelous proof of this,*
> *which this margin is too narrow to contain.*
> – Pierre de Fermat

Measurement of neutron emission has been proposed as a means of deuterium beam diagnostics in SPIDER and MITICA neutral beam test facilities as introduced in section 1.2.3. Neutrons here are produced by the $D(d,n)^3He$ reaction between the incident deuterium beam and deuterons implanted in the copper beam dump, and are detected by the neutron imaging system CNESM. In SPIDER, an expected neutron yield for 100 keV deuterons on saturated copper alloy has been indicated as about 10^{12} neutrons/s spread over 1 m^2 beam dump [110]. In order to present the intensity map of deuterium beam on the dump by measuring produced neutrons, the physics behind the deuterium implantation in the dump by impinging large current negative deuterium ions should be investigate first, for confirming the indicated neutron yield and aiding the CNESM system development. The Local Mixing Model (LMM) [111–113], which has been quite successful in predicting the properties of hydrogen retention and isotope exchang for a variety of refractory material [114], has been applied for describing the evolution of implanted deuterium ions in the copper beam dump and to calculate the time trace of neutron emission. A liquid scintillator-based detector has been developed to detect the time trace of neutron emission at the ELISE facility. Relative comparison between calculations and measurements has been analyzed. Implications based on so far results have been made for neutron based diagnostics at SPIDER.

3.1 The Local Mixing Model

In LMM diffusion or migration of deuterons is neglected once the negative deuterium ions are implanted. In order to obtain more information about the beam parameters (position, profile, divergence, intensity, homogeneity, etc.), a high spatial resolution diagnostic calorimeter, which is consisting of many small blocks to provide a 2D image of the beam profile, is usually used as the beam dump [115]. In deuterium operation, the time dependent total neutron yield on a rectangular dump from the beam-target reaction, $Y(t)$, can be obtained by summing the neutron production in each block with the equation 3.1.

$$Y(t) = \sum_{i=1}^{N_i} \sum_{j=1}^{N_j} \int_0^R \Phi_{i,j}(z,t) n_{i,j}(z,t) \sigma(z,t) A_{i,j} dz \tag{3.1}$$

Where N_i and N_j are the number of blocks on the ith row and jth column of the dump, respectively; R is the projected range of the incident deuterium. $\Phi_{i,j}(z,t)$ is the deuterium flux in the block at a depth z and at a time t; $n_{i,j}(z,t)$ is the time dependent number of deuterons that get deposited per unit volume at a depth z; $\sigma(z,t)$ is the $D(d,n)^3He$ neutron production cross section which depends only on the incident deuterium energy; $A_{i,j}$ is the area of the block. The schematic diagram of the LMM is shown in figure 3.1. Calculations of the beam flux $\Phi_{i,j}(z,t)$, deuterium concentration density $n_{i,j}(z,t)$, and the cross section $\sigma(z,t)$ for each block are introduced in the following three subsections: 3.1.1 - 3.1.3.

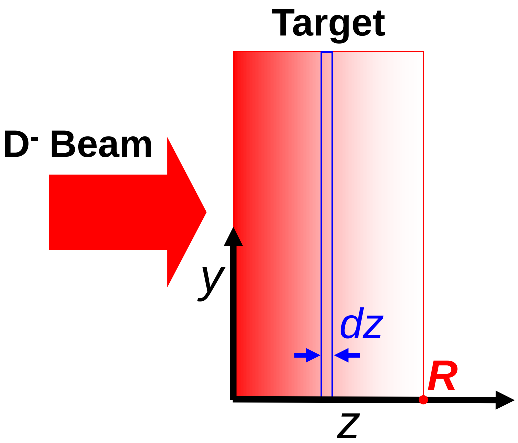

Figure 3.1: Schematic diagram of the Local Mixing Model.

3.1.1 Deuterium beam flux in depth

For the incident deuterium beam on the ith row and jth column block of the dump, the deuterium flux in the block at a depth z and at a time t, $\Phi_{i,j}(z,t)$, can be calculated with equation 3.2.

$$\Phi_{i,j}(z,t) = \Phi_{i,j}(0,t)(1 - \int_0^z p(x)dx) \tag{3.2}$$

where $p(x)$ is the probability for the deposition of a deuteron at a depth x and depends on the incident energy and the dump material significantly. In the LMM, no other reactions but deposition has been assumed and the probability of deposition in depth has been normalised to 1. The TRansport of Ion in Matter (TRIM) code [116] is applied to calculate the $p(x)$ for incident deuterons with a step of 0.5 keV in this thesis. As an example, figure 3.2 shows the normalized deposition profiles of different energetic deuterons incident on a pure copper layer (density: 8.902 g/cm^3).

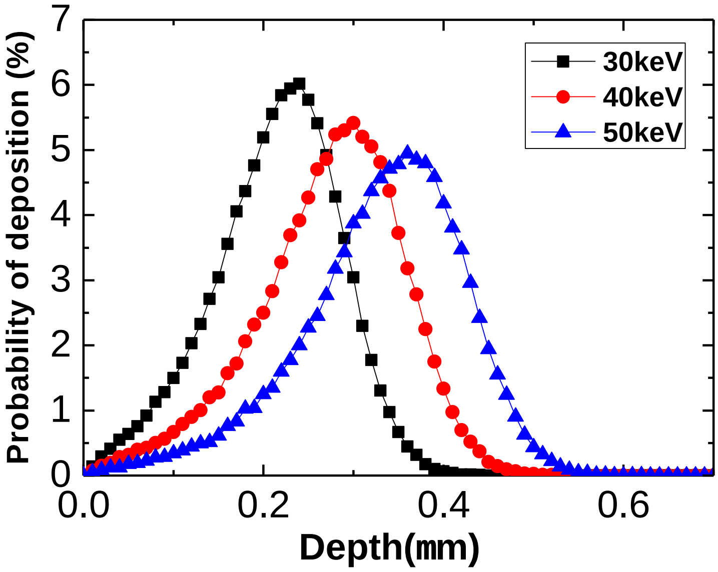

Figure 3.2: Different energetic deuterons concentration profiles in copper which are calculated by the TRIM code and normalized to 1.

The item, $\Phi_{i,j}(0,t)$, shown in equation 3.2, is the incident deuterium flux and can be in turn given by

$$\Phi_{i,j}(0,t) = \frac{I_{i,j}}{A_{i,j} \cdot q} \tag{3.3}$$

where $I_{i,j}$ is the current that reaches the ith row and jth column block and q the ion charge. $I_{i,j}$ is obtained by dividing the measured beam power on each block by the the total voltage (extraction voltage + acceleration voltage) that applied on the beam.

3.1.2 Density of trapped deuterons in depth

Ion implantation of hydrogen isotopes into metals can yield high concentrations of atoms [117]. The concentration rate here is defined as the percentage of deuterons to target atoms per unit volume. As the incident deuterons penetrate in the dump, the local deuteron concentration increases until a maximum is reached (saturation) and the saturation level depends only on the target material and its temperature. An important issue in evaluating the neutron source coming from the beam-target $D(d,n)^3He$ reactions is to predict the density profiles of the deuterium content within the implantation zone of the copper-target material [118]. A "deuterium saturation density" in copper of 1.7×10^{28} D/m^3 at room temperature, which is about 20% of the Cu atom density of the material and corresponds to the stationary profile reached in irradiation conditions, has been used as a reasonably conservative value [119,120]. Additional hydrogen coming to rest in a saturated region results in the local loss of an equivalent quantity of hydrogen with the isotopic composition of the lost hydrogen being the same as that in the region itself. Hydrogen lost from a saturated region is assumed to escape through the target surface [114]. With the calculation based on the TRIM code we found that less than 3% incident deuterons are scattered from the copper target. For simplification no deuterons escape is assumed in this modeling. As the deposition profile of deuterons in the target has been normalized to 1, then the trapped deuterium density of each block in depth z, $n_{i,j}(z,t)$, can be derived by

$$n_{i,j}(z,t) = n_{target} \cdot min\left(C_{max}, \int_0^t p(z)d\tau\right) \tag{3.4}$$

where n_{target} is the number of target atoms per unit volume (in cm^3); C_{max} is the saturation concentration rate of deuterium which is determined by the target material and its temperature, as introduced above, $C_{max} = 20\%$ in copper in room temperature.

3.1.3 DD cross section in depth

Neutrons are produced by the D(d,n)^{3}He reactions and the cross section of the reaction is dependent only on the incident deuterium energy. However, the deuterium ions loss their energy after they are impinged in the target. In order to calculate the time dependent cross section as a function of depth ($\sigma(z,t)$ in equation 3.1), energies of deuterons at depth z have been calculated by using the total stopping power data from the TRIM code so to convert the energy dependent D(d,n)^{3}He cross section to a function that depends on the depth z.

The total stopping power of copper to deuterium ions was extracted from the database of TRIM code and is shown in figure 3.3 (Left). The applied D(d,n)^{3}He cross section was extracted from the evaluated library ENDF/V-II.0 [121] and the cross section as a function of energy is shown in figure 3.3 (Right).

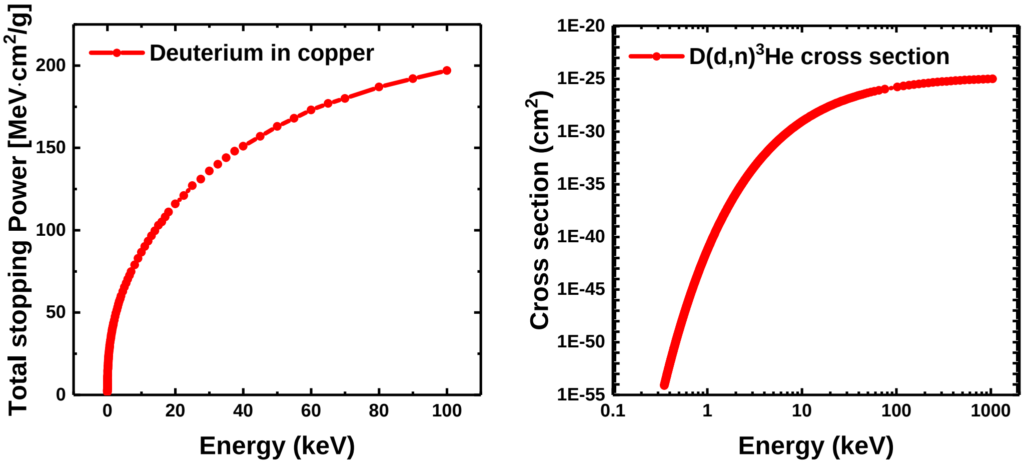

Figure 3.3: Left: The total stopping power of copper to deuterium ions; Right: The evaluated D(d,n)^{3}He cross section.

For each incident deuterium beam, the energy can be determined by measuring the high voltage that applied on the ions. With the incident energy and the data that provided in figure 3.3, the cross section as a function of depth can then be obtained. Figure 3.4 shows an example of the deuteron energy and the D(d,n)^{3}He cross section as a function of depth for 40 keV incident deuterons. From the figure we note that the effective layer from which neutrons are produced is only 0.5 μm thick and that most neutrons are produced within the first 0.2 μm.

3.2 Time trace of neutron emission measurements at the ELISE facility

In order to verify the LMM for the prediction of the neutron emission in SPIDER and aid the CNESM detection system development, measurements of the neutron emission from D(d,n)^{3}He reactions have been performed. A parasitic experiment [92] was first done in the low RF power deuterium campaign at the ELISE facility [122, 123] in 2014.

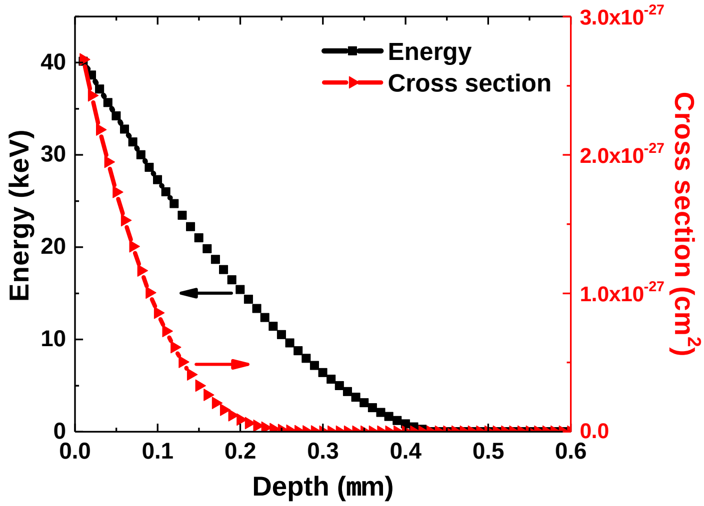

Figure 3.4: Deuteron energy (left scale) and the D(d,n)^{3}He cross section (right scale) as a function of depth in copper for initial incident energy at 40 keV.

In that first study [92], the time evolution of neutron emission for the whole deuterium campaign at ELISE has been obtained to benchmark calculations based on the LMM. However, only one 2D infra-red image has been applied and used as the deposited beam power distribution for the whole pulses. The beam current, which is used to calculate the incident beam intensity in LMM, was the measured extracted ion current. The beam loss during acceleration was not considered. By matching the neutron emission in the initial rising part of the measured counting rate (i.e. the concentration of deuterium was reaching saturation) to calculation, measurement and calculation have been compared in a relative scale. The experimental results were generally found to be consistent with calculations but, at a detailed level, an over estimation of about 40% of the emission was often observed, and went up with higher beam power.

In order to test the capability of the LMM to predict the magnitude of neutron emission in a more precisely way, a new dedicated experiment was performed on 3 consecutive days (6th - 8th, Oct. 2015). The new study makes use of fully developed IR and calorimetry diagnostics to provide more accurate input data for the calculations. First, the 2D IR images for all the pulses extracted in the experimental period were obtained. And the second, benefiting from later refinements of the method to analyze data from the diagnostic calorimeter, the total beam current loaded on the dump (I_{cal}) has been derived by dividing the known deposited power by the total applied high voltage [124]. With the total loaded beam power and the 2D IR images, the loaded current on each block has then been derived and used as the input for the LMM-based calculation.

3.2.1 Experimental setup

The test facility ELISE (Extraction from a Large Ion Source Experiment), situated in the Max Planck Institut für Plasmaphysik in Garching, Germany, is the first large RF (radio frequency) driven ion source for the production and extraction of negative ions [125]. The ELISE ion source, with a size of $0.9 \times 1\text{m}^2$ and an extraction area of 0.1 m^2, has the same width but half the height of the ITER source. That indicates that the ELISE test facility is the perfect experimental platform on which we could investigate the physics behind the neutron emission from the large current negative deuteium beam-target reactions for the neutron diagnostics on SPIDER. Negative hydrogen (H) or deuterium beams here can be extracted and accelerated up to 60 kV for 10 seconds (s) every 3 minutes out of the continuously operating plasma source [126, 127].

An EJ301A liquid scintillator produced by Scionix was installed in vicinity of one of the two inner walls of the ELISE facility to monitor the neutron emission. The scintillator was placed behind the beam dump and in the same horizontal level as the center of the dump, as shown in figure 3.5. The distance between the dump and detector is approximately 2.8 m.

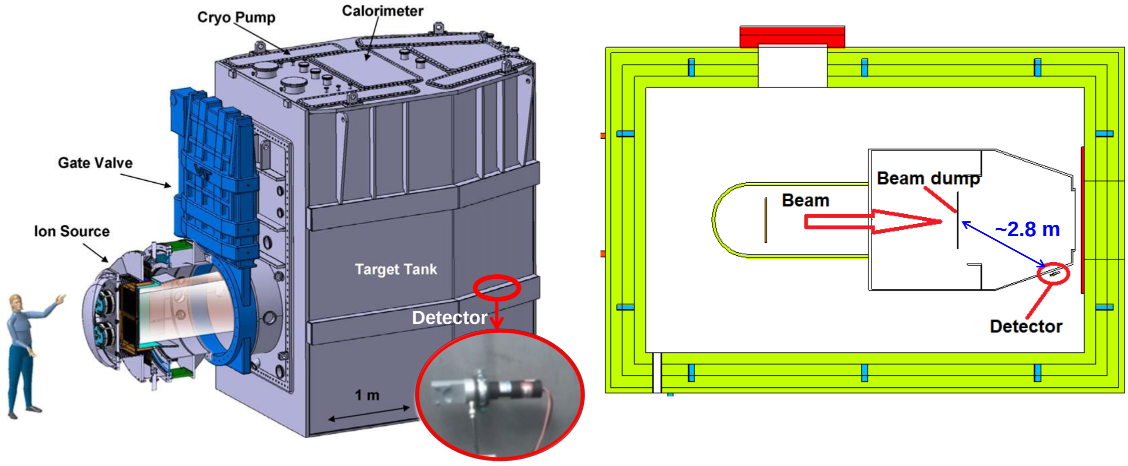

Figure 3.5: Left: The ELISE test facility with indicating the neutron detector position, extracted from ref. [123]; Right: The top view of schematic diagram of the ELISE facility showing the deuterium beam, beam dump, and the position of the installed liquid scintillation detector.

3.2.2 Time trace of neutron emission measurement

The EJ301A scintillator has a detection efficiency of 16% to 2.5 MeV neutrons and was coupled to an active base H10580 Hamamatsu PMT to minimize gain shifts [128]. The signals coming from the detector were digitized by means of a 14 bit, 400 MS/s custom digitizer based on the ATCA (Advanced Telecommunications Computing Architecture) platform [129]. A standard charge comparison technique PSD by comparing the long/short gate charge integration of the signals, as we introduced in section 2.2.3, has been applied for n/γ-rays discrimination.

In order to monitor the stability of the PMT, a LED source has been coupled to the PMT as well. The intensity of the LED source was set as 1000 Hz. With the charge comparison technique PSD, neutrons, γ-rays, and the LED signals could be separated clearly, as shown in figure 3.6. In order to reduce the extent of low energy neutrons in the measured signal, a threshold of 0.26 MeV (E_{ee}), which corresponding to a neutron energy of 1.15 MeV, was used in the measurements. In this way, the probability of a wrong n/γ-ray events discrimination was reduced to about 6%.

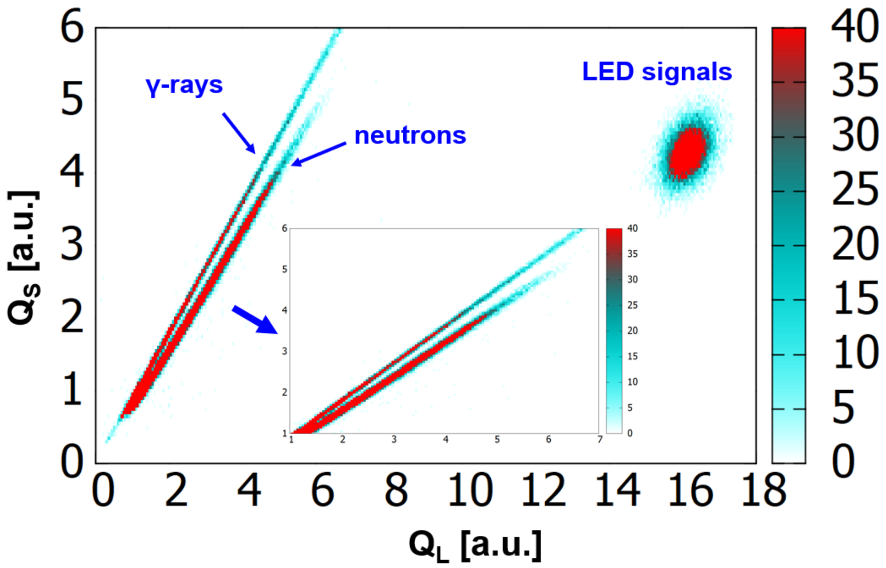

Figure 3.6: Particles discrimination using the charge comparison PSD that applied on the scintillator. Neutrons, γ-rays, and LED light signals are separated clearly.

The time evolution of neutrons and γ-rays counting rate during a pulse then has been individually reconstructed. Figure 3.7 shows the measured neutrons, γ-rays, and LED signals for an extracted pulse in ELISE as a function of time. The PMT was found stable and the time evolution of measured neutrons and γ-rays, as expected, was similar. The simultaneous radiation emission started at the beginning of each pulse and the ration of neutrons to γ-rays was about 2-3. For each extracted deuterium pulse on ELISE, the measured neutrons always show a constant intensity as a function of time in pulse duration, as shown in figure 3.7. In order to compare the measurement with calculation, which is mainly based on the LMM by employing the beam current and high voltage (HV) that have been measured for each pulse, the average intensity of neutron emission for each pulse has been calculated.

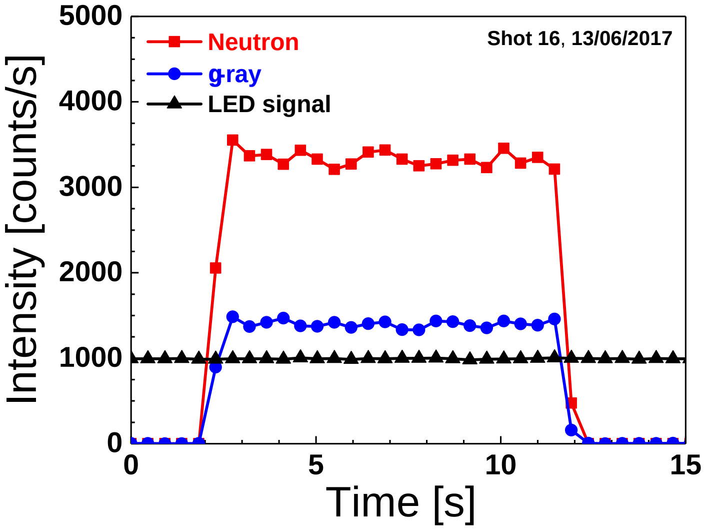

Figure 3.7: The time trace of neutrons, γ-rays, and LED signals emission measured for the same extracted pulse in ELISE.

3.2.3 Operation of pulsed deuterium beams

Ions were extracted from the source and accelerated to the dump pulse by pulse. The extraction (U_{ex}) and acceleration voltage (U_{acc}) for the ELISE source were supplied by two "stacked" HV-Modules, capable of up to 35 kV, 50 A and 70 kV, 25 A, respectively [130]. The total energy of ions arrived at the beam dump, i.e. the total high voltage applied on the ions, were obtained by summing the measured extraction and acceleration voltage ($U_{ex} + U_{acc}$).

The beam dump consists of 4 HCP (hexagonal close packing) copper plates with a size of 600 mm × 600 mm, 2 cm thick, covering a total area of 1.2 m × 1.2 m, and is designed to stop an ion beam of 20 A with up to 2° divergence [115]. Each calorimeter plate is made of a copper back plate, with embedded cooling water circuit, and 15 × 15 copper blocks (beam facing area: 38 mm × 38 mm, thickness: 25 mm, gap between blocks: 2 mm) which are individually brazed on the beam-facing side of the back plate with an intermediate thermal resistance [131]. The side facing the beam is coated with Molybdenum Disulde (MoS_2) to perform IR analysis. This is done by a micro-bolometer IR camera (FLIR A655sc), which is triggered 5 seconds before the HV phase and acquires IR images for one minute, including the 10 s beam time, with the aim to measure the average temperatures of each block [132]. The camera is equipped with a wide angle objective that provides full view of the calorimeter. Through an evaluation procedure it is possible to obtain a 2D image of the beam power distribution with a total resolution of 30 × 30 "pixels". With the 2D image of the beam power distribution and the ion current, the deuterium flux on each block can be determined by using the equation 3.2, and then the total neutron emission on the dump can be calculated using the LMM.

182 pulses, with increasing beam current (I_{ion}) in the range about 6 A - 17 A and at a fixed total voltage $V = 30$ kV, have been extracted, as shown in figure 3.8. The lower beam power corresponds to the region where $< 10\%$ discrepancies between calculations and data were found in our first experiment [92]. The time shown here (x axis) is the accumulated beam time, i.e. the effective time of beam pulses, net of pauses. The accelerated current reaching the dump, I_{cal}, can be however different from the total extracted ion current I_{ion}, up to about 20% - 30%, as some ions were stopped by the grounded grid and the ground shield in their path from the RF source to the dump [124]. The drop of I_{cal} at $t = 1074$ s was due to a fault of the calorimeter diagnostic in one pulse.

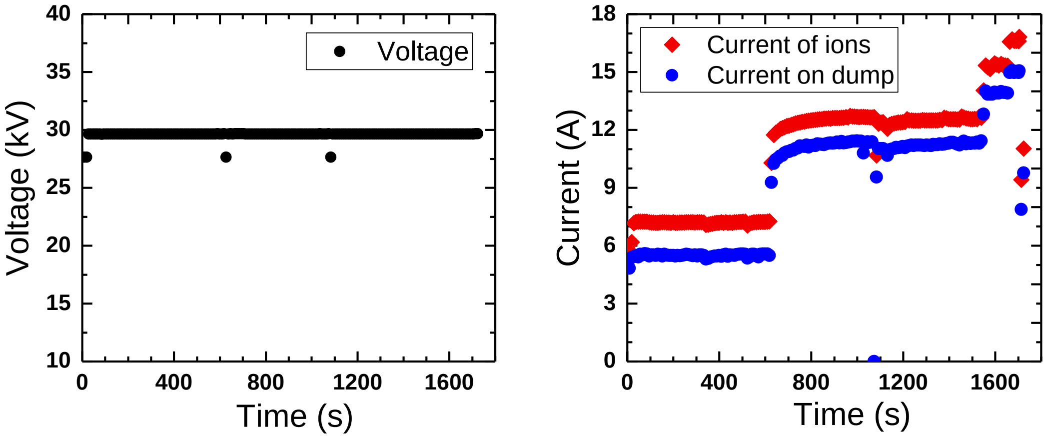

Figure 3.8: Operation parameters of the dedicated neutron experiment on ELISE in 2015. Left: the total high voltages that applied on ions; Right: current of the ion beam and the current loaded on the dump.

Before the dedicated experiment, a set of experiments with different parametric deuterium beams (e.g. different voltages, currents, and beam profiles) were performed from the beginning of the deuterium campaign (15 Sep., 2015) so that we could assume that deuterium concentration has reached at saturation. Deuterium beams were designed to focus on the beam dump as could as possible and to achieve very similar beam profiles when the machine was operated at increasing values of the current. Figure 3.9 shows the example of beam images obtained by the IR camera in the three experimental days. Beam profiles were similar and most of them were focused in central part where the deuterium concentration has been assumed as saturation.

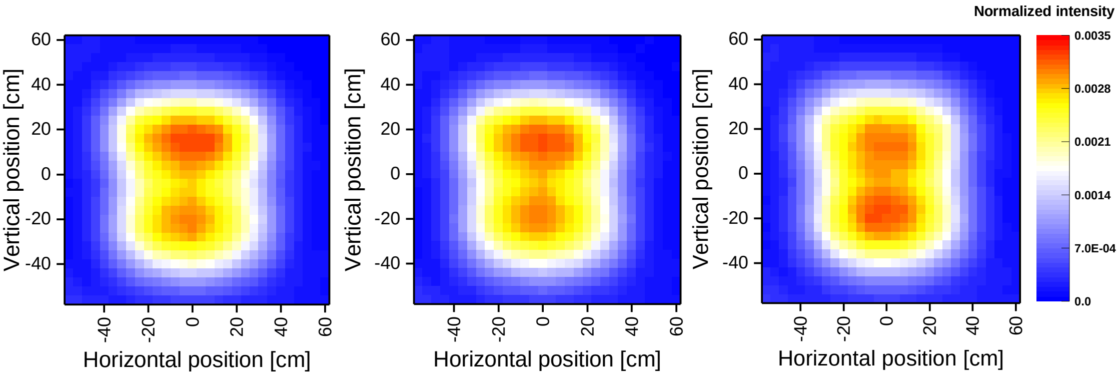

Figure 3.9: Typical beam profiles measured during the neutron emission experiment on the 3 consecutive days with the ELISE IR camera and normalized to the total deposited beam power.

3.2.4 Results and Comparison with calculations

In order to interpret data, for each of the pulse we performed, the expected time dependent neutron yield ($Y(t)$) was calculated based on the LMM of deuterium deposition in the dump made by 99% of copper. The deposition profiles of deuterium in the dump have been calculated with the TRIM code with incident energy from 27 keV to 31 keV with a step of 0.5 keV. The deposited power distribution on each block has been normalized to the total deposited beam power on the dump, which was used to calculate the incident deuterium flux on each block. The concentration at saturation was set as 20% based on ref. [119] and our previous experiment [92]. In order to compare simulations and measurements in a more quantitative way, the conversion coefficient k from calculated neutron yield $Y(t)$ (neutron/s from the target) to the detector counting rate (r_n) has been determined. As k depends only on the neutron transport from the dump to the detector and the detection efficiency of the scintillator, it can be empirically evaluated by the ratio between the simulation and measurements at one experimental point where the LMM based calculation is assumed to be correct that can be used to describe the physics behind the LMM perfectly. As the beam currents that extracted in the first 600 s as shown in figure 3.8 were stable, data in the period (200 s - 408 s) have been used to calculate different k values, for calculations based on the I_{ion} and I_{cal}, respectively.

Figure 3.10 (left) shows the neutron counting rate during our experiment, together with the converted LMM-based calculations by using the ion current (I_{ion}) and the loaded current on the calorimeter (I_{cal}), respectively. As neutron emission responds to changes of the current reaching the calorimeter, as well as to the build up of deuterium concentration in the dump, for each value of I_{ion} we performed several pulses until a sufficiently stationary neutron rate was observed so to enable a clean comparison between data and simulations. The discrepancies between calculations and measurements, presented by C/E (ration of calculations to experiments), are shown in figure 3.10 (right). From the results of figure 3.10 we observed that, at t > 600 s, calculations based on I_{cal} agree better with experimental results, as expected, showing that well calibrated neutron measurements are sensitive even to current variations smaller than 20%, such as the difference between I_{ion} and I_{cal}.

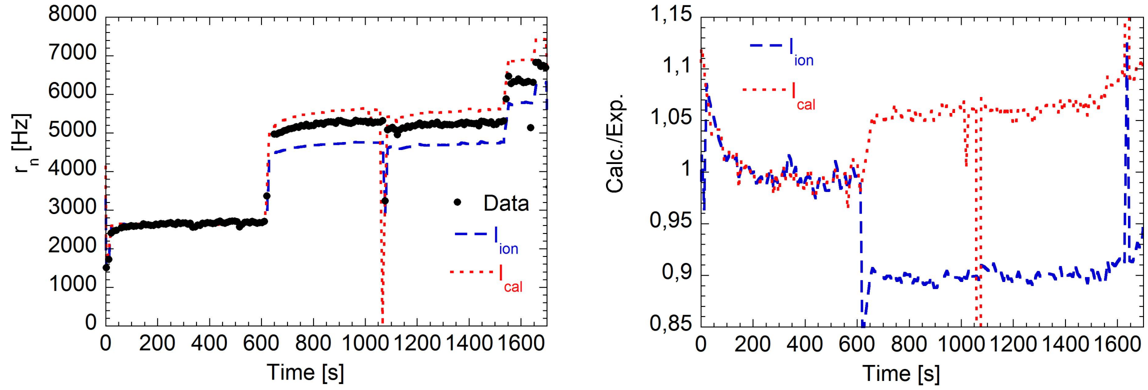

Figure 3.10: Comparison of measurements and calculations based on the LMM by employing beam current I_{ion} and I_{cal}, respectively. The error bars on the data are of the same size as the dots.

Concerning the beginning phase (t < 100 s) at $I_{ion} \approx 7$ A, the LMM model was found less accurate. This is due to some missing beam profile measurements during the technical discharges performed in the days preceding our experiment. Some uncertainties then have been introduced in our determination of the detailed build up of deuterium concentration before the full saturation was reached (stationary neutron emission) at $t > 200$ s.

A closer inspection to figure 3.10, however, reveals that, albeit at the level of < 10 %, there still seems to be a systematic discrepancy between measurements and I_{cal} based simulations that I_{cal} based calculations tend to overestimate neutron emission. On the contrary, I_{cal} based calculations always underestimate emission, but the agreement with measurements is improved as current gets larger. Compared to our former experiment, where we observed a disagreement at the level of ≈ 30 % already at $I_{ion} = 8$ A - 10 A, we can conclude that an accurate knowledge of the beam profile and current is essential for a reliable determination of the neutron emission and improves the agreement to a better than 10 % level. The discrepancies observed earlier were most likely due to insufficient input diagnostic information.

At the same time, however, we found no way to reconcile the remaining difference and we conclude that some additional deuterium diffusion caused by temperature effects away from the saturation state must be included in the model to completely account for the observations. This process, which is outside the LMM used here, does not play a very important role at the currents and voltages we have tested so far, as we were able to predict neutron emission with an accuracy better than 10%. However, our data provide reasonable evidence that diffusion outside the LMM is at play in beam-target neutron emission experiments and becomes progressively more important as beam power is increased, as shown in figure 3.11.

Figure 3.11 shows a linear correlation between the C/E and deposited beam power, but for a few outliers. These correspond to the first few pulses of each experimental day or after a long duration between pulses when, presumably, a full saturation of the deuterium concentration in the dump was not yet reached as the deuterium diffusion effect. A linear fit to the data of figure 3.11 yields $C/E = (3.55 \pm 0.08) \times 10^{-4} Power(kW) + (0.945 \pm 0.002)$. For comparison, SPIDER is meant to operate with I = 40 A, V = 100 kV, up to 1 h beam pulses. The power $V \cdot I_{cal}$ delivered on the dump by the beam at SPIDER will therefore be about 4000 kW and about 10 times larger compared to our experiment. Considering the area of the beam dump in SPIDER is 2 times larger than that in ELISE, the LMM based neutron emission calculations for SPIDER may be over estimated by up to a factor 1.645 under the assumption that deuterium diffusion outside

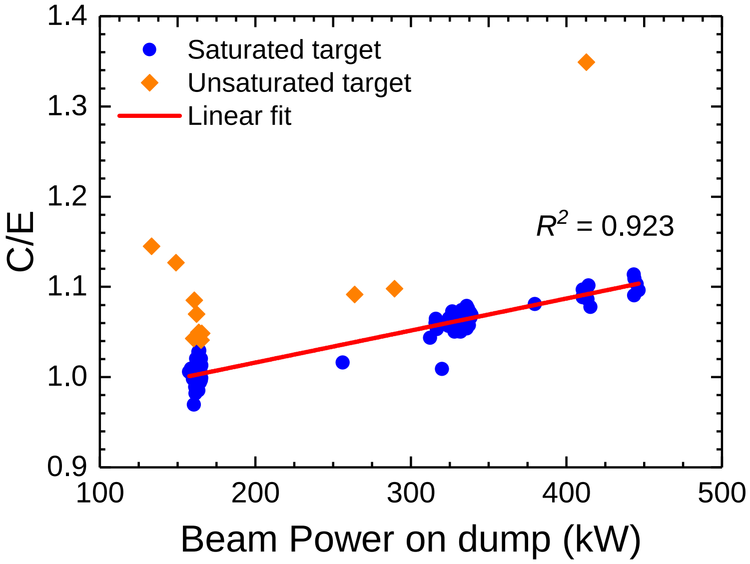

Figure 3.11: The ratio of the calculations and measurements C/E as a function of the beam power loaded on the dump.

the LMM scales linearly as the beam power density. This suggests that a quantification of the diffusion coefficient that needs to be added to the neutron emission model is demanded for reliable predictions at SPIDER.

3.3 Probing the LMM on ELISE and implications for SPIDER

3.3.1 High power beam-target neutron emission on ELISE

In order to verify whether the linear, empirical correction which we derived from the beam-target neutron emission experiment in the power range 160 kW to 440 kW still extrapolates linearly towards the beam power expected at SPIDER, we then performed another dedicated experiment that explores the beam power approaching the maximum capabilities allowed by the ELISE facility in 2017. The beam power was scanned from about 200 kW to 950 kW by modifying the beam current and/or applied voltage in a controlled manner. The filling pressure was set to 0.6 Pa. 231 deuterium pulses have been extracted in 3 different experimental days. The operation parameters including the beam currents deposited on the dump, high voltages (HV) are shown in figure 3.12.

Still, particular attention was paid to ensuring a constant beam size and profile as

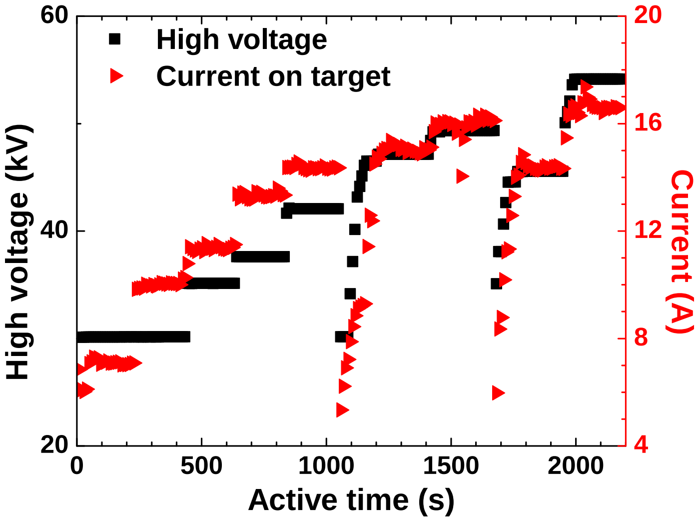

Figure 3.12: High voltage (kV; left scale) and current (A; right scale) parameters of the deuterium beam extracted in the neutron emission experiment in 2017.

the power was scanned. A 2D beam power deposition profile (obtained by the 30 × 30 blocks) at low (300 kW) and high (900 kW) power deposition (W/m^2) is shown in figure 3.13. The deuterium beam power deposition profiles are very similar in the two cases as we have designed the beam parameters on purpose to achieve concentrated and comparable profiles at different powers.

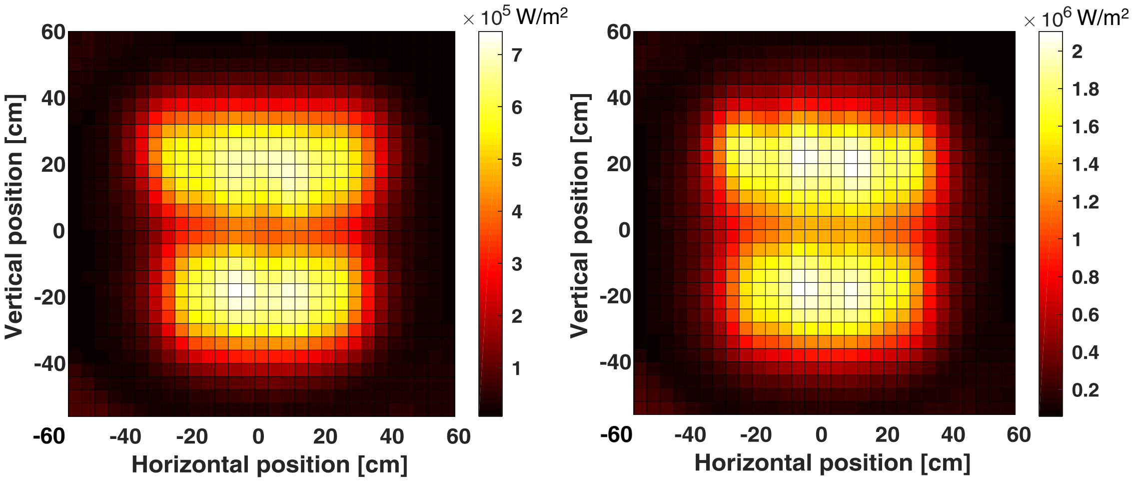

Figure 3.13: Deuterium beam power deposition profiles measured in the neutron emission experiment by the ELISE infra-red camera at low (300 kW, left) and high (900 kW, right) power deposition on the dump.

Neutron emission is still measured by the calibrated Scionix-EJ301A liquid scintillator which was used also in our previous experiment at the same position. The average neutron intensity measured during each pulse was used to compare with LMM based calculations. As a set of experiments with a 22-44 keV deuterium beam was performed before the dedicated neutron emission experiment from the beginning of the deuterium campaign (25 Apr., 2017), the deuterium concentration has been assumed to saturation. Figure 3.14 shows the LMM based calculation of the time trace of neutron emission together with the measurement in our dedicated experiment. The calculation is based on equation 3.1 and uses as input the measured diagnostic information on the beam (current, voltage, profile). In general the LMM based calculation reproduces the basic features of the emission, i.e. the step ladder increase of the neutron yield as the beam power on the target increases. In order to compare calculations and measurements in a more quantitative way, the conversion coefficient k from calculated neutron yield $Y(t)$ to the detector counting rate r_n has been determined by normalizing data at 200 kW on the dump between t=114 s and t=209 s, where the LMM based calculation is assumed to be correct.

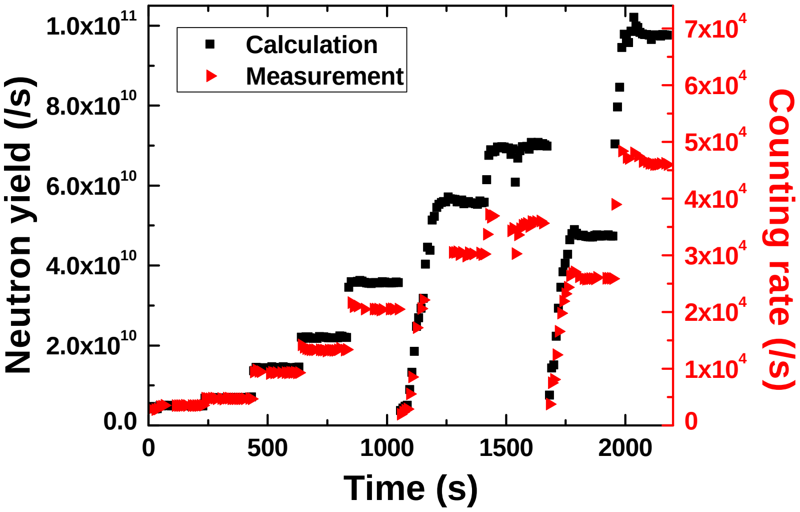

Figure 3.14: Calculated neutron emission from the dump as a function of time (left axis) compared to the measured counting rate (right axis).

Figure 3.15 shows the comparison of measurements and calculations on a quantitative ground, albeit on a relative scale. If the LMM model held exactly at any power on the dump, we would expect that the ratio between calculations and measurements $C/E = 1$, but this contradicts the experimental data here. Instead, the LMM based calculations predicted systematically more neutrons than found experimentally, especially for the pulses that the deposited beam power were at high power level, as we observed in our former experiment introduced in section 3.2.

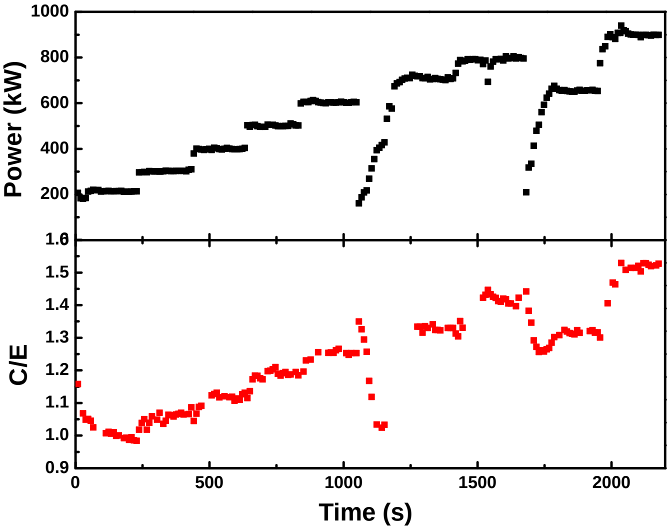

Figure 3.15: (Top) Beam power impinging on the dump as a function of time; (Bottom) Ratio between calculations and measurements as a function of time.

In order to observe the discrepancy between the LMM based calculations and measurements with the change of deposited beam power, the C/E values as a function of beam power have been analyzed, as shown in figure 3.16. The relationship between the two parameters is linear except a few outliers, which correspond to the first few pulses of each experimental day when a full saturation of the deuterium concentration in the dump was not yet reached. A linear fit to the data of figure 3.16 yields $C/E = (7.1 \pm 0.1) \times 10^{-4} Power(kW) + (0.841 \pm 0.008)$.

In this experiment, the deposited beam power on the dump has been obtained with two individual methods by using: the IR camera and the calorimeter. The copper plates are attached to a support structure made of stainless steel tubes that also serve as pipelines for the beam dump cooling circuit. Each block operates therefore as a small inertial calorimeter that stores the heat during the beam pulse and slowly cools down in the pause between beam pulses [131]. The blocks and thermal resistances are designed so that the power deposited in a block during the beam-on phase is approximately proportional to the temperature increase of the block, allowing for easy calculation of the average beam power impinging on a block during the pulse. This gives the possibility to measure beam power separately for the copper plates and then to calculate the deposited beam current on each block. In order to confirm the linear relation between this two methods, deposited beam powers have been compared, as shown in figure 3.17. A good

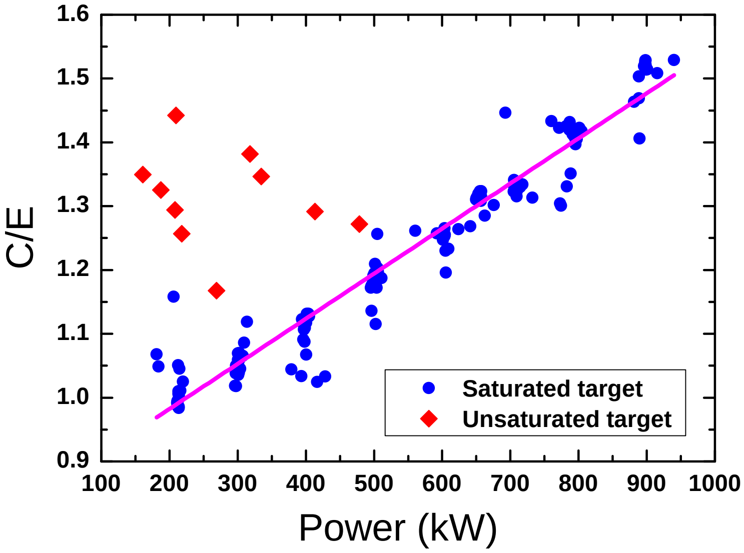

Figure 3.16: Ratio C/E between the calculated and measured neutron emission as a function of the beam power deposited on the dump.

linear fit ($R^2 = 0.965$) has been applied and it shows that the two methods could provide almost the same value (slope = 1.003) independently. That means that the two measured beam powers could provide the same results: the ratio between calculations and measurements (C/E) on a relative scale has been found to exceed unity beyond the observed fluctuation level of the data points at constant power and to scale linearly with the beam power in the range 200 kW to 950 kW.

3.3.2 Implications for SPIDER

In order to understand the results of figure 3.16 a hypothesis has been made that the dominant effect is a reduction of the deuterium concentration at saturation as a function of temperature. Qualitatively, one can expect temperature to promote the diffusion of deuterium in the dump and we here speculate that this is manifested in the different concentration reached at saturation as a function of temperature. The IR diagnostics installed at ELISE determines the difference ΔT between the average temperature of each individual block of the beam dump before and after irradiation. By defining the hypothetical temperature dependent saturation rate (HTDSR) as the concentration at saturation required to exactly match the experimental data at each temperature, the HTDSR as a function of ΔT averaged over the dump surface has been calculated, as shown in figure 3.18. As the concentration at saturation used at a power

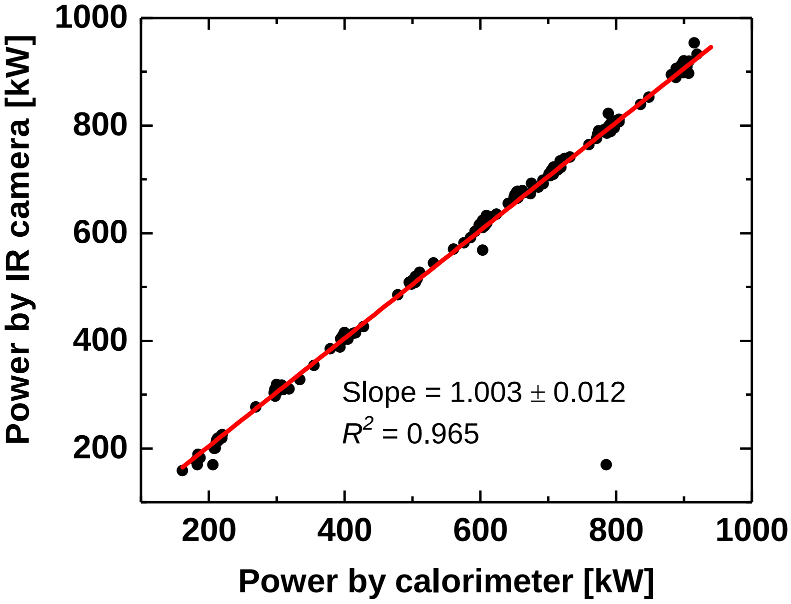

Figure 3.17: Comparison of the beam power impinging on the dump measured by the IR camera and the calorimeter.

of 200 kW is 20%, data show a linear decrease of HTDSR versus ΔT which is described as $HTDSR = -4.35 \times 10^{-4} \Delta T + 0.218$. This formula can be used as an empirical correction for neutron emission calculations at SPIDER.

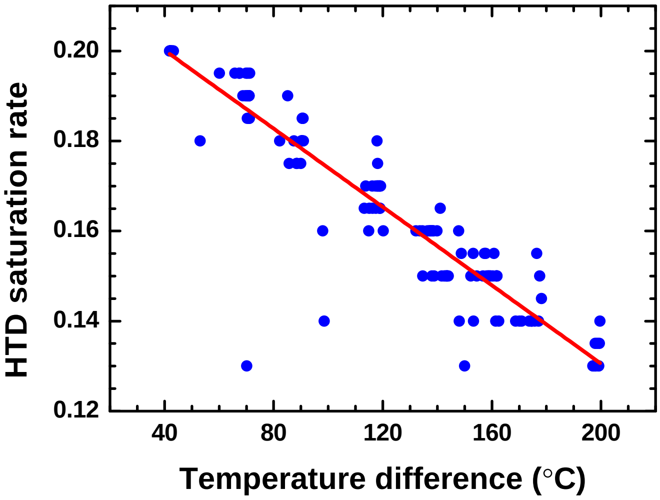

Figure 3.18: The hypothetical temperature dependent saturation rate as a function of the temperature difference after and before the beam impinging.

On the other hand, the dump has always been coated with a suitable black material to overcome the problem of the low copper emissivity which is important for the IR camera for light collection. In ELISE, the side facing the beam is PVD (Physical vapor deposition) coated with Molybdenum Disulde (MoS_2) and will be cleaned and coated again before each campaign. However, the thickness and uniformity of the coating are very hard to be measured precisely and there is no need for measurements with IR camera and the calorimeter. The thickness of the coating is given as about $3\mu m$ in design [122]. The density of natural MoS_2 is 5.06 g/cm^3 [133, 134], but the values for different types of sputtered MoS_2 coating were determined to be about 3.3 - 3.95 g/cm^3 [135], which are significantly lower than the bulk density. Even taking the lowest density (3.3 g/cm^3) in consideration, the projected range of 60 keV deuterium ions in coating would be about 0.62 μm based on TRIM calculation. This means that the incident deuterium lose its whole energy and be trapped in the coating. In order to repeat the LMM based calculations with the MoS_2 material, the deposition profiles of deuterium in coating have been calculated from 27keV to 56 keV with a step of 1 keV. After repeating the calculation and comparison as introduced in section 3.2, the discrepancy between calculations and measurements (C/E) as a function of deposited beam power has been obtained, as shown in 3.19, together with the saturated data shown in figure 3.16. In order to compare the two LMM based calculations, data are normalized with the same pulses (114 s - 209 s). In the calculation based on the neutron production happened in the layer of MoS_2, the concentration rate at saturation was set as 20% as well.

As the density of the sputtered MoS_2 coating was not determined and no study of the deuterium implantation in the coating material has been found, it's difficult to obtain the right density of suitable saturation concentration rate as inputs in the LMM based calculations. For simplification, a reasonable density of 3.5 g/cm^3 was set, and the calculations based on different saturation concentration rates in range 10% to 60% have been performed and compared, as shown in figure 3.20. Calculations were normalized with the data in range 114 s - 209 s, the same period that has been used to normalize data for converting calculations to measurements. We can note that the differences among those calculations are small (within 1%), which indicates that the LMM based calculation by applying any reasonable density or saturation concentration rate is stable for comparing with measurement when the deuterium concentration in target has been reached at saturation.

In SPIDER, the front surface of the dump, with expected temperature up to 350 °C, will be coated with a suitable black molybdenum disulphide coating, i.e. Molykote

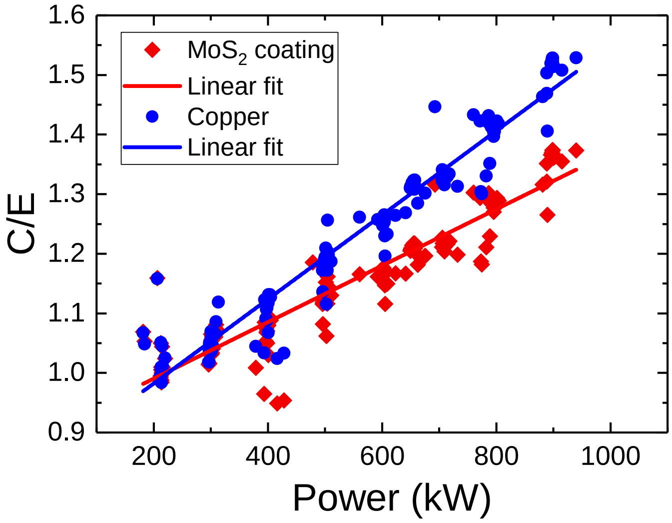

Figure 3.19: Ratio C/E between the calculated and measured neutron emission as a function of the beam power deposited on the dump by assuming that the deuterium deposited the whole energy in the layer of MoS_2 coating (red) or in the copper dump (blue).

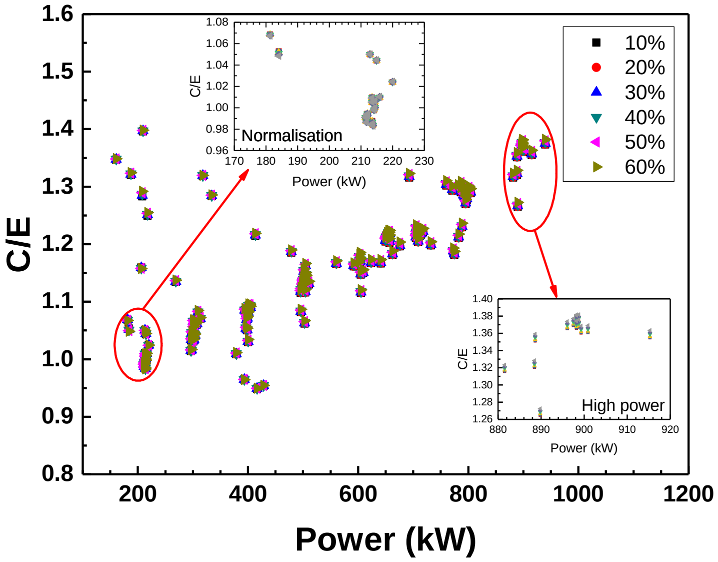

Figure 3.20: Comparison of different calculations based on different saturation concentration rates of deuterium in sputtered MoS_2 coating.

D-321R, made by Dow Corning, to reduce the reflection from the opposite panel [110], and in this case also to overcome the problem of the low copper emissivity, as effectively achieved on ELISE [136]. To this end, considering the similar materials used as the dump and coating on ELISE and SPIDER, a similar calibrated scintillator will also be installed on SPIDER as a neutron emission monitor. The prediction of neutron emission by applying the LMM as introduced in this thesis would be adapted by the empirical corrections based on measured temperature difference that has been observed in this thesis.

Chapter 4

Development of A Telescope Proton Recoil Spectrometer

There is no such thing as darkness,
only a failure to see.
– Malcolm Muggeridge

The principle of neutron detection using a telescope proton recoil spectrometer has been introduced in section 2.3. In order to measure the neutron spectrum on the ChipIr beam line, where complex background and intense fast neutrons exist, some TPR prototypes have been designed for background suppression and been tested at accelerator-based facilities. Double coincidence TPR based on a silicon detector and a YAP scintillator has been first designed for wide energy range neutrons measurement. Triple coincidence YAP scintillator-based TPR confirmed its capacity of neutron spectrum measurement on fast neutron beam line ROTAX. However, as there is no dedicated shielding and a collimator on the ChipIr beam line for the TPR spectrometers and there is no need to build one due to engineering constraints and budget limits, new silicon-based TPR prototypes by considering both with more coincidence and low sensitive volume detectors have then been developed to improve the capabilities on background suppression for intense fast neutron measurement.

4.1 Configurations of telescope proton recoil neutron spectrometers

4.1.1 Design criteria

One of the attractive features of proton recoil telescopes is the fact that their detection efficiency can be calculated quite accurately. Because complications such as multiple scattering or wall effects are largely avoided, the probabilities of neutron scattering and subsequent recoil proton detection are quite easily calculated from the accurately known hydrogen scattering cross section and geometric evaluation of the detector solid angle [2]. However, a TPR spectrometer design can vary a lot upon applications request, e.g.:

- the neutron energy range of interest;
- the energy resolution and detection efficiency required by applications;
- and the background in the measurement environment.

Based on the above requirements demanded by applications, one has to consider the following issues in the design of a TPR neutron spectrometer:

- Choice of proton detectors (type, area, thickness, quantity, etc.);
- Choice of the target (materials, thickness, etc.);
- Experimental arrangements (target-detector distance, the recoil angle θ with respect to incident neutrons, etc.);
- Influence of environment (protons scattering by air, materials close to the beam and detectors, etc.).

These issues are mostly decided by many different factors. Table 4.1 lists the objectives and related main affecting parameters in a TPR design by using a polyethylene (PE) target as a converter for neutron detection.

As shown in equation 2.5, the energy of recoil proton (E_p) that scattered on hydrogen can be calculated easily with incident neutron energy (E_n): $E_p = E_n cos^2(\theta)$. Here θ is the recoil angle of recoil protons with respect to the incident neutrons. The energy of recoil proton decreases with the recoil angle increasing and decreases significantly when recoil angle is larger than 45°. On one hand, one would expect to place the detector with recoil angle as small as it could be, to increase the detectable energy range (extend the low energy threshold) and detection efficiency, but on the other hand, the pulses

Table 4.1: Objectives and affected parameters in a TPR design

Objectives	Main affected factors
Detectable energy range	Recoil angle Detector thickness
Energy resolution	Target thickness Target area Detector area Recoil angle
Detection efficiency	Target thickness Target-detector distance Recoil angle
Pile-up	Recoil angle Target-detector distance Detector property Detector active volume Shielding

pile-up effect and radiation tolerance of the detector with low recoil angle in high intense neutron field have to be considered. The choice of the type of the detectors (ΔE and E) and their thicknesses are decided by the radiation field and the energy range of interest. In general, thick PE target could increase the detection efficiency, but on the other hand, could worse the energy resolution because some produced recoil protons would be stopped or broaden by the PE target itself. The choices of target-detector distance and the active area of the detector are also a kind of compromise upon requested energy resolution and detection efficiency. For measuring the neutrons in a complex radiation field, one also has to consider the shielding, the pulses pile-up effect on detectors, and the choosing of proper type of detectors.

In order to observe how those factors affect the design of a TPR neutron spectrometer, a simple model by discussing the influence of the target and set-up arrangement has been built and simulated by the Monte-Carlo (MC) method-based code MCNPX [137].

4.1.2 MC method-based simulations

In the MCNPX model, a very small (Φ 1 mm) surface neutron source has been modeled as a neutron beam line. A PE target with density of 1.0 g/cm^3 and radius of 2.5 cm has been built as the neutron-proton converter. A spherical surface with its center at the center of the PE target has been used as a detector to count the recoil proton emission from the PE target. The radius of the detector was set as 50 cm, and the spherical has been divided into 19 parts from -95° to 95° to count the flux and spectrum of recoil protons. The schematics of the TPR model is shown in figure 4.1.

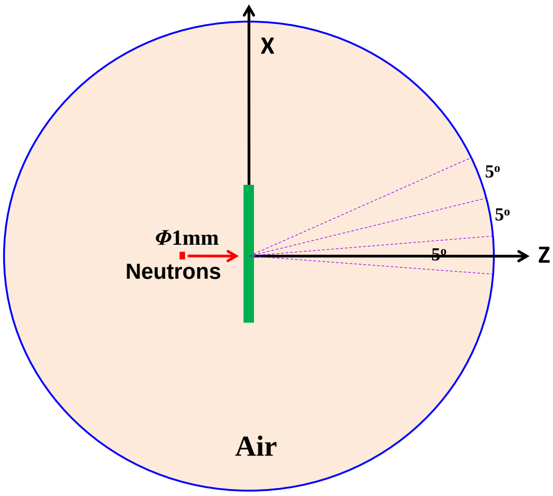

Figure 4.1: Schematics of the TPR model in MCNPX. Neutron flux on the spherical surface have been counted in every 5 degree.

The environment between the detector and the PE target was set as air with a density of 0.001205 g/cm^3 by considering the reality of our later experiments at ISIS. The la150h library [138, 139], which is dedicated for proton transportation, has been employed. The primary energies of neutrons were set from 10 MeV to 100 MeV with a step of 10 MeV. For different energetic incident neutrons, run events with different thick PE targets have been performed. The thicknesses of the PE targets were set as 0.1 mm to 0.6 mm with a step of 0.1 mm, and 0.8 mm, 1.0 mm, 1.2 mm, 1.5 mm, and 2.0 mm, respectively. Figure 4.2 shows the flux of recoil protons as a function of recoil angle (in degree) for different thick PE targets with the incident neutron energies at 20 MeV, 60 MeV, and 100 MeV, respectively. For low energy neutrons, the energy of recoil protons is corresponding low. As the neutron-proton conversion efficiency is low in thin PE targets and more produced protons are stopped in the thick target itself, the detection efficiency is relative low for low energy neutrons with not much affects from the thickness of the target. In general, thick PE target could generate higher detection efficiency than thin target, especially for high energy incident neutrons. This could provide an information for choosing the experimental arrangement and the thickness of the PE target demanded by the detectable energy range and the detection efficiency of interest.

One could also note from figrue 4.2 that the flux of recoil protons drops very fast

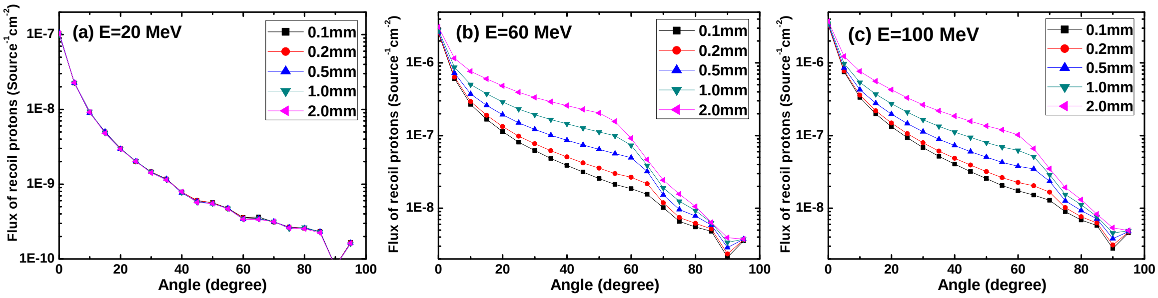

Figure 4.2: Recoil protons flux as a function of degree of the TPR system with respect to the incident neutron beam. Simulations with 20MeV, 60MeV and 100MeV incident neutrons are shown from left to right, respectively.

with the recoil angle in the range 50 ° − 80 °, which is mainly resulted by the feature of the angular distribution of the neutron elastic cross section on hydrogen, as shown in figure 4.3. Here the angular distributions of the H(n, el) reaction cross section for different energetic neutrons, which were extracted from the JENDL-4.0/HE library [140], have been presented. The cross section drops significantly as the recoil angle increases, especially in angle range of 50° − 80°.

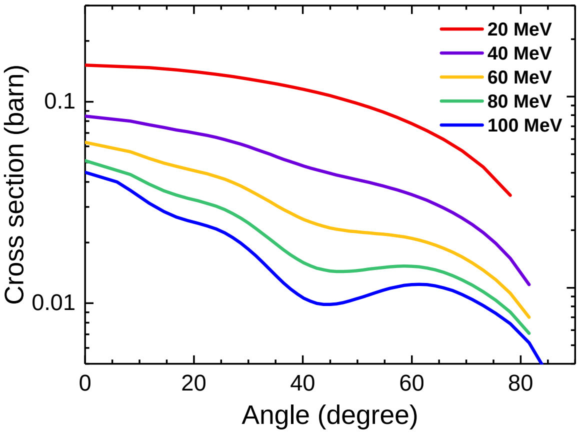

Figure 4.3: The angular cross section distribution of the H(n, el) reaction extracted from the JENDL-4.0/HE library.

In order to observe the energy resolution affected by different thick PE targets, the recoil proton spectrum, which is detected by the detector positioned at an angle of 30 ° with respect to the incident neutron beam line, has been obtained, as shown in Figure 4.4 as an example for 100 MeV incident neutrons. As the solid angle of a cone was chosen as a step of 5 ° to count the flux on sensitive spherical surface which is 50 cm far away from the center of the PE target, the angle and the distance are relative large which correspondingly give a large counting area on the spherical surface and result in a large FWHM of the proton peak contributed by the scattered protons on H on the energy spectrum.

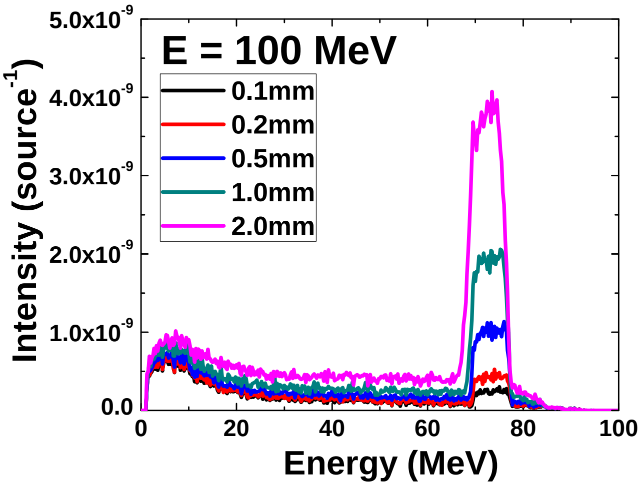

Figure 4.4: Recoil proton spectrum with different PE target thickness at 100 MeV incident neutrons.

In principle, the more thick the PE target is, the more recoil protons will be scattered. Correspondingly, the incident neutrons are moderated, and the recoil protons are more easier to lose energy in the target, both result in the broaden of the FWHM of the recoil proton spectrum. In order to observe the influence of the PE target thickness on detection efficiency, four different recoil angles were chosen to count the flux of recoil protons as a function of the PE target thickness, as shown in figure 4.5. In general, the detection efficiency increases with the thickness of the PE target increases. However, when the detector is placed at a large angle with respect to the incident neutrons, the detection efficiency is more easier reaching to a saturation level as increasing the thickness of the PE target, for instance, as shown in the right bottom figure on figure 4.5 for 30 MeV incident neutrons. In this case, increasing the thickness would not increase the detection efficiency significantly but would worse the energy resolution.

With the general analysis of a MC simulation model for designing a TPR neutron spectrometer, some choices for making a real TPR neutron spectrometer, e.g. the thickness of the PE target, the angle of the detector placed with respect to the incident neutron beam line, and the interested detection energy range etc., can be preliminary determined upon the requests by applications. By using the projected range data of protons in some materials provided by the SRIM code, the thickness and materials of the detectors can also be chosen. To this end, considering the environment (complex

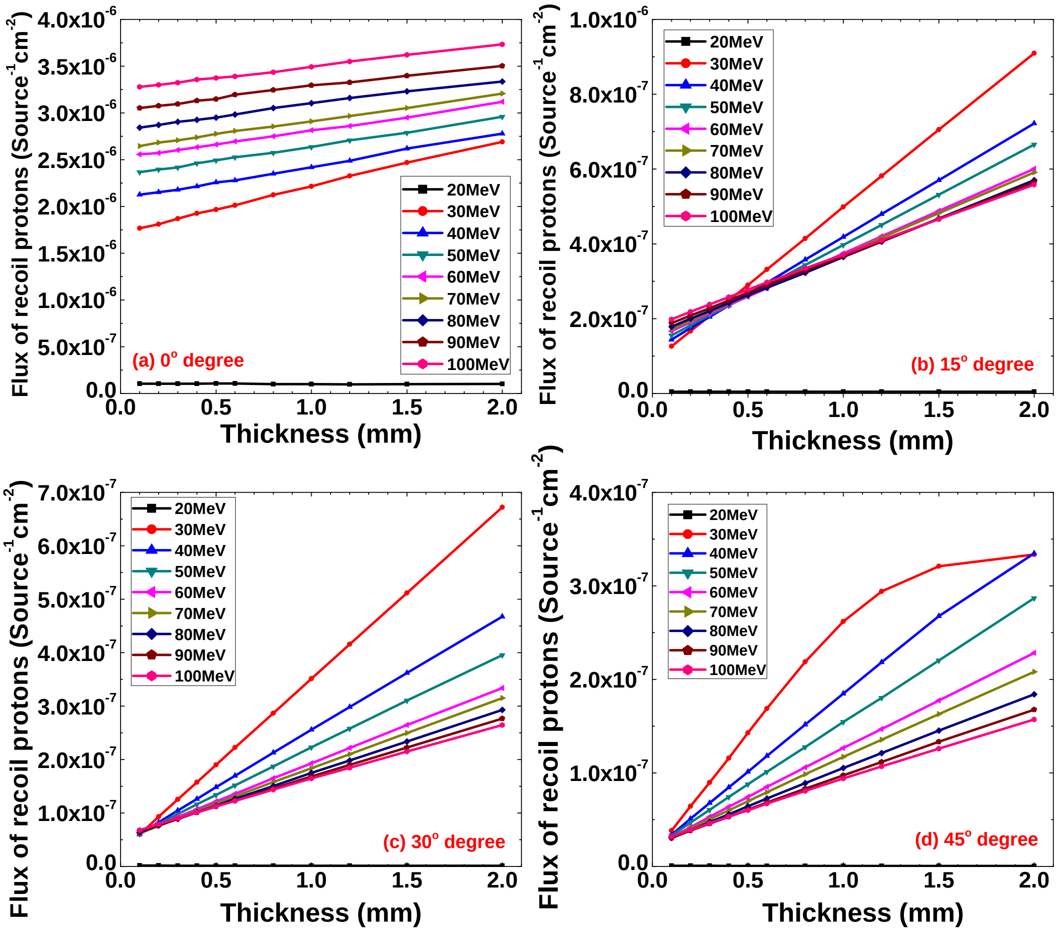

Figure 4.5: Flux of recoil protons as a function of PE target thickness at positions of $0^\circ, 15^\circ, 30^\circ$ and 45° with respect to the incident neutron beam.

radiation field, wide energy range of neutrons, no dedicated collimator in experimental hall for detectors, high intensity fast neutrons, etc.) on the ChipIr beam line, two types of TPR neutron spectrometers, one is based on silicon detectors as ΔE detectors and a YAP:Ce (Yttrium Aluminium Perovskite (Cerium)) scintillator as E detector (called scintillator-based TPR spectrometer in the following), and the other one is based only on silicon detectors (called silicon-based TPR spectrometer in the following), have been designed and tested.

4.1.3 Scintillator-based TPR spectrometer

The scintillator-based TPR neutron spectrometers are using silicon detectors as the ΔE detectors and a YAP:Ce (YAP in the following) scintillator as the E detector. Two prototypes, one is consisting of a 500 μm thick surface barrier silicon detector together with a 2.54 cm thick YAP scintillator, and the other one is consisting of a 500 μm thick surface barrier silicon detector, a 1000 μm thick surface barrier silicon detector, and a 2.54 cm thick YAP scintillator, respectively, have been built for different capabilities on background suppression by performing coincidence analysis. The cylindrical YAP scintillator has a diameter of 2.54 cm and a thickness of 2.54 cm. YAP scintillator has a fast decay time (25-30 ns), which can be utilized to minimize pileup for operations at high background counting rates (say, 100 kHz - 1 MHz background induced by environmental γ-rays) [141,142], and a good stopping power with a density of 5.37 g/cm^3, which can be used for spectrum measurements of a wide detectable energy range to charged particles (e.g. protons). The 2.54 cm thick YAP scintillator could completely stop about 115 MeV protons based on the SRIM code calculation, which corresponds to 230 MeV neutron if the detector is place at an angle of 45° with respect to the incident neutrons. The most important reason that we apply a YAP scintillator as the E detector for neutron detection on the ChipIr beam is the good capability of its radiation damage tolerance, which could make the TPR spectrometer a long-term monitor for neutron spectrum measurements.

As the scintillator-based TPR spectrometers have the ability to measure high energy neutrons, the first silicon should be thick enough otherwise the produced high energy protons will pass through it and deposit a few energy with which one cannot specify the signals from the electronic noise [143]. However, on the other hand, low energy recoil protons cannot pass through a thick ΔE detector, which then increase the low detectable energy threshold. In order to choose a proper thick silicon detector as the ΔE detector, some MCNPX code-based simulations of the response of different thick silicon detectors to protons have been performed. Figure 4.6 shows the deposited energy on different thick silicon detectors as a function of incident proton energy. By evaluating the noise level of the 300μm and 500μm thick silicon detectors in measurement circumstance, the minimum energy deposition to get a clear proton signal should be at least 0.6-0.7 MeV. As the scintillator-based TPR spectrometer could measure protons up to 115 MeV, by inserting the energy threshold line (red dash line on figure 4.6), the thickness of the first silicon detector was chosen as 451 μm, the one we have so far in the lab with thickness closing to 500 μm, for the two scintillator-based TPR prototypes.

The low detectable proton energy threshold using the scintillator-based TPR prototypes depends on the thickness of the silicon detector. As the thickness of the first silicon detector was about 500 μm, then the low energy threshold was determined as about 8

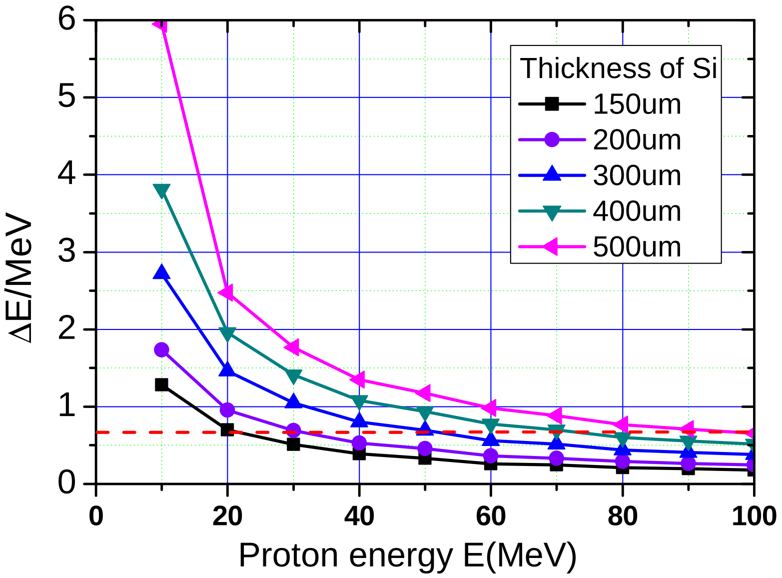

Figure 4.6: MCNPX calculation of energy deposited on different thick silicon detectors as a function of incident proton energy.

MeV, which is the minimum energy for a proton to be transmitted by silicon, excluding the energy lost in air and aluminum foils that we used to shield the light and electromagnetic noise. Without considering the PSD that could be applied to separate protons from other particles on the silicon detector and then to lower the detectable energy threshold, the proton energy range that could be achieved using the scintillator-based TPR was about 9 MeV to 110 MeV.

4.1.4 Silicon-based TPR spectrometer

The silicon-based TPR prototype, which consisting of 4 different thick silicon detectors, was designed with low sensitive volume and multi-coincidences for intense background suppression. The thicknesses of detectors from the first one facing to the PE target are 219 μm, 340 μm, 451 μm and 1022 μm. As the silicon detector can easily be damaged by neutrons, it's not suitable for long term measurement of the neutron spectrum on the ChipIr beam line, where high intense radiation especially neutrons exist. However, as there is no dedicated collimator so far for neutron spectrum measurement, the signals on large volume detector (e.g. YAP scintillator we introduce in the last subsection (4.1.3)) would be saturated and cannot be separated by common PSD analysis. To this end, full silicon detector-based TPR spectrometer could be applied as the low volume and low detection efficiency of silicon to neutral particles, e.g. neutrons and gamma-rays.

With the projected range of protons in different thick silicon detectors calculated by the SRIM code, the detectable proton energy range using the silicon-based TPR spectrometer was determined as 5 MeV to 28 MeV.

4.1.5 Advantages and disadvantages

The dominant disadvantage of the proton recoil telescope is its extremely low detection efficiency (typically one count per $10^3 - 10^6$ incident neutrons), but on the other hand, the low detection efficiency shows the capacity of high intense neutrons detection. This low efficiency stems from two factors, neither of which can be improved without sacrificing energy resolution of the device. First, the thickness of the target (e.g. PE converter) must be kept small to avoid appreciable energy loss of the recoil protons before they leave the target. Usable thicknesses lead to a probability of about $10^{-4} - 10^{-3}$ that the incident neutron undergoes a scattering event within the target. Second, the solid angle subtended by the recoil proton detectors must be kept relatively small to avoid including too large a spread in recoil angles, and consequently smearing the peak response function.

One of the attractive features of TPRs, as we introduced in section 2.3, is the fact that their detection efficiency and response to neutrons can be calculated quite accurately, which gives a simple way to unfold the neutron spectrum and flux. Besides, by performing the coincidence analysis, the background can be suppressed efficiently and particles can be discriminated clearly by using a TPR spectrometer in complex radiation field.

Table 4.2 shows the comparison of advantages and disadvantages of TPR neutron spectrometers and the two types of TPR neutron spectrometers that used in this thesis. In priciple, the two types of the TPR neutron spectrometers could compensate each other for measuring the neutron spectrum on the ChipIr beam line, where a complex and intense radiation environment without a dedicated collimator exists.

4.2 Scintillator-based TPR spectrometer

Before testing the scintillator-based TPR spectrometers on the fast neutron beam lines, e.g. ChipIr, the response of the used silicon detectors and the YAP scintillator to

Table 4.2: Main advantages and disadvantages of a TPR neutron spectrometer

	Main advantages	Main disadvantages
TPR spectrometer	a, simple response function to neutrons; b, accurate detection efficiency; c, background suppression; d, charged particles discrimination.	a, low detection efficiency; b, high detectable lower energy threshold.
Scintillator-based TPR	a, wide energy range; b, good radiation damage tolerance.	a, sensitive to n, gamma-rays.
Silicon-based TPR	a, non-sensitive to neutrons; b, background rejection with more coincidences	a, short energy range; b, easily be damaged by neutrons.

protons should be charactrized first. Especially the YAP scintillator, in which different energetic protons have different penetration depth (the position of brag peak), the light collection for different energetic incident protons could not be linear to deposited energy. In order to characterize the performance of the YAP scintillator to protons, some tests have been previously performed at the Uppsala tandem accelerator in the energy range 4-8 MeV [142] and at the Legnaro Tandem ALPI-PIAVE accelerator in 9-20 MeV energy range [144]. To extend the characterization of the light yield of the YAP scintillator to a higher energy and check the linearly response to protons, the scintillator-based TPR spectrometer consisting of a 451 μm thick silicon detector and the 2.54 cm thick YAP scintillator has been tested with up to 80 MeV protons from the cyclotron accelerator at the INFN-LNS, Catania, Italy.

4.2.1 Response of a YAP scintillator-based TPR to protons

1. Experimental setup

The measurements have been performed with 62 MeV and 80 MeV proton beams using the cyclotron accelerator at INFN-LNS. Some aluminum (Al) foils with different thicknesses have been used to reduce the energy of protons impinging on the TPR spectrometer and to obtain measurement points in the 5-80 MeV range. As the flux of the direct proton beam would be too intense to measure, a Rutherford scattering configuration has been used to reduce the flux on detectors. This was obtained by using a 0.25 mm thick polyethylene target as a scatterer to produce recoil protons from the primary beam. The TPR neutron spectrometer was then placed at a distance of 30.5 cm from the target with an angle of about 27° with respect to the incident proton beam, as shown in figure 4.7. The angle was chosen to be large enough so that the detectors and their supporting structures did not intercept the beam but, at the same time, so to ensure a high enough signal (deposition energy) on the detector.

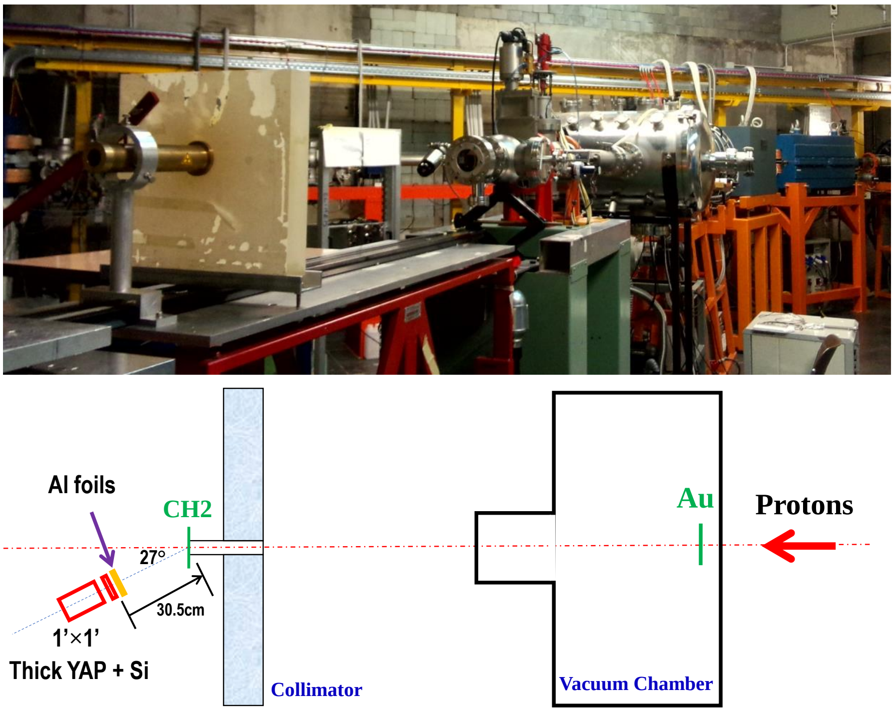

Figure 4.7: Experimental set up of the TPR spectrometer in INFN-LNS. Top: the picture of the set up, the TPR is not shown here; Bottom: schematic diagram of the experimental arrangement. The primary proton beam passes through a fixed golden target in a vacuum chamber and incident on the PE target, then it will be scattered and partially be detected by the TPR prototype.

The entrance of the YAP scintillator was covered by a $30\mu m$ thick Al foil for the optimization of light collection. The Si detector was also covered by a layer of $30\mu m$ thick Al foil on two sides to shield from light and electromagnetic noise.

The YAP scintillator was coupled to a Hamamatsu R9420-100-10mod PMT and operated with negative voltage at 650 V so to cover the whole proton energy range. The Si detector was equipped with a current preamplifier (CIVIDEC C2 [145]). This 40 dB Broadband Amplifier is a low-noise current amplifier with an analog bandwidth of 2 GHz. Its speed and radiation hardness are optimized for use as a front-end amplifier. The detector is reverse biased at +170 V. All signals recorded on the two detectors were fed directly into a 14 bit, 500 MSamples/s digitizer (CAEN DT5730 [146]) and were saved by triggering the signals on YAP scintillator. The waveforms are then analyzed off-line for coincidence and pulse height analysis.

2. Coincidence measurements

Two events, recorded by the Si detector (ΔE) and by the YAP:Ce scintillator (E) with the same trigger, are considered to be coincident if the time interval Δt between them falls within an acceptance window. The center of this time window T_c was determined by observing the peak which stands out from a continuum of random coincidences in a histogram of Δt vs coincidence events. Figure 4.8 shows an example of determining the time window for choosing the true coincident events.

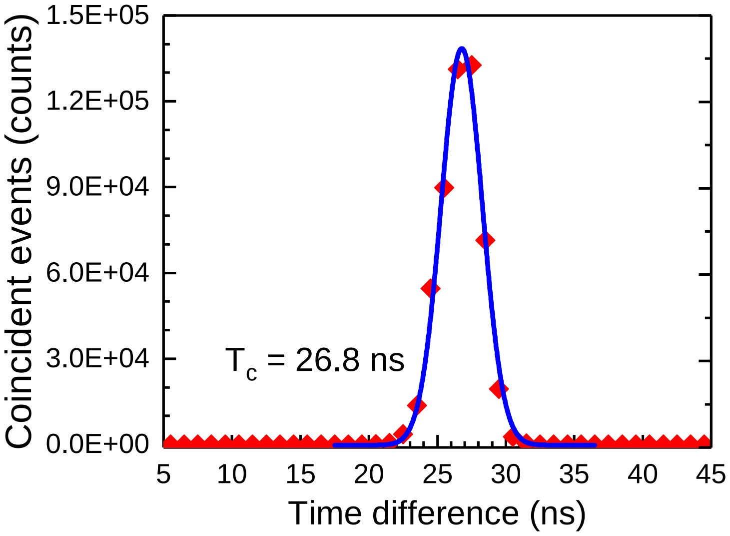

Figure 4.8: Coincident events as a function of time difference between the two signals on the two detectors.

For each measurement event at primary proton energy at 62 MeV and 80 MeV, the time difference T_c for picking the true coincident events has been determined from about 26 ns to 34 ns, with corresponding widths of 10 ns to 12 ns. As the length of two signal cables used for the two detectors were almost the same, then the time difference between the two signals on the two different detectors was mainly resulted by the electron transit time in the PMT, which usually ranges from 20 to 80 ns in various PMT design [2].

The energy deposited by charged particles on the two detectors allow to produce identification (ID) maps mathematical described by the Bethe formula [16, 95], where the bending radius of each ID depends on the charge and mass of the ion species. This makes particle identification possible, such as shown by the $\Delta E - E$ contour plot in figure 4.9. Here we can easily distinguish protons as main contributors to the most intense ID, which stands out from a structure-less background due to γ-rays. Above the proton signature, there are then other particles which are separated by the different charge and mass: deuterons, tritons, ^{3}He and α. The intensity of these signatures is, as expected, less pronounced than protons, as the lower interaction cross section compared to nuclear elastic scattering and higher stopping power in air, Al foils, and Si detector.

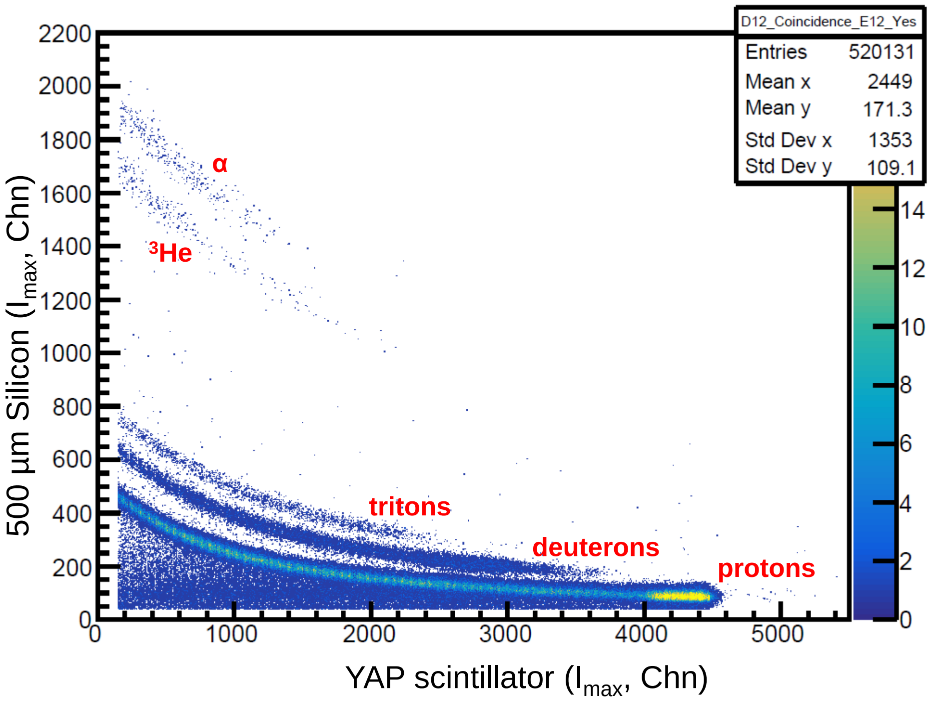

Figure 4.9: $\Delta E - E$ contour plot of coincidence events measured by the TPR. Elongated structures ("bananas") due to particles produced from the interaction of protons with the polyethylene target can be clearly seen.

3. Pulse height spectra analysis

Pulse height spectra (PHS) on the YAP scintillator were obtained after coincidence analysis. Figure 4.10 shows the PHS with incoming protons at 62 MeV and 80 MeV without any Al foils in front of the spectrometer. The most important feature of the PHS is the peak at the maximum pulse height position, that is the contribution of proton elastic scattering on carbon ($Peak_C$). The contribution of scattering on hydrogen ($Peak_H$) and inelastic scattering on carbon can also be observed. As $Peak_C$ has the highest energy and best resolution, the center of the peak has been used to determine the relative light yield of the YAP:Ce detector as a function of the incident proton energy. However, one can also note that the shape of the peak is not Gaussian, which could be resulted by a non-well collimated beam [144]. Detailed analysis reveals that it was resulted by protons scattering on air. The statistical error on the PHS position $Peak_C$ is about 0.5-2.3%.

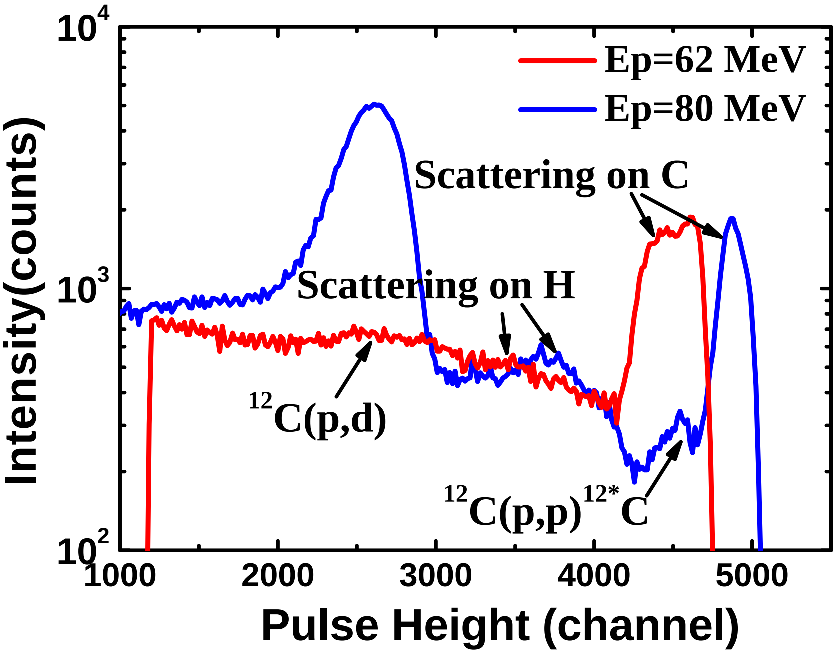

Figure 4.10: Measured PHS on the YAP scintillator with 62 MeV and 80 MeV proton beams.

In order to improve the accuracy on determining the center of the proton peak, which is contributed by protons scattered on C, the PHS has been analyzed by fitting the highest energy peak with Gaussian functions. Figure 4.11 shows an example of a fit for a measurement with 80 MeV protons. In the analysis of each PHS we considered components due to: a) elastic scattering on carbon and on hydrogen; b) inelastic scattering on carbon; c) scattering on air and d) a continuous background that is empirically described by a polynomial. The position of the ^{12}C elastic scattering peak is the most important parameter as it is used to determine the relative light yield. At an energy lower by 4.44 MeV with respect to the ^{12}C elastic scattering peak we then found a further peak from inelastic scattering on carbon, where the energy difference corresponds to the first excited state of the ^{12}C nucleus. As Oxigen and Nitrogen have higher masses than ^{12}C, scattering by air determines a barely visible peak at even higher energies than scattering on carbon. Concerning the peak broadening, kinematics predicts wider peaks when scattering occurs on lighter elements. This is why the elastic scattering peak on hydrogen is significantly larger than that on ^{12}C.

4. Light output of the YAP scintillator

Some Al foils of different thicknesses were placed in front of the TPR system to obtain

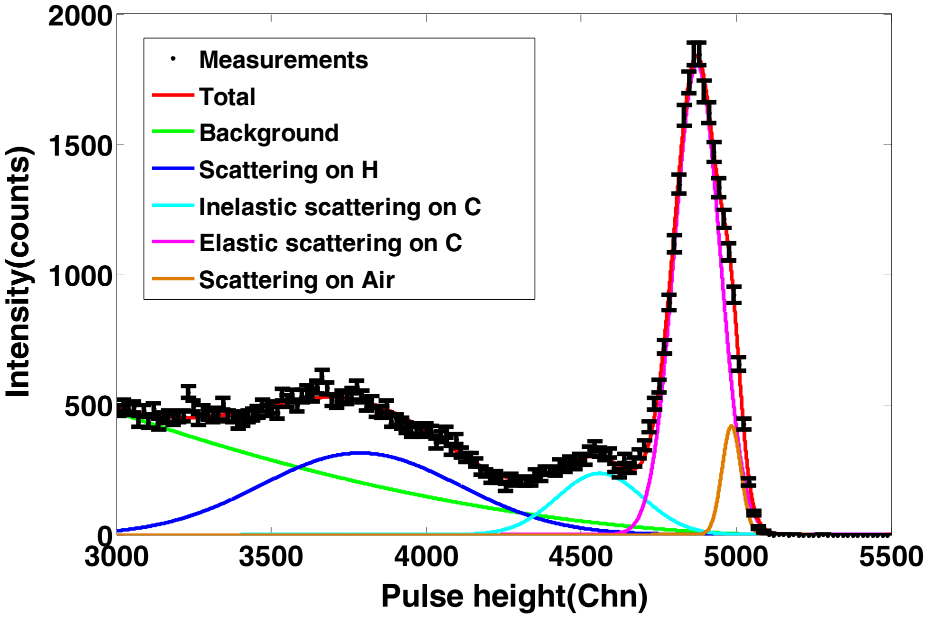

Figure 4.11: Fit of the experimental data with different components that contribute to the measured spectrum, as indicated in the legend. An empirical polynomial fit is used to described the background.

a range of different proton energies on the TPR from the two beam energies (62 and 80 MeV) available with the cyclotron accelerator. The proton deposition energy on the YAP scintillator after passing through the Al foils has been calculated with two independent methods that were found to be consistent. The first method was the simulation using the MCNPX code by employing the la150h library. This determines the transport of protons including scattering on the target and struggling in the Al energy degrader and air. With the second method, the energy of the scattered protons on carbon (on polyethylene) was derived analytically based on the kinematical scattering model (see equation 2.5). Proton energies lost in air, target, Al foils and silicon detector were determined based on the Pstar library [147] together with using the iterative method. In this way, each type of materials between the primary proton beam and the YAP scintillator have been divided into many very thin layers to calculate the residual energy of proton after passing through each layer. The two methods provided consistent results within 1%, as shown in figure 4.12.

In order to obtain the relation between the proton deposition energy on YAP scintillator and its relative light yield, the PHS with an energy scale must be provided. In this experiment the equivalent electron energy (MeV_{ee}) scale has been adopted so that the light yield for protons at an energy E_p is expressed relative to γ-rays of same energy

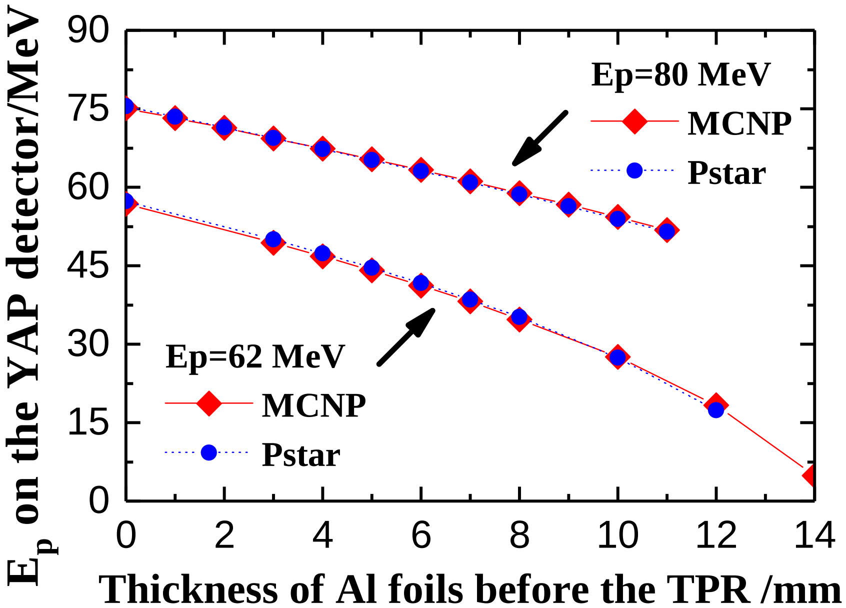

Figure 4.12: Calculated proton deposition energy on the YAP scintillator after passing different thick Al foils placed in front of the TPR prototype.

$E_\gamma = E_p$. To this end, we have calibrated the PHS with ^{137}Cs (0.662MeV) and ^{60}Co (1.17 and 1.33 MeV) γ-ray sources prior to the proton measurements. A linear relation between pulse height in channels (Chn) and the electron equivalent energy (E_{ee}) $E_{ee} = 1.05 \times 10^{-2} Chn - 0.02$, as determined by the γ-ray calibration and shown in figure 4.13, has been used to calibrate the PHS.

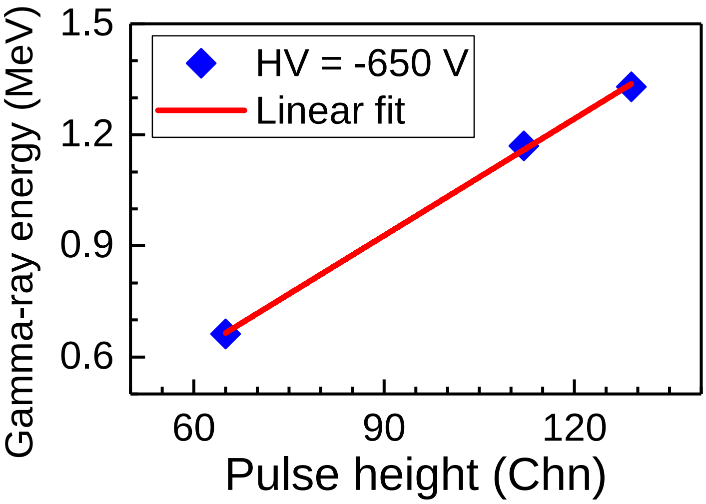

Figure 4.13: Calibration of the YAP scintillator using ^{137}Cs and ^{60}Co γ-ray sources at -650 V voltage supply and its linear fit.

With this input, from the center position of the ^{12}C elastic peak in the PHS and in MeV_{ee} units, the curve of the relative light yield of the YAP scintillator as a function of the proton energy has been determined, as shown in 4.14. We find that the relative yield is linear for the set of data obtained with beam energies of both 62 MeV ($R^2 = 0.9988$) and 80 MeV($R^2 = 0.9989$).

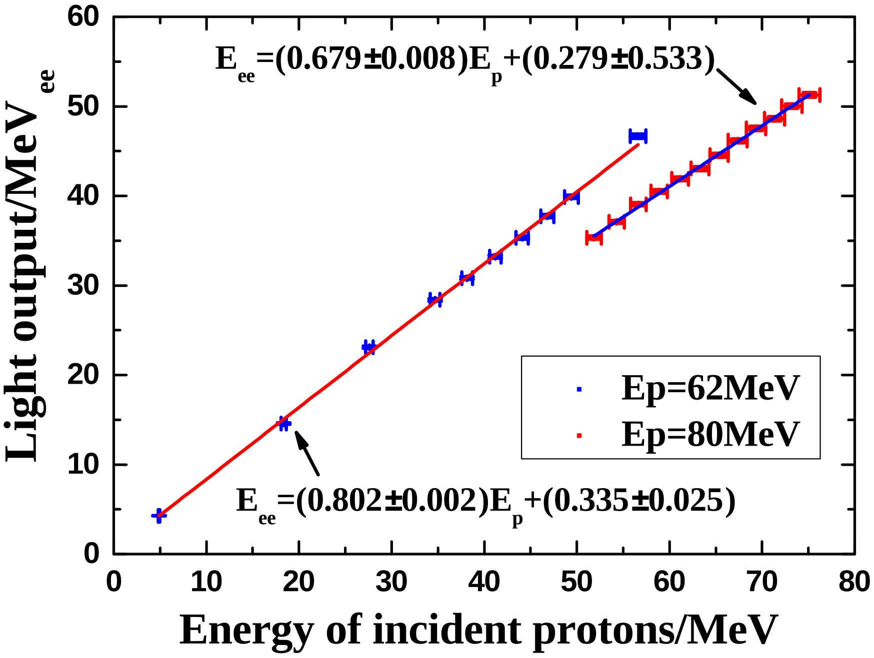

Figure 4.14: Light yield of the YAP scintillator as a function of the proton energy.

Even though the slopes differ for the two data sets, measurements obtained with a proton beam of 62 MeV show a relative light output of (80.2±0.2)%, while measurements obtained with a proton beam of 80 MeV provide a relatively reduced light output of (67.9 ± 0.8)%. After an analysis of the possible causes we concluded that the problem was a shift of the PMT gain from the first to the second set of measurements, that were performed on different days. The calibrations with gamma sources were done on the same day as the first set of measurements, so it is reasonable to assume that the relative yield determined with these data is the most accurate. As changes of the PMT gain are important and have been already observed in the measurements reported here, a radioactive pulser, which is placed on the surface of the PMT and inside the YAP detector, has been implemented to monitor the long term stability of the PMT in the later tests of the scintillator-based TPR prototypes.

Besides, as the preamplifier we used for good pulse sharping was current type, the deposited energy on the silicon detector was proportional to the area of generated pulses.

In order to deal with the pile-up in intense field measurement, the relation between the area of each pulse and its PH has been studied, as shown in figure 4.15. Here we note that the PH is proportional to the area of each proton pulse, which means that the PH of each pulse is also proportional to the deposited energy of the incident proton. In the later TPR prototype test, the PH analysis has been applied for coincident analysis.

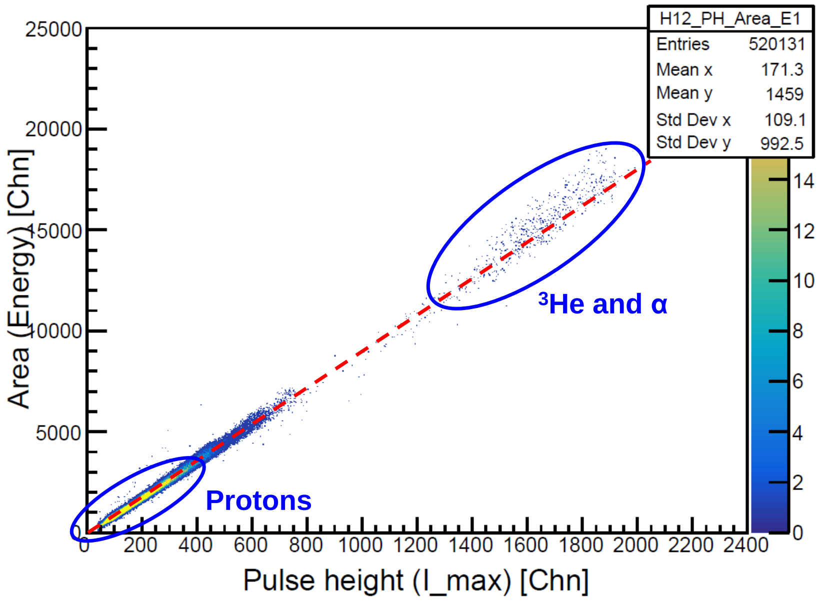

Figure 4.15: The relation between the area of each pulse and its PH.

4.2.2 Double coincidence TPR spectrometers

As there is no dedicated collimator designed for the neutron spectrum measurement in the experimental hall on the ChipIr beam line, two prototypes of double coincidence TPR spectrometers have been designed and tested to characterize the response of YAP scintillators to background in high intense neutron/gamma field. The first prototype, which is called thick TPR in the following, consists of a 451μm thick silicon detector and a 2.54 cm thick YAP scitillator. This TPR prototype has been characterized with up to 80 MeV protons as introduced in subsection 4.2.1. The other prototype consists of a 340μm thick silicon detector and a 2 mm thick YAP scitillator, the later one could fully stop protons up to 27 MeV but has only one-twelfth sensitive volume to the 2.54 cm thick one.

The two prototypes have been test on the ChipIr beam line and the experimental arrangement is shown in figure 4.16. The polyethylene (PE) scatter (target), which was used to convert neutrons to recoil protons, was 1.2 mm thick and placed at the axis of incident neutrons. Two TPR prototypes were positioned at an angle of 45° with respect to the incident neutrons. The distance between the center of the PE target and the first silicon detector was about 27 cm.

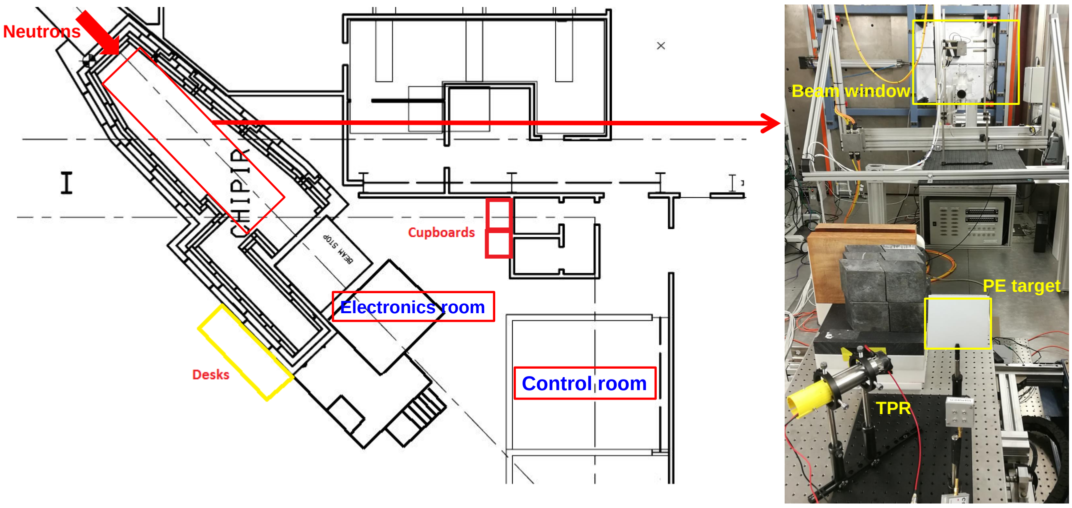

Figure 4.16: Experimental arrangement of the double coincidence scintillator-based TPR prototypes test on the ChipIr beam line.

Two YAP scintillators were coupled with Hamamatsu R9420-100-10mod PMTs and operated with negative high voltage at -650V for the thick YAP ($\phi 2.54 \times 2.54$ cm) and -700V for thin YAP ($\phi 2.54 \times 0.2$ cm). The used two silicon detectors for the two TPR prototypes were equipped with two low-noise current preamplifiers (CIVIDEC C2). Silicon detectors were operated with positive high voltages at +100 V and +170V for $300\mu m$ and $500\mu m$ thick silicon detectors, respectively. The test of each TPR prototype was separately, e.g. every time only one TPR prototype was measuring, as shown in figure 4.17. Both of the signals from the PMT and the silicon detector were fed directly into a 14 bit, 500 MSamples/s desktop digitizer (CAEN DT5730).

As we introduced in subsection 1.3.1, the 800 MeV proton beam at ISIS has a repetition frequency of 50 Hz and a double bunch fine structure. The two proton bunches are about 70 ns wide (FWHM) each and 322 ns apart. In this experiment, a 4060 ns long waveform was triggered by a signal from the proton beam line for each ISIS pulse, and the data has been stored for both detectors (ΔE and E) at the same time. This means that even if the global count rate is relatively low (50 Hz), the instantaneous counting rate can be very high ($>$ 1 MHz): more than one signal pulse is typically present in the time window, and pile-up would be an important issue for the YAP scintillator. Figure

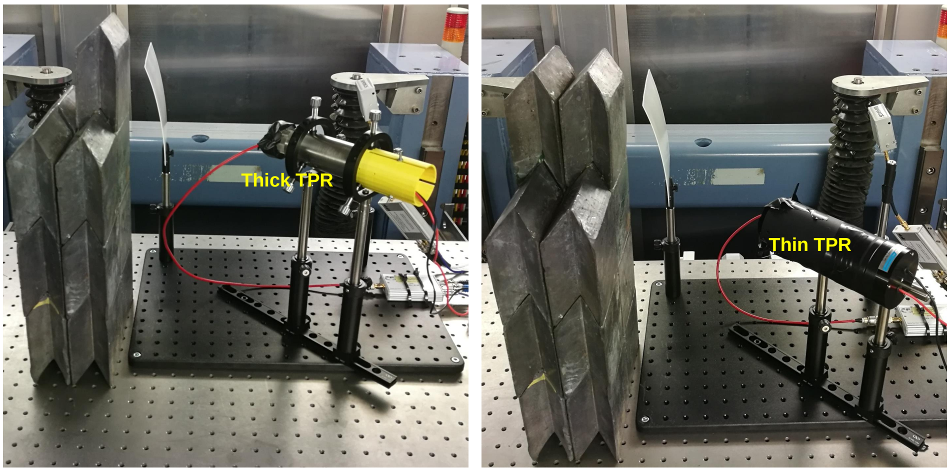

Figure 4.17: Pictures of the two sets of scintillator-based TPR spectrometers. Left: Thick TPR (500 μm Si + 2.54 cm thick YAP scintillator); Right: Thin TPR (300 μm Si + 2 mm thick YAP scintillator).

4.18 shows an example of waveforms on the two detectors of the thick TPR. The x axis is the pulse length (in points) recorded by the DT5730 digitizer, which digitizes signals in every 2 ns (interval between two adjacent points here). Two bunches of signals can be easily seen from the waveform on the YAP detector. Neutrons produced in each bunch didn't always generate a pulse on the silicon detector but many signals were detected by the YAP scintillator. The pile-up was very serious on the thick YAP scintillator and that would be resulted by the scattered neutrons and γ-rays.

As no dedicated collimator and shielding can be used inside the experimental hall on the ChipIr beam line, some polyethylene materials and lead bricks were placed in front of the TPR prototype to reduce the scattered neutrons and gamma-rays from the upstream direction, as shown in figure 4.16. The beam size was also changed trying to control the influence from background events. The operations are shown in Table 4.3. Run 2 - Run10 events are for thick TPR measurements and Run 11 - Run 14 events are for thin TPR measurements:

Off-line analysis is needed for coincidence measurements with the two sets of TPR spectrometers to analyze the pulses on YAP from pile-up effect. A self-defined threshold for each recorded waveform has been set and only the first pulse was set as an effective pulse for PH analysis if there were some pulses piled up. Pulses on the two detectors recorded by the same trigger were considered to be in coincidence if the time difference between two effective pulses falls inside a selected Δt window. In order to reduce the probability of random coincidences, the Δt window must be set as short as possible.

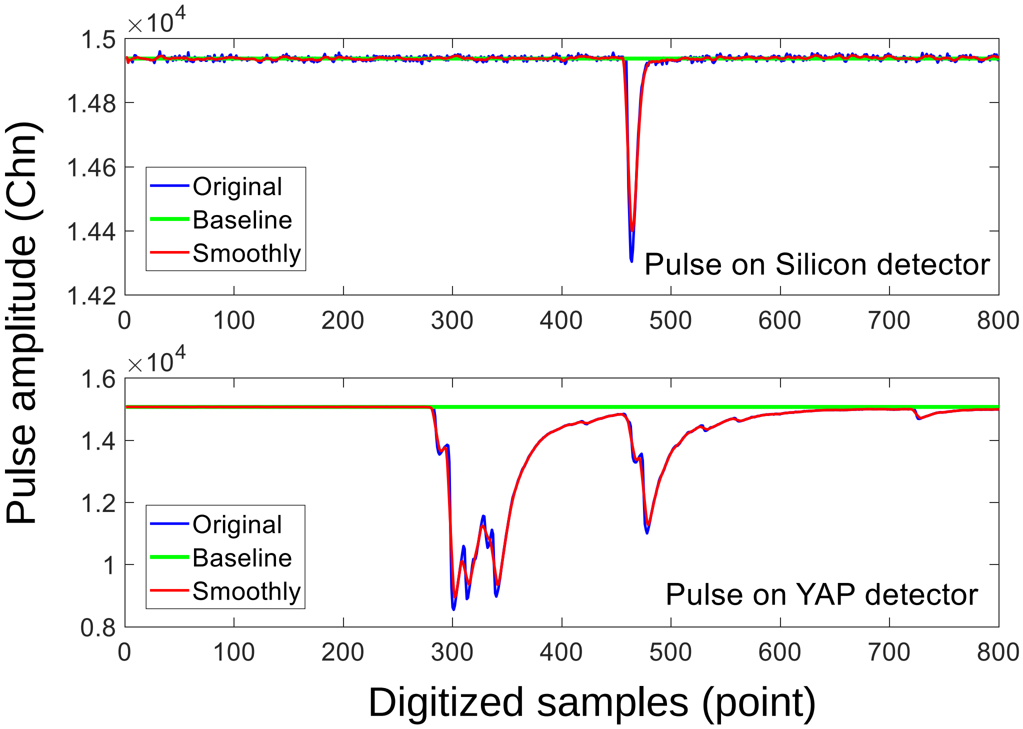

Figure 4.18: An example of pulses on the thick TPR.

Table 4.3: Experimental arrangements

Run event	HV on PMT	Polyethylene target	Acquisition Time(sec)	Integrated beam current(uAh)	Remarks
Run 2	-650	Yes	2304	16.576	
Run 3	-650	Yes	4356	54.486	
Run 4	-650	Yes	3888	45.766	
Run 5	-650	Yes	50616	561.99	
Run 6	-650	NO	4500	49.939	No target
Run 7	-650	Yes	6360	71.151	Table and lead moved
Run 8	-650	Yes	4440	49.867	
Run 9	-650	Yes	1399	15.967	No shielding
Run 10	-650	Yes	1200	13.960	Only Lead
Run 11	-700	Yes	2160	24.581	Detector was not aligned
Run 12	-700	Yes	2520	28.597	Detector was corrected
Run 13	-700	NO	3900	32.322	No target
Run 14	-700	Yes	37020	399.10	Long term

The Δt window is not centered to zero since different time delays are introduced by the PMT, cables and preamplifiers, etc. The center of the time window T_c for selecting true coincident events was found using a routine that counts the number of coincidence events as a function of time difference of pulses on the two detectors. Here we first counted the number of pulses on each detector and then used the time of each pulse (the time of maximum PH) on YAP scintillator to minus the time of each pulse on Silicon detector. Then the coincident events as a function of time difference between them have been obtained for each run event, as shown in figure 4.19 for Run 5, i.e. long-term test of the thick TPR with a PE target as a scatter.

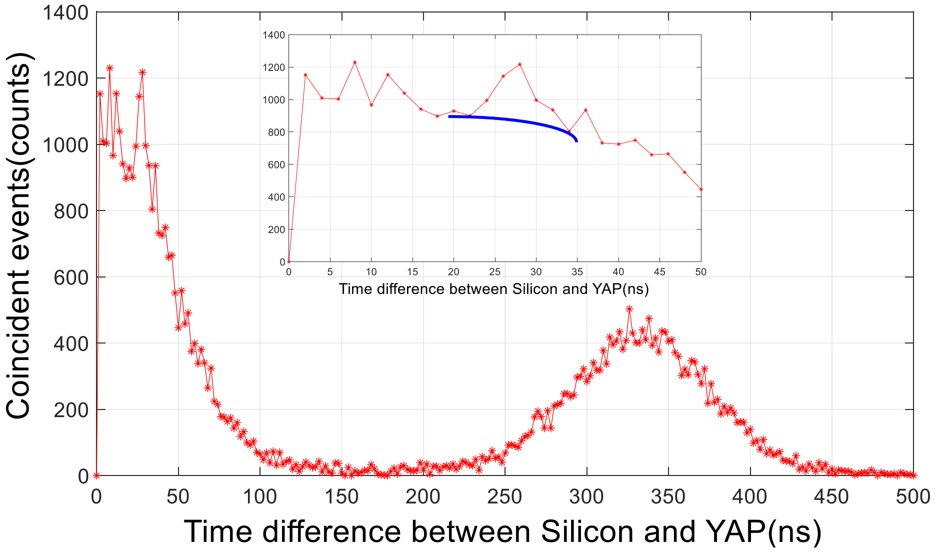

Figure 4.19: Coincidence events between the pulses on YAP detector and Silicon detector as a function of their time difference.

We first can note from figure 4.19 that there is a main peak with its center at about 340 ns. This peak was contributed by the pulses generated by the two bunches of proton beam, i.e. there was a pulse on the YAP scintillator during the second bunch, and at the same time, there was also a pulse produced by the first bunch protons on the silicon detector. In data analysis, we can also observe the other peak with its center at about -340 ns (not shown in figure 4.19). However, the random coincident events raise a large peak instead of showing a continuum background as shown in figure 4.8. Considering the length of used signal cables for silicon and YAP scintillator were almost the same, then the time difference between the two detectors should be in range 20-80 ns, which is mainly resulted by the electron transmit time in PMTs. Here we note that there is a small peak raising upon the random coincident events at around 30 ns. By zooming in this area, the time window for selecting true coincident events has been centered at 28 ns with a width of about 6 ns. At the same time, the true coincident rate, which is the ratio of true coincident events to the whole coincident events during the time window, has been evaluated at about 14%. In this case, the true coincident events, which are needed for obtaining the neutron spectrum, cannot be obtained because most of the selected coincident events are contributed by random events.

By analyzing the test data of the thin TPR, a little higher true coincident rate than the thick TPR has been found, as about 19%-23%. However, those low true coincident rates are far away in application for neutron spectrum measurements. This could be that, on one hand, there is no dedicated shielding and a collimator for the TPR spectrometer on the ChipIr beam line, on the other hand, two coincidence could be not enough for a good background suppression in intense neutron/gamma-rays field. As there is no need to build a dedicated collimator due to engineering constraints and budget limits, new TPR prototypes by considering either with more coincidence or low sensitive volume detectors (or both) have to be developed to improve the capabilities on background suppression for intense fast neutron measurement.

4.2.3 Triple coincidence TPR spectrometers

In order to improve the ability of signals coincidence and background compression, a triple coincidence type of scintillator-based TPR spectrometer has later been designed. Considering the wide detectable energy range provided by the scintillator-based TPR, two sets of triple coincidence TPR spectrometers, which are based on a thin (2 mm thick) YAP scintillator and a thick (2.54 cm thick) YAP scintillator, respectively, have been developed and tested on the ChipIr beam line and ROTAX beam line. The thin triple coincidence TPR was designed by adding one more coincidence and has been tested on the ChipIr beam line. The thick triple coincidence TPR was designed to check the affect of a beam collimator so it has been tested on the ROTAX beam line where the neutrons are well collimated.

1. Prototype test of the thin triple coincidence TPR on ChipIr

The thin YAP scintillator-based triple coincidence TPR prototype consists of two Silicon detectors and a thin YAP scintillator ($\phi 2.54 \times 0.2$ cm), as shown in figure 4.20. A YAP pulser has been placed on the surface of the PMT to monitor its long term stability. Two silicon detectors have been covered by a layer of thin Al foil ($30 \mu m$ thick) on each side. The thinner silicon detector ($340 \mu m$ thick) was placed as the first detector for keeping the ability of low energy protons detection by performing the coincidence analysis with the second silicon detector ($451 \mu m$ thick).

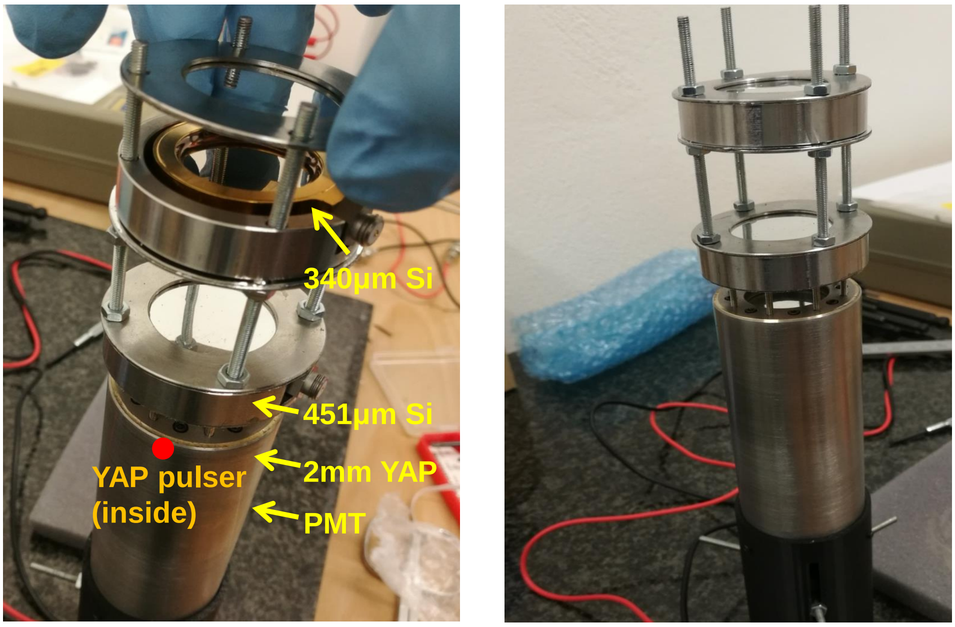

Figure 4.20: Picture of the triple coincidence TPR spectrometer. From top to bottom are a $340\mu m$ thick silicon detector, a $451\mu m$ thick silicon detector and a 2 mm thick YAP scintillator.

Two silicon detectors were equipped with two low-noise current preamplifier (CIVIDEC C2). The high voltage that applied on the thin silicon ($340\mu m$ thick) detector was +100 V and was +170 V on the thick silicon ($451\mu m$ thick) detector. Signals from the PMT and the two preamplifiers were fed directly into a 500 MSamples/s desktop digitizer (CAEN DT5730). Background measurement was performed by removing the PE target at the same conditions compared with the measurement with the PE target. An example of pulses on the three detectors triggered by the same signal from the proton beam is shown in figure 4.21. Here we note that the pulses on the two silicon detectors are clear but the pile-up is still very serious on the 2 mm thick YAP scintillator. As signals on the YAP could be generated either by charged particles (p,d,α, etc.) or scattered neutrons and gamma-rays, it is very hard to separate piled-up pulses by analyzing their pulse shape. Then only the first pulse in each punch beam has been used for PH analysis.

Pulses on the three detectors recorded on the same waveform are considered to be in coincidence if the time difference of their maximum falls inside a selected Δt time window for each two adjacent detectors. As what we did for analyzing the measurements performed with the double coincidence TPR in subsection 4.2.2, the time difference, between the first two silicon detectors and between the second silicon detector and the YAP scintillator, have been obtained, as shown in figure 4.22. Here the first time

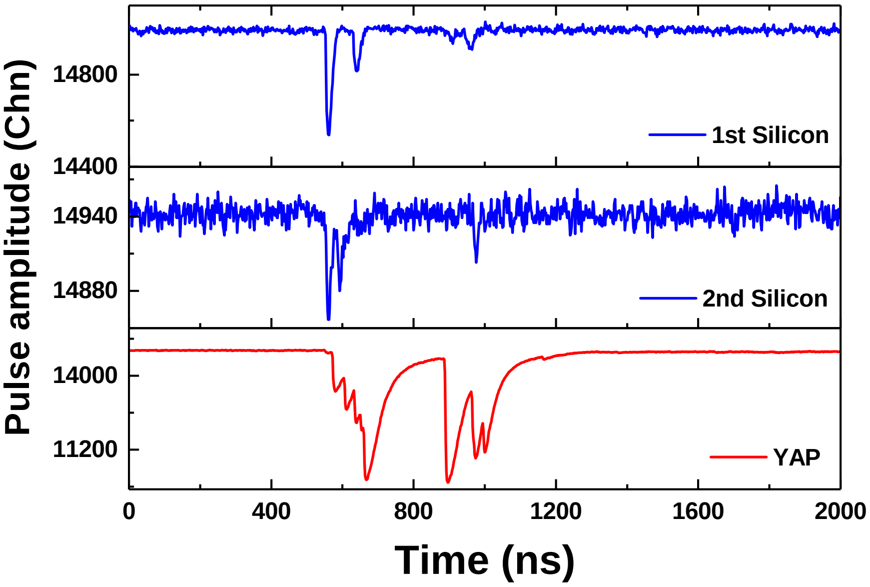

Figure 4.21: An example of pulses on the two Silicon detectors and YAP scintillator.

difference is defined by using the time of pulses on the second silicon detector to minus the time of pulses on the first silicon detector, and the second time difference is defined by using the time of pulses on the YAP detector to minus the time of pulses on the second silicon detector. Here we can note that there is a peak raising up from large random coincident events at about 0 ns for the two silicon detectors. This is because that the used cables length and preamplifiers type for the two silicon detector were the same. As we observed in subsection 4.2.2 for double coincidence analysis, the time difference between the silicon detector and the YAP should be at round 20-80 ns, as the peak shown in figure 4.22 (bottom) at about 30 ns. By comparing the coincident events as a function of Δt between two adjacent detectors in measurements with and without a PE target, the net coincident events distribution was obtained by normalizing events to the proton beam current as shown in figure 4.22. However, no net coincidence peak was raised between the second silicon detector and YAP. The reason could be that, as only the first pulse generated on the YAP scintillator has been considered for PH analysis, the first pulse usually was contributed by the background.

Given by the net coincident events peak raising from the random (or background) coincident events, the first two silicon detectors give the possible of using as a TPR for low energy protons detection, even the true coincident rate was only about 40%. For different energetic incident protons, the energies deposited on the two silicon detectors

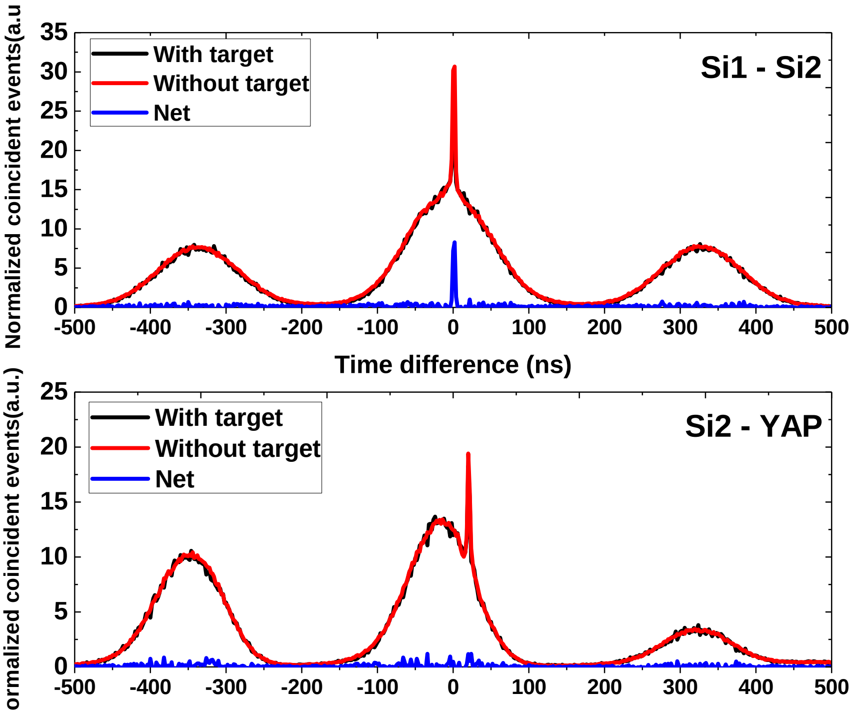

Figure 4.22: Coincidence events as a function of the time difference of pulses on each two adjacent detectors. Upper panel: time difference between the two silicon detectors; Bottom panel: time difference between the second silicon detector and the YAP.

are different. Figure 4.23 (left) shows the relationship of energy deposition on the two silicon detectors with different energetic incident protons. The calculation was performed using the MCNPX code. The probability function of energy deposition by passing through a charged particle in a thin layer of silicon is given by the landau distribution [148], which gives the error bar of each calculation and forms a “banana” shape area of the proton identification map, as shown in figure 4.23 (right). For a mono-energetic incident proton, it deposits more energy on the first silicon detector and less energy on the second silicon detector when its energy just enable it passing through the first Si detector. As the incident energy increases, the deposited energy on the first Si detector decreases but the deposited energy on the second Si detector increase, until the two silicon detectors just full stop the energy of incident protons. For protons carrying energy high enough to pass through the two silicon detectors, they deposit less and less energy on the two detectors as the energy increases.

In measurements, the time difference window for selecting true coincident events between the first two silicon detectors has been determined as 0-2 ns. By analyzing the coincident events within that time window, the experimental 2D map of energy

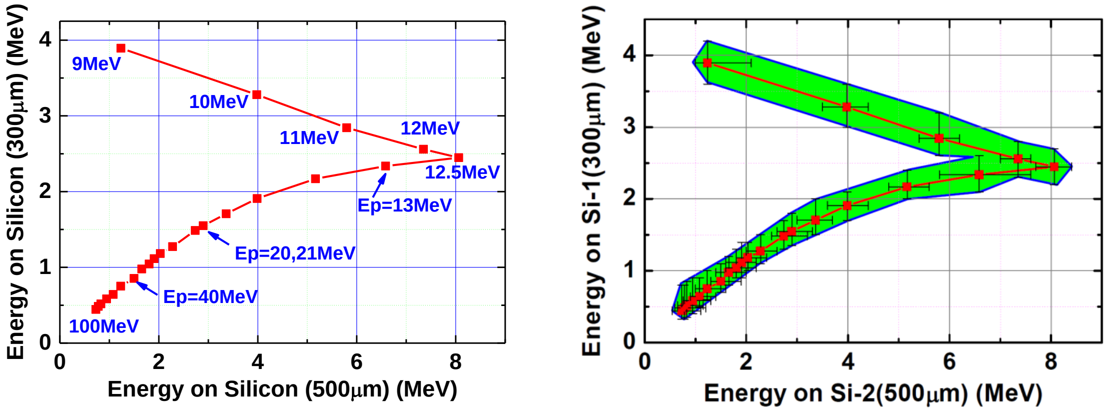

Figure 4.23: 2D identification map of the energy deposition of true coincident events on the two silicon detectors.

deposition of coincident events between the two silicon detectors has been obtained, as shown in figure 4.24. The shape of the distribution, which is similar compared with the calculation results, can be seen but is not very clear. This is because that there were still about more than a half events contributed by random coincidence or background and the measurement was not performed very long.

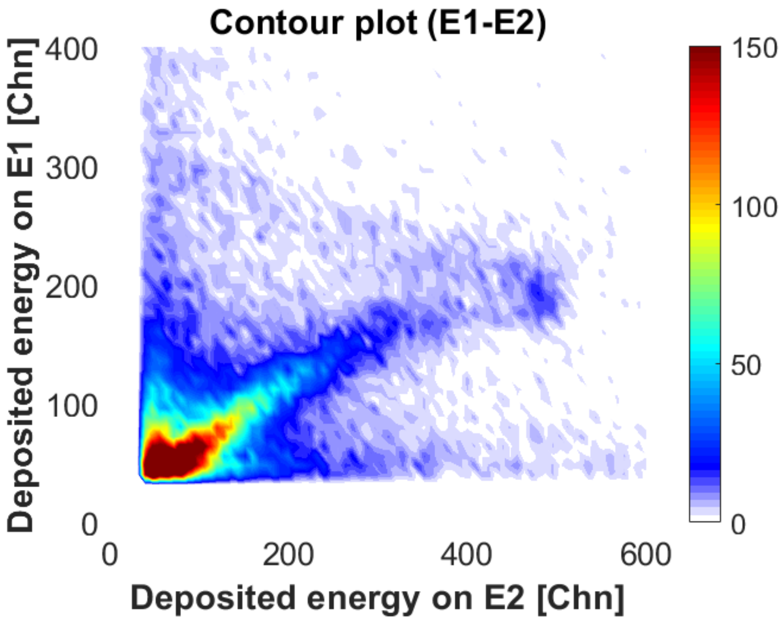

Figure 4.24: The measured 2D energy deposition map of coincident events on the two silicon detectors (300 μm and 500 μm thick).

With the triple coincidence thin TPR prototype based on two silicon detectors and a 2 mm thick YAP scintillator, we demonstrated that the YAP scintillator can not work properly without a dedicated collimator and shielding as the serious pulses pile-up effect. The pile-up rate, which is the ratio of piled-up pulses to the total pulses, has been evaluated for the YAP scintillator as about 60% - 80% on ChipIr beam line. In order to evaluate the affect of the collimator, a triple coincidence TPR prototype based on two silicon detectors and a 2.54 cm thick YAP scintillator has been built and tested on the ROTAX beam line.

2. Prototype test of the thick triple coincidence TPR on ROTAX

The first triple coincidence TPR prototype based on a thin YAP scintillator (2 mm thick) has been technically useful to verify the quality of the construction of the detector, i.e. to verify the correct collection of signal waveforms, together with the assessment of the data analysis workflow required to build the pulse height spectrum and to exploit the coincidence method for background suppression. However, an unexpected pile up fraction exceeding more than a half was observed on the YAP scintillator, suggesting an excessive radiation load by scattered neutrons or gamma-rays. This made the reconstruction of the incoming neutron spectrum not at hand. As the massive, dedicated shielding house that would be required to suppress the background radiation down to an acceptable level cannot be built for permanent installation in the ChipIr experimental hall, the general applicability of the TPR technique for measurements of the fast neutron spectrum by a dedicated experiment with the two silicon detectors and a YAP scintillator TPR spectrometer has been tested at the ALF/ROTAX beam line, where the neutron beam is well collimated. The motivation was in this case to mock up the application of the instrument at ChipIr, but in a mitigated γ-ray background environment.

The TPR spectrometer, which was consisting of a 451 μm thick, a 1022 μm thick silicon and a 2.54 cm thick YAP scintillator with the same active area of 450 mm^2 facing the PE target, was positioned at an angle of 30° and 45° with respect to the incident neutrons, respectively. The distance between the center of the PE target and the first silicon detector was about 27 cm. The experimental arrangements on the ROTAX beam line are shown in figure 4.25 for the two cases.

Each silicon detector was equipped with a low-noise current preamplifier (CIVIDEC C2). The YAP scintillator was coupled with a Hamamatsu R9420-100-10mod PMT. All the signals from the three detectors were fed directly into a 500 MSamples/s desktop digitizer (CAEN DT5730). Pulses on the three detectors were triggered by the proton

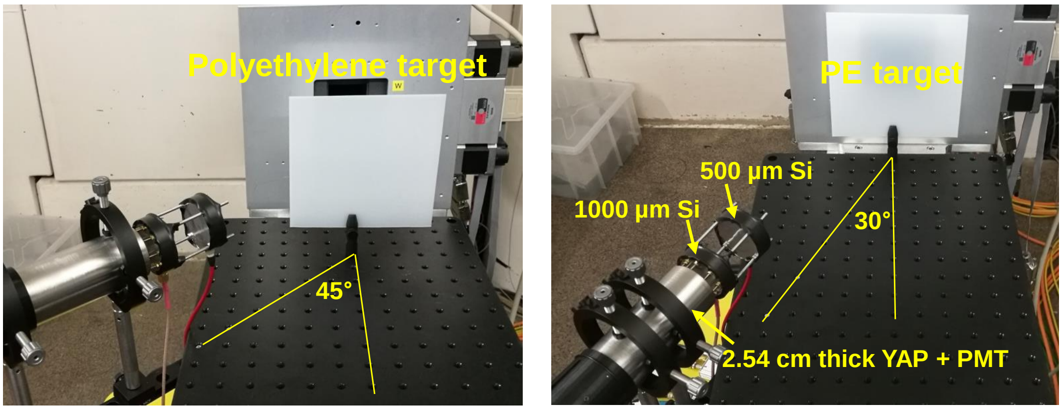

Figure 4.25: The experimental arrangements of the triple coincidence scintillator-based TPR prototype test on the ROTAX beam line.

beam from the synchrotron and were saved to computer after digital process for off-line coincidence analysis, the schematic diagram of electronics flow is shown in figure 4.26.

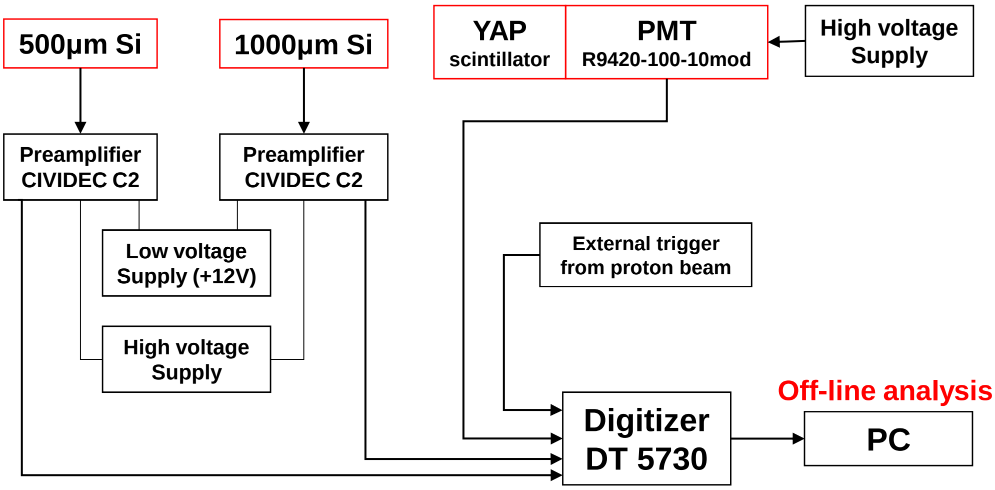

Figure 4.26: The signals process of the triple coincidence TPR spectrometer test on ROTAX.

The two silicon detectors were operated at +170 V and +160 V for the 451 μm and 1022 μm thick silicon, respectively. In order to obtain enough high amplitude signals and at the same time to cover the energy range up to the maximum detectable protons (about 110 MeV for 2.54 cm thick YAP scintillator), -650 V high voltage was applied on the YAP scintillator by also considering the energy calibration that has been presented in subsection 4.2.1.

Figure 4.27 shows an example of pulses on the three detectors. Here we note that the pulses are very clear and pile-up effect is not high on the YAP scintillator.

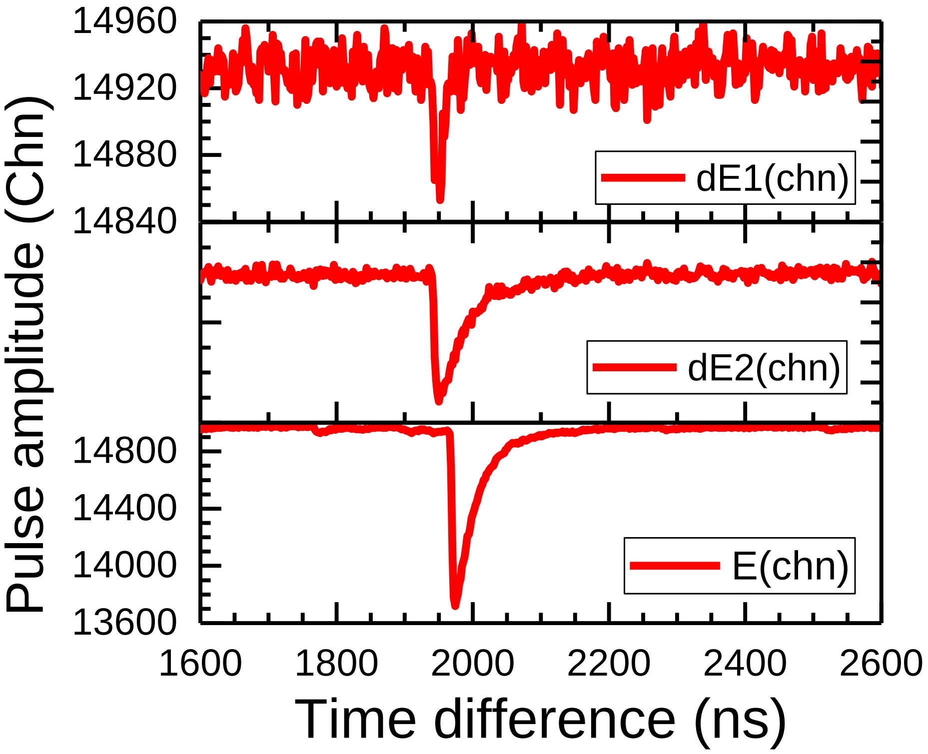

Figure 4.27: An example of measured pulses by the three detectors with the same trigger.

The coincident events as a function of time difference (ΔT) between each two adjacent detectors have been analyzed. Figure 4.28 shows an example of coincident events as a function of ΔT between the first two silicon detectors (left figure) and between the second silicon detector and the YAP scintillator (right figure), respectively, in a measurement with the PE target. We can note that a clear peak raised up on the random coincident events. The true coincident rate has been evaluated higher than 90% in this case. The true coincidence time window was determined as 3 ns with a width of 4 ns for the coincidence analysis between the first two silicon detectors and as 24 ns with a width of 4 ns for the coincidence analysis between the second silicon detector and the YAP scintillator.

By analyzing the coincident events on each true coincident time window, the 2D map of PH on the two adjacent detectors has been obtained to specify different types of particles. The three detectors based TPR could be divided into two TPR, respectively, consisting of the first two silicon detectors and the three detectors. Figure 4.29 shows the contour plot of the PH produced by coincident events between the first two silicon detectors. For comparison of the improvement with coincidence analysis, the contour

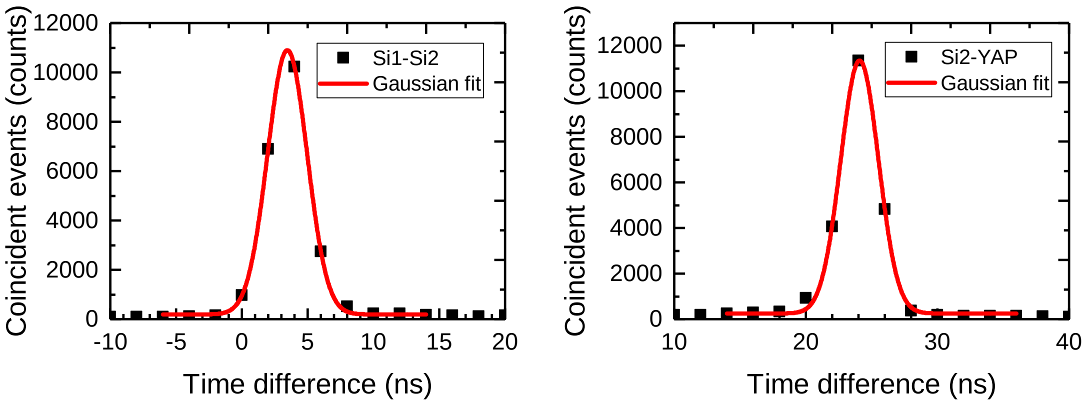

Figure 4.28: An example of measured coincident events as a function of time difference between the first two silicon detectors ($\Delta E1 - \Delta E2$, left) and between the second silicon detector and the YAP scintillator ($\Delta E2 - E$, right).

plots without coincidence analysis (left figure) and with coincident analysis are shown together. Here we note that with the coincidence analysis, the quality of particles presenting and discrimination gets much better. Besides, the intense curve, which is ascribed to protons knocked on by neutrons in the polyethylene target, is unambiguously observed. We also note that two faint, secondary curves appear in the upper half of the plot. This comes from the production of heavier charged particles in the target by neutron induced nuclear reactions. Albeit weak, the clear identification of the secondary curves demonstrate the efficiency of the coincidence window method for background suppression made possible by our instrument design.

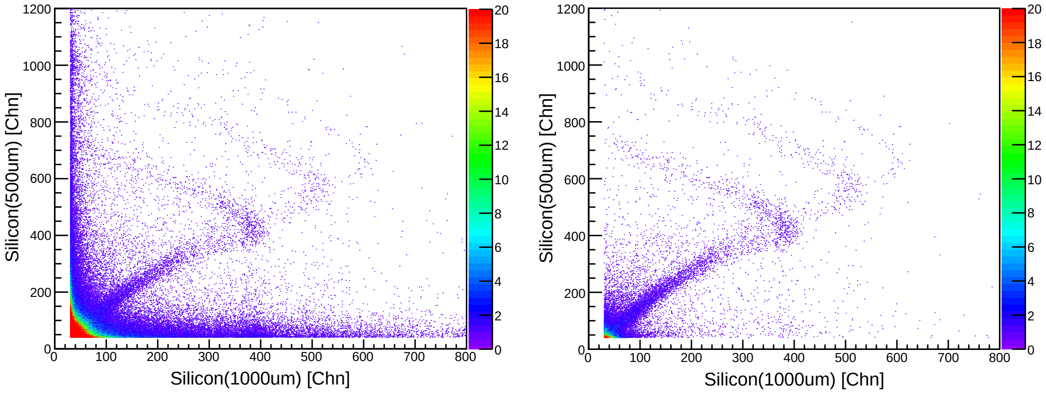

Figure 4.29: An example of measured 2D energy deposition map of coincident events between the first two silicon detectors. Left: without coincidence analysis; Right: with coincidence analysis.

By performing the triple coincidence analysis, the low energy part on the E1-E2 contour plot disappeared because all proton passed through the first two silicon detectors, as shown in figure 4.30. In this case, different type of particles are more easier to be separated from the contour plot between the second detector and the YAP scintillator by using the TCutG tool in ROOT.

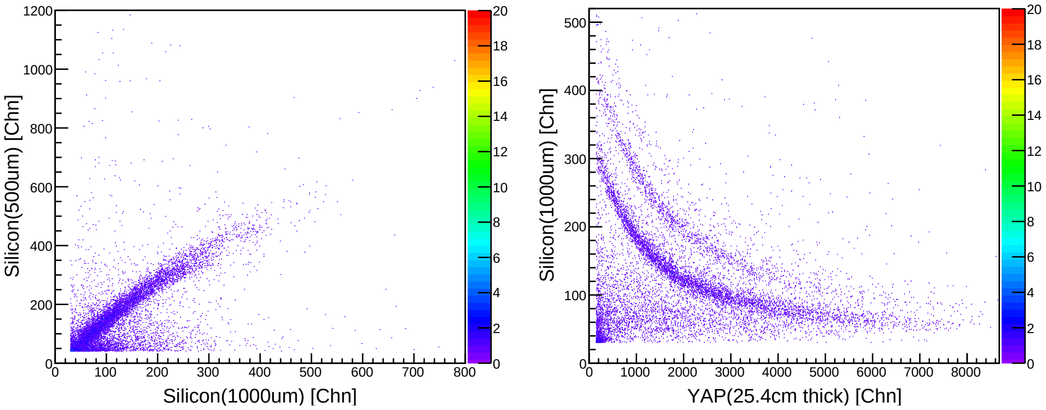

Figure 4.30: An example of measured 2D energy deposition map of coincident events between each two adjacent detectors by performing triple coincidence analysis. Left: coincidence between the first two silicon detectors ($\Delta E1 - \Delta E2$); Right: coincidence between the second silicon detector and the YAP scintillator ($\Delta E2 - E$).

In order to convert the PH to deposited proton energy on each detector, the energy calibration of the 1022 μm thick silicon detector has been performed by using the punch through points resulted by protons, deuterons and tritons. Figure 4.31 shows the relation between the deposited energy and PH on the 1022 μm thick silicon detector and its linear fit. A linear relation between PH and the proton energy on the YAP scintillator $E_p = 0.01547 \times PH - 0.4407$, as determined by the calibration that presented in subsection 4.2.1, has been used to obtain the deposited proton energy.

As there were some Al foils between each two adjacent detectors for protecting each detector from light and electromagnetic noise, the response of each detector to produced protons from the PE target must be calculated. To this end, a MCNPX model based on the experimental setup has been built and simulated by considering the energy loss in air and Al foils. The calculated response matrix is shown in figure 4.32.

With the coincidence analysis in simulation, the energy deposition contour plots between each two adjacent detectors could be reconstructed. By comparing the simulation and measurement, the recoil proton energy spectrum has been obtained, as shown in figure 4.33. As only the fully stopped events have been selected for the $\Delta E - E$ TPR, an energy gap shows on the spectrum. Measurements with and without the PE target

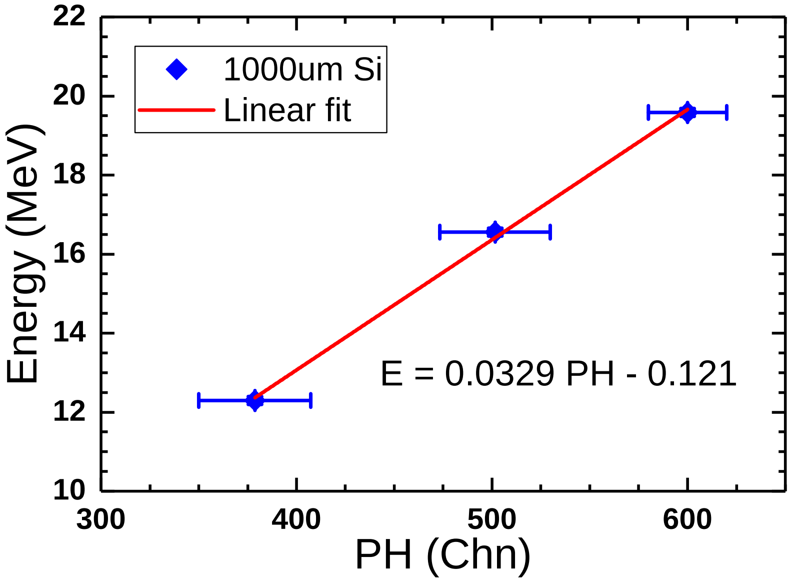

Figure 4.31: Energy calibration of the 1022 μm thick silicon detector by using the punch through points resulted by protons, deuterons, and tritons.

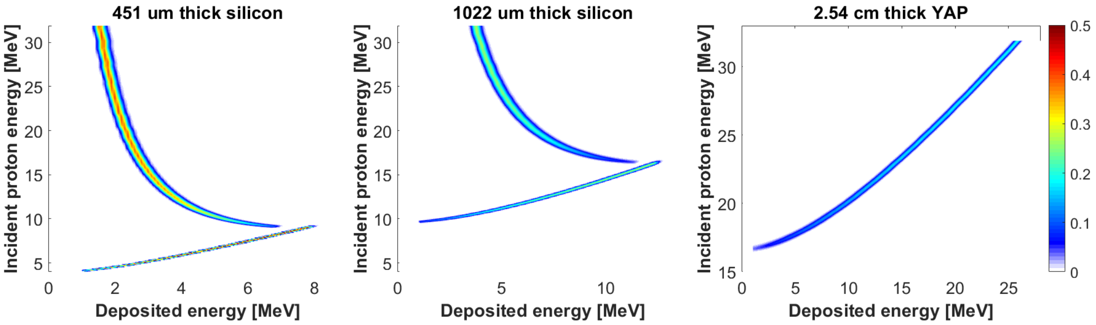

Figure 4.32: Response matrix of the three detectors to protons.

have been normalized to the proton beam and compared to obtain the net recoil proton energy spectrum.

The analysis of the energies contained in the curve is a measurement of the proton energy spectrum, which can be related to the energy distribution of the neutrons in the beam by the known geometrical setup of the experiment. When all the detectors have been calibrated, the neutron energy spectrum can be obtained. Here we have demonstrated that the application of the scintillator-based TPR spectrometers for fast neutron spectrum measurement is feasible in a mitigated γ-ray background environment. However, as the problem of intense background existing on the ChipIr beam line, the scintillator-based TPR, which is very sensitive to neutrons and gamma-rays, cannot be applied so far as the pulses pile-up on the scintillator. In this case, low sensitive volume

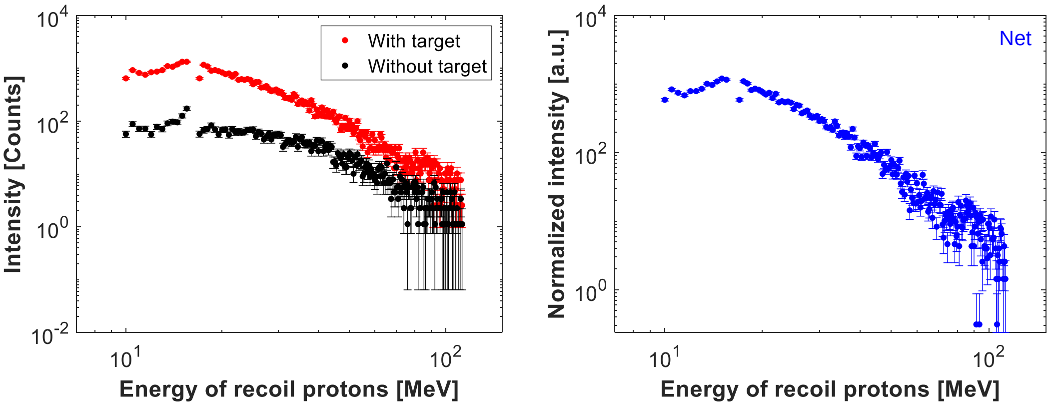

Figure 4.33: Measured recoil proton energy spectrum after considering the background (without PE target).

and multi-coincidence TPR is demanded.

4.3 Silicon-based TPR spectrometer

In order to overcome the limitations encountered in the scintillator-based TPR prototype as introduced in section 4.2, a TPR spectrometer consisting of only silicon detectors has been designed by replacing the YAP scintillator. The concept is expected to mitigate the interference of γ-ray background on the data for two reasons. First, the active volume of each silicon detector is significantly less than that of the 0.2 cm or 2.54 cm thick YAP scintillatrs, which implies a reduced average counting rate (and hence pile up probability) for each detector. This part has been proved as feasible by the tests we performed on the ChipIr and ROTAX beam lines with a triple coincidence scintillator-based TPR prototype. Secondly, more discrimination windows are made possible by the use of multiple detectors, which helps at discriminating coincident neutrons against non-coincident γ-ray events. The construction of the new instrument and a first test of the concept at the ALF/ROTAX beam line are introduced in this section.

4.3.1 Configuration and experimental setup

The silicon-based TPR prototype consists of four surface barrier type silicon detectors with gold and aluminum (Al) contacts. The active area of them were the same with a value of 450 mm^2. The sensitive thicknesses of the four silicon detectors were 219 μm (E1), 340 μm (E2), 451 μm (E3), and 1022 μm (E4), respectively. Each silicon detector, except the third one as the assembly problem, was placed in an Al cylindrical container (as shown in figure 4.34 (right)). The third silicon detector was put in a plastic cylindrical container. All the four silicon detectors were covered by a layer of 15 μm thick Al foil on two sides to shield from light and electromagnetic noise. They were assembled from the thinnest one to the thickest one with the thinnest one facing the incident protons and to the center of the target, as shown in figure 4.34. In order to perform the pulse shape analysis (PSA) on the first silicon detector, the rear side of the first detector (219 μm thick) was placed to face the incident protons.

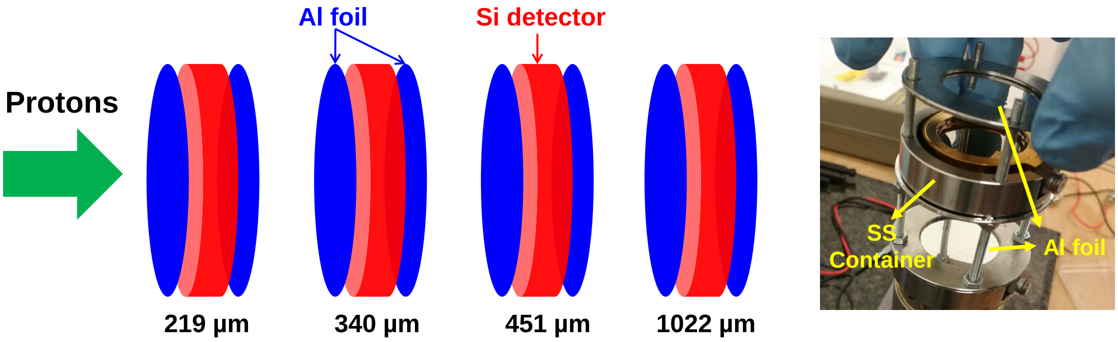

Figure 4.34: Schematic arrangement of the silicon-based TPR prototype and its assembly.

A 2 mm thick polyethylene (PE) layer has been used as a scatter (target) to convert incident neutrons to protons. The TPR spectrometer was placed at 45° with respect to incident neutrons and was aligned to the center of the PE target. The distance between the first silicon detector and the center of the PE target was about 23 cm. Figure 4.35 shows the setup on the ROTAX beam line.

Each silicon detector was connected to a low-noise current preamplifier (CIVIDEC C2). Four silicon detectors, from the thinnest one to the thickest one (E1 to E4), were reverse biased at +70 V, +100 V, +170 V and +160 V, respectively. All signals were fed directly into a 500 MSamples/s digitizer (CAEN DT5730) and were saved by triggering the signals from the synchrotron proton beam. In order to measure the background, the PE target was removed for a long-term measurement.

4.3.2 Pulse processing and coincidence analysis

The waveforms were processed off-line for coincidence and pulse height analysis. Waveforms were acquired at the same time on the four silicon detectors by triggering the signals from the synchrotron proton beam. The length of each waveform was 2030

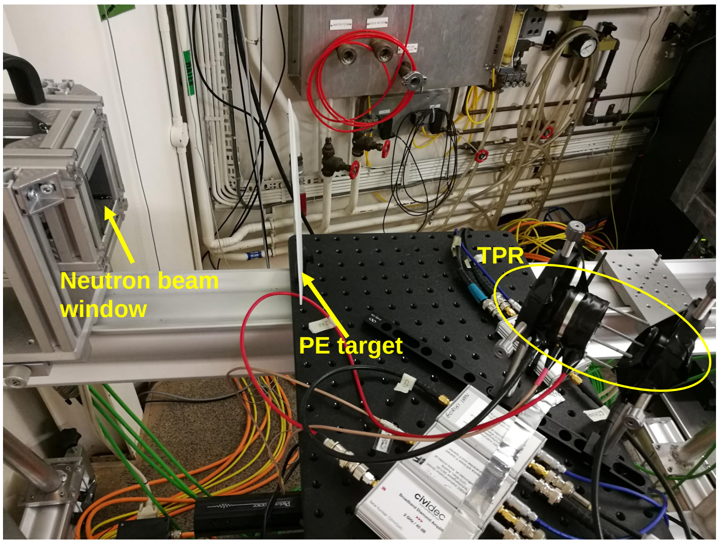

Figure 4.35: Picture of the layout of the silicon-based TPR spectrometer measurement on the ROTAX beam line, indicating the neutron beam window, PE target and the TPR spectrometer with yellow highlights.

points which corresponds to 4060 ns. As the neutron spectrum on the ROTAX beam line was continuous up to a few hundred MeV, high energetic recoil protons from the PE target could pass through the four silicon detectors and the Al foils on the two sides of each detector. However, on the other hand, low energy recoil protons could be stopped in the first three detectors or even on the first detector. Consequently, the four silicon detectors could be divided into 3 TPR spectrometers based on the detectable energy range. For simplification, here we named the TPR spectrometer consisting with the first two detectors as “D1-D2”, the first three silicon detectors-based TPR spectrometer “D1-D2-D3”, and the four detectors-based TPR spectrometer “D1-D2-D3-D4”, respectively. The data files were first read at the same time to check if there was a signal on each detector, and then the data were analyzed and were classified to each group (TPR). Figure 4.36 shows the flow chart of the analysis.

In order to check if there was a signal on a detector, a self-defined threshold should be set properly, and the baseline of each waveform must be evaluated first. The first 400 ns samples of the waveform were used to estimate the baseline by calculating their average value. The maximum absolute value and the variance of the output digitized current signal (higher or lower than the base line, i.e. the electronic noise level) during the first 400 ns samples were obtained. For each TPR spectrometer, the waveform of each silicon detector has been analyzed to calculate the number of peaks (signals) and their corresponding parameters, e.g. raise time, pulse height (PH), area and the position

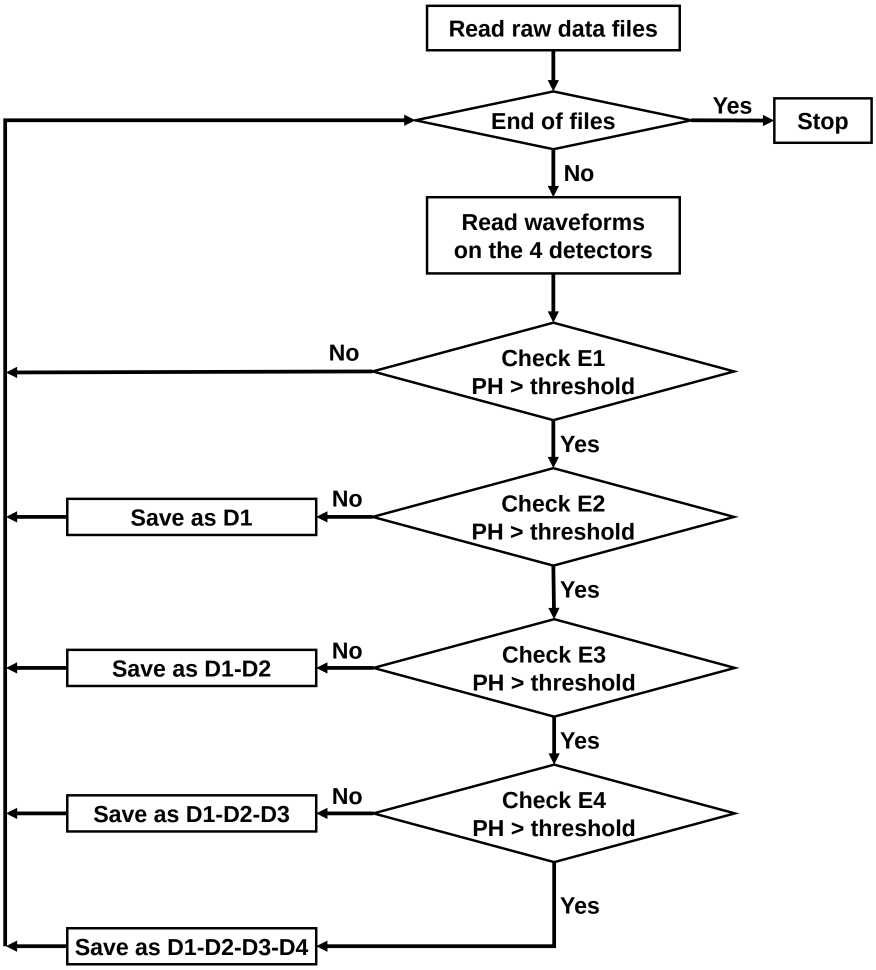

Figure 4.36: The flow chat diagram of the off-line analysis.

of maximum PH of each pulse. All the analysis was based on the ROOT framework [149] and the results were save into an individual tree for each TPR spectrometer. Figure 4.37 shows an example of pulses on the 4 silicon detectors by choosing the same time window. In order to obtain the above mentioned parameters for each pulse, some procedures have been performed: interpolation of the waveform, find the number of peaks, and calculate their area, PH and raise time.

In order to get the maximum PH and the raise time of each peak, each waveform has been curve fitted by applying a cubic interpolation algorithm (third degree polynomial equation). The number of interpolated points between two adjacent ADC samples (2 ns spaced) has been studied. A calibration of the 1022 μm thick silicon detector with a ^{241}Am α source has been performed and been analyzed with and without interpolation. Figure 4.38 (left) shows the PH spectrum without interpolation and with 50 points

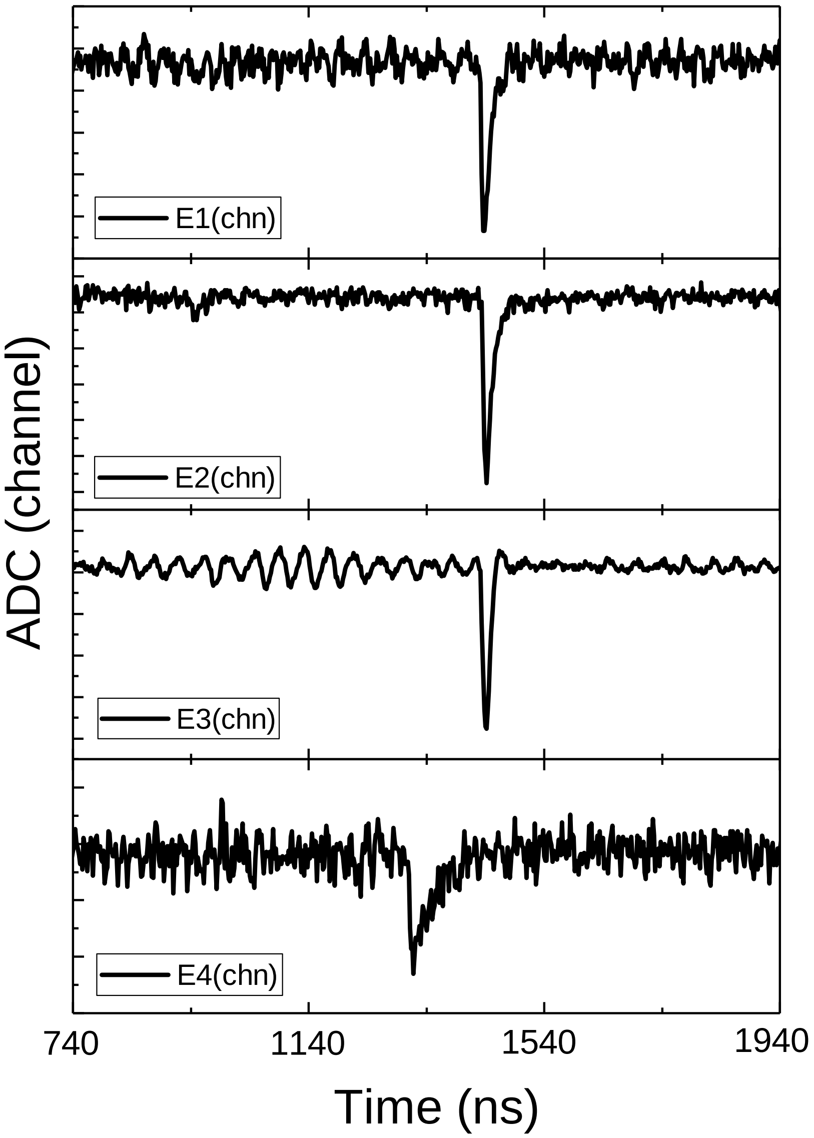

Figure 4.37: An example of generated pulses on the four silicon detectors at the same time window.

interpolation analysis. As the limits of the energy resolution of the detector in air, the 3 α peaks (5388 keV: 1.6%; 5422 keV: 13%; 5485 keV: 84.5%) structure is not clear. Each PH peak has been fitted by applying a gaussian function to obtain the center of the peak. We found that the interpolation analysis improves the PH determination when the number of interpolated points increases, reaching a non-improvement situation for more than 10 points. In order to improve the PH analysis enough and to make the analysis time not too long, 10 points interpolation analysis has been used to analyze the TPR data, which yields a new interpolated sampling rate of 5 GSamples/s.

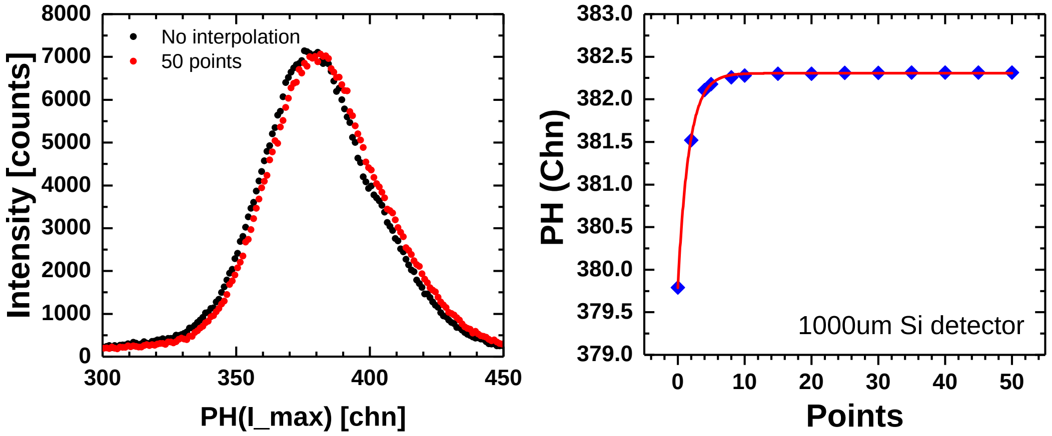

Figure 4.38: Calibration of the 1022 μm thick silicon detector and its PH determination using interpolation method. Left: PH spectrum without and with interpolation; Right: Determined PH as a function of interpolated points in waveform analyzing.

For each pulse, the start point and the stop point have been obtained by setting a 10% PH threshold, as shown in figure 4.39. The PH was obtained by calculating the difference between the minimum amplitude of the interpolated samples and the baseline. The time of the pulse that will be used for later coincidence analysis was the position of the PH. In case of the PSD analysis by using the area and raise time of each pulse, the raise time was obtained by using the time difference between the start point and the PH point. The area of each pulse was obtained by summing up the products of interpolation bin and the amplitude of each interpolated point from the start point to stop point. The parameters of each pulse (raise time, PH, area, pulse time, etc.) have been save into the corresponding TPR tree in a root file for coincidence analysis.

The first three silicon detectors were assembled together with the distance between each two adjacent silicon detectors lower than 1.5 cm. The distance between the third and the fourth silicon detector was about 4 cm. If an incident proton punches through a detector and then arrived at the detector just behind the former one, the time difference between two generated pulses on the two adjacent detectors would mainly be the summation of the time difference caused by the preamplifiers, cables and the time of protons flight between the two detectors. The signal cables used for the first three detectors were about 15 m long with 0.5 m difference. The signal cable used for the fourth detector was about 13 meters long. All the four used preamplifiers were the same type so the difference of time consuming in the preamplifiers should be very low. By performing the coincidence analysis as introduced in section 4.2, the coincident events as a function

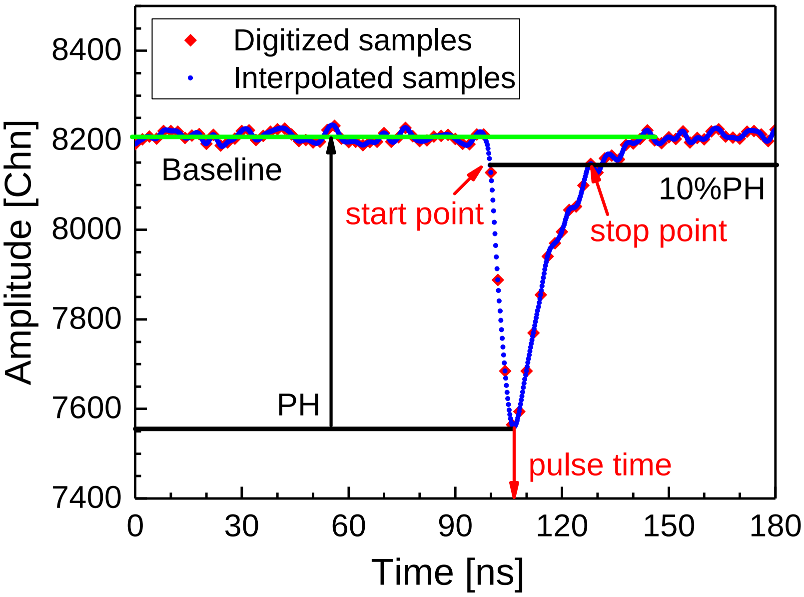

Figure 4.39: Diagram of the pulses analysis.

of time difference between two adjacent silicon detectors has been obtained by using the pulse time on the downstream detector to minus the pulse time on the upstream detector, as shown in figure 4.40. Here we note that the true coincident events raise a very clear peak from random coincident events. The time difference window (ΔT) for selecting true coincident events has been determined as -6 ns $< \Delta T <$ 10 ns between E1-E2, -6 ns $< \Delta T <$ 8 ns between E2-E3 and -34 ns $< \Delta T <$ -24 ns between E3-E4, respectively. As the large electronic noise on the third detector (E3), the random coincidence was high on the coincidence analysis between the E2-E3 and E3-E4. In this situation, the true coincident events still raised clear peaks from random coincident events, and the true coincident rate was determined larger than 70%.

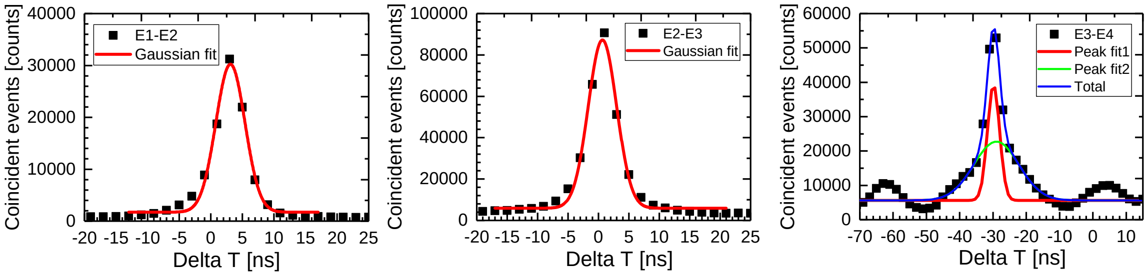

Figure 4.40: Coincident events as a function of time difference between each two adjacent detectors.

With the determined time difference windows for selecting the true coincident events, the PH $\Delta E - E$ contour plots between each two adjacent detectors for the three silicon-based TPR spectrometers have been obtained, as shown in figure 4.41. For the "D1-D2" double coincidence TPR, which corresponds to the case that there was no signal on the third detector, charged particles are separated clearly based on the 2D ID map. Along to proton signature, there are other particles which present similar shape by the different charge and mass: deuterons, tritons, ^{3}He and α particles. The intensity of these signatures is, as expected, less pronounced than protons, as the lower corresponding nuclear reaction cross sections compared to nuclear elastic scattering and the higher stopping power in air and Al foils (on the both sides of each silicon detector). However, the shape of each type of particles contribution presented here is different from the "banana" shape as shown in figure 4.9, which presents a typical double coincidence $\Delta E - E$ contour plot. Besides the low energy protons, which deposit more and more energy on the second detector when they fully deposited their energy on it, some high energy protons are also observed, which carrying high enough energy to pass through both the detectors. The reason why there was no signal on the third detector would be that the high energy particles deposited the rest energy on the two Al layers between the two detectors, or passed through the two Al layers but contributed less energy on the third detector (less than the self-set threshold), or have been scattered by the air or Al between the two detectors. For the "D1-D2-D3" triple coincidence TPR and the "D1-D2-D3-D4" four coincidence TPR, we can also observe the high energy protons which passed through all the detectors. Besides, some few low energy protons (marked with a red dash cycle) have been observed on the E1-E2 coincidence contour plot, which should not be presented here because there was a signal on the third detector which means that the proton has passed through the first two. This might be caused by the case that sometimes the signals we analyzed on the third silicon detector were actually electronic noise as we didn't set a high threshold on each detector, thus there was practically no triple coincidence in this case and the incident particles practically deposited the whole energy on the first two detectors. This part proton events between E1-E2 have been added to the "D1-D2" double coincident events.

For each TPR spectrometer, e.g. the "D1-D2-D3-D4" TPR, the coincident events that fully deposited their energy on the last two silicon detectors can be selected by using the TCutG cut tool in ROOT, as shown in figure 4.42 for selecting protons, deuterons and tritons. As the three particles were overlapped around punch through points and could not be separated so far by using PSA, the applied cut area for each type of particles

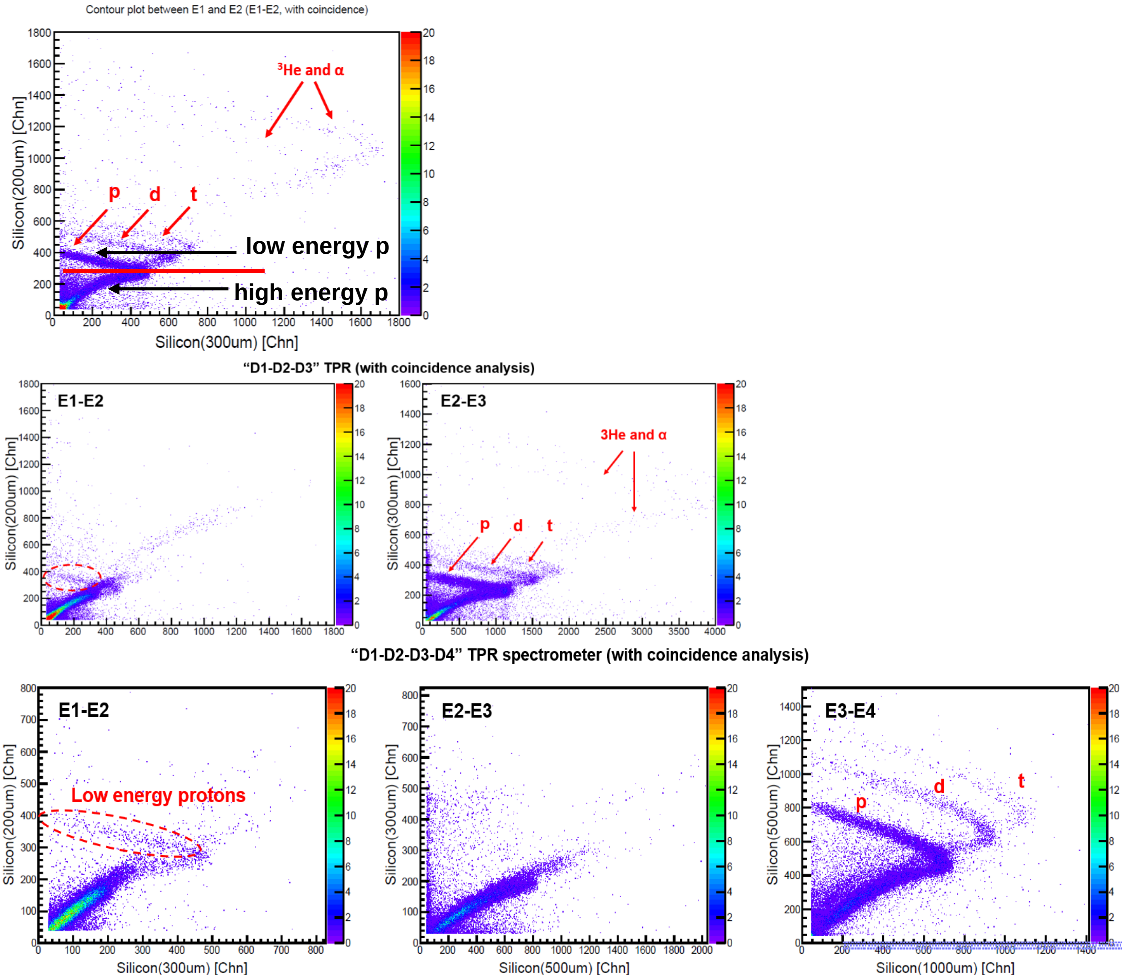

Figure 4.41: $\Delta E - E$ contour plots between each two adjacent detectors for the three silicon-based TPR prototypes. Top panel: "D1-D2" double coincidence TPR; Middle: "D1-D2-D3" triple coincidence TPR; Bottom: "D1-D2-D3-D4" four coincidence TPR.

only focuses on the low energy region. In this case, we lost some events in near punch through region but improved (ensured) the accuracy.

By performing the particles selection for protons on the contour plot of E3-E4 for the "D1-D2-D3-D4" TPR as shown in figure 4.42, the four coincident events for protons can be selected. Figure 4.43 shows the contour plot of the PH of four coincident events on the each two adjacent detectors. Some random coincident events have been observed as the events on the contour plots of E1-E2 and E2-E3 are not on the "curve" which is determined by the Bethe formula. Consequently, similar cuts have been applied on the contour plots of E1-E2 and E2-E3, as shown in figure 4.43. With the three set "cuts" for "D1-D2-D3-D4" TPR, those four coincident events, which passed through the first three silicon detectors and deposited the full energy on the fourth detector, have been

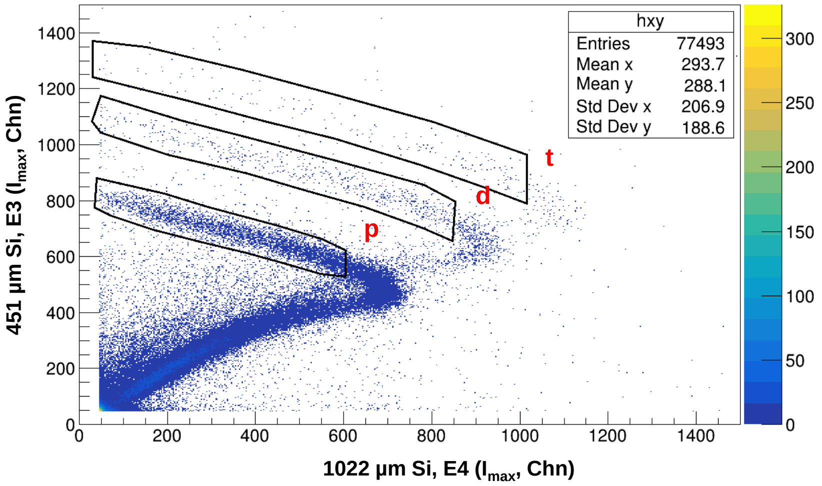

Figure 4.42: Particles selection for events that deposited the full energy on the fourth silicon detector for the "D1-D2-D3-D4" TPR.

selected. By repeating the same procedure for the "D1-D2" and "D1-D2-D3" TPRs, the corresponding coincident events have been selected, respectively.

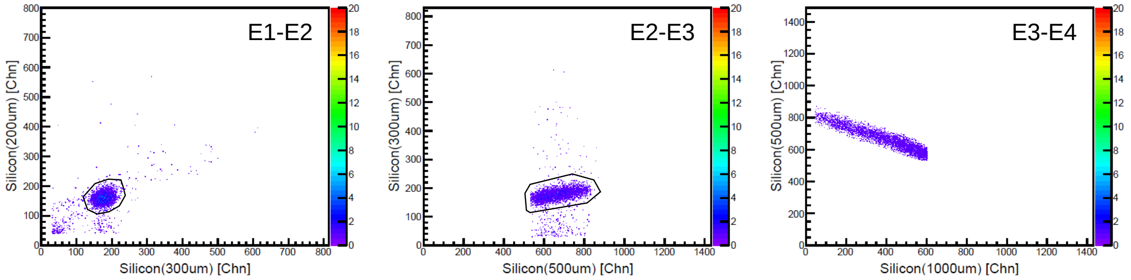

Figure 4.43: $\Delta E - E$ contour plot between each two adjacent detectors for the "D1-D2-D3-D4" TPR after performing coincident events selection.

4.3.3 Energy calibration

In a typical $\Delta E - E$ telescope spectrometer for charged particles detection, charged particles have passed through the ΔE detector so the energy deposition on the ΔE detector always decreases as the energy of incident particles increases. On the contrary, for particles passed through the ΔE detector and deposited the residual energy on the E detector, the deposition energy on the E detector always increases as the incident energy increases, until to an energy point after which the particles can pass through the two detectors (ΔE and E), then the deposition energy on the E detector decreases as the incident energy increase. The energy point that enable particles just pass through the two detectors is called the punch through point and that can be used for energy calibration.

In the four silicon detectors-based TPR spectrometer, we can obtain two proton punch through points for the second and the third detectors based on the contour plots of E1-E2, E2-E3 and E2-E3, E3-E4, respectively. For the first detector, one proton punch through point could be first obtained from contour plot of E1-E2. The other proton punch through point that just enable protons passing through the first detector could be obtained by analyzing the events that the energy has been fully deposited in the first detector, i.e. there is no pulse on the second detector. In this case, the PSA method is needed to discriminate different types of charged particles. Moreover, by analyzing the coincidence between E2-E3 and E3-E4, more calibration points could be obtained for the first silicon detector.

The proton punch through point (PTP) for each silicon detector has been calculated using the MCNPX code by employing with the la150.h library. A continuum energy proton spectrum with the same intensity from 1 MeV to 15 MeV has been modeled as the particle generator to calculate the deposition energy spectrum on each silicon detector. The maximum energy that protons can deposit on each detector is the PTP, as shown in figure 4.44. The proton punch through point for each silicon detector has then been obtained from figure 4.44. For comparing with the MCNPX calculations, another independent way by using the projected range from the SRIM code has been performed. The two calculated results have been compared as shown in table 4.4.

Table 4.4: Comparison of calculated proton punch through energy in silicon detectors using MCNPX and SRIM

	Calculated proton punch through energy (MeV)	
	MCNPX	SRIM
219 μm	5.2	5.05
340 μm	6.6	6.53
451 μm	7.7	7.69
1022 μm	12.2	12.33

In order to convert the PH channel to proton deposition energy, the response of the full four silicon detectors-based TPR to protons should be obtained. To this end, a MCNPX model by considering air, Al foils between each two adjacent silicon detectors, the sensitive thickness of detectors and the accurate distance between each two detectors has been built and simulated by employing the la150.h library. Figure 4.45 shows the

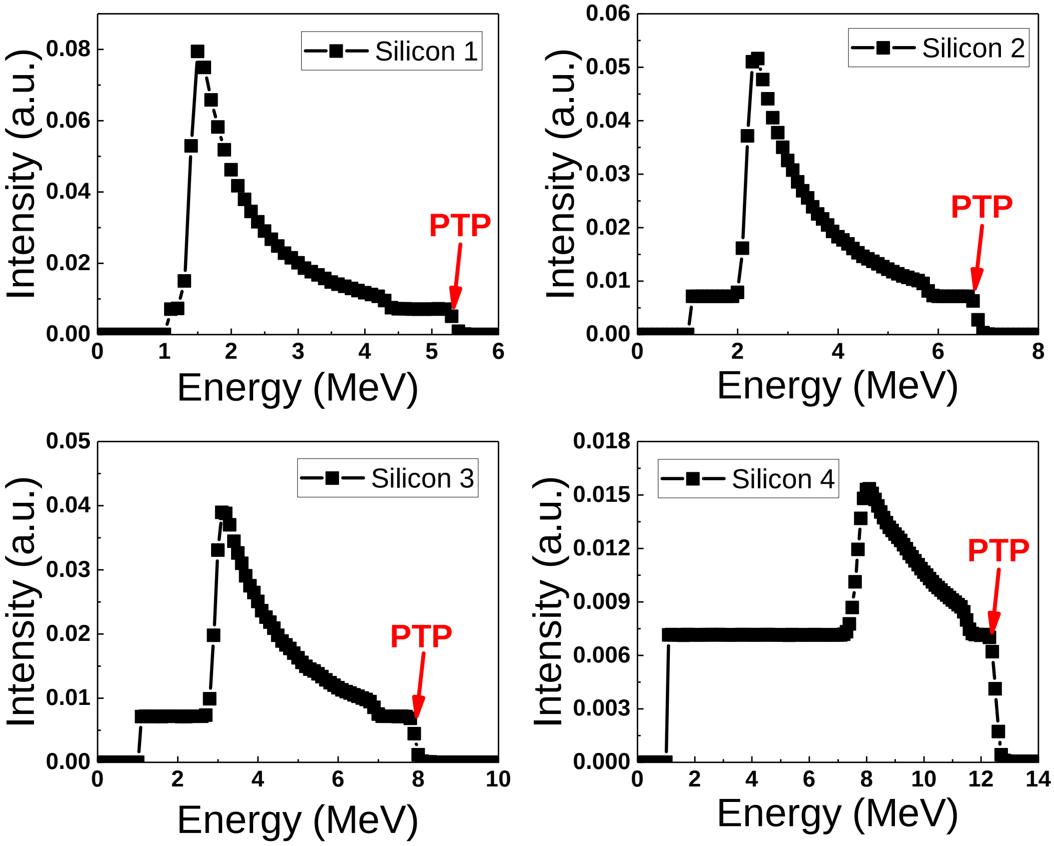

Figure 4.44: Calculated energy deposition on each silicon detector with continuum energetic protons incident on.

calculated response matrix of each silicon detector to protons. For each mono-energetic proton (y axis), the energy deposition on each silicon detector is shown (axis). The probability of a proton depositing energy on each detector is shown as the intensity (from white to red) which is normalized to one source proton.

In the MCNPX model, each run event has generated 1×10^7 protons with the same energy. Run events with incident proton energy from 4.5 MeV to 40 MeV with a step of 0.1 MeV have been performed. Therefore, on one hand, the energy calibration points for the first three silicon detectors could be obtained based on the calculated response function, on the other hand, the coincidence events between each two adjacent detectors could be reconstructed to compare with measurements. Figure 4.46 shows the reconstructed contour plots between each two silicon detectors based on the MCNPX simulation.

With the analysis of relation between area and PH of each pulse, as shown in figure 4.15, we confirmed that the PH of each pulse is proportional to its area, and linear

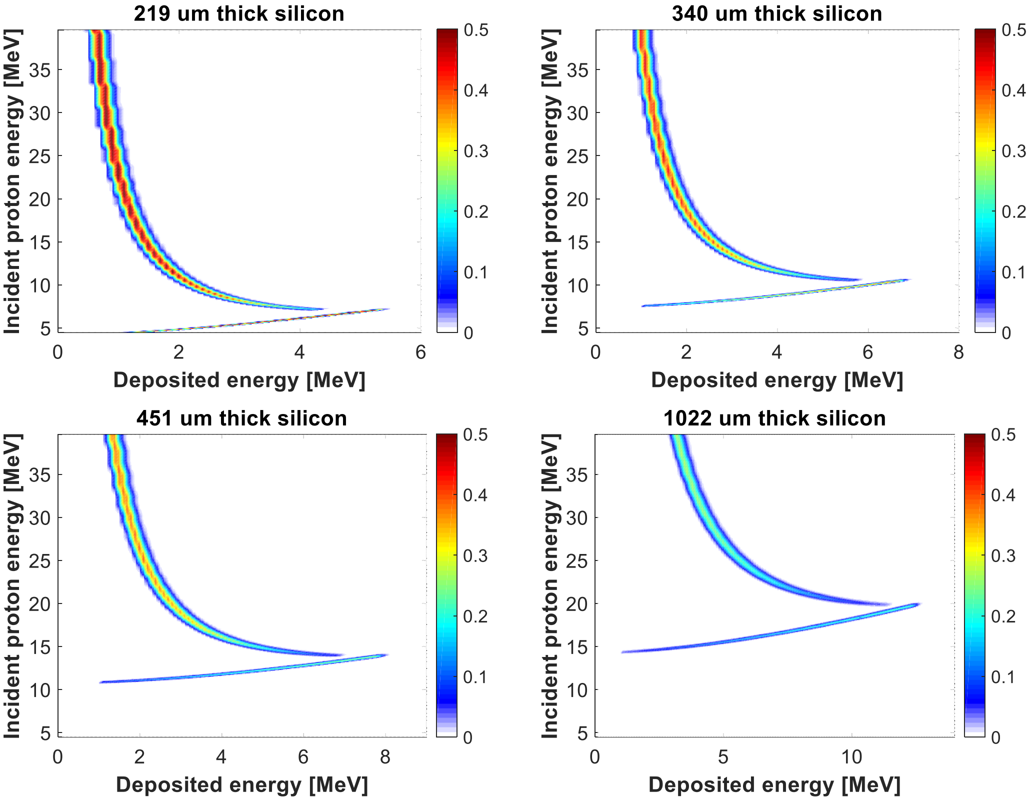

Figure 4.45: Response function of each silicon detector to protons.

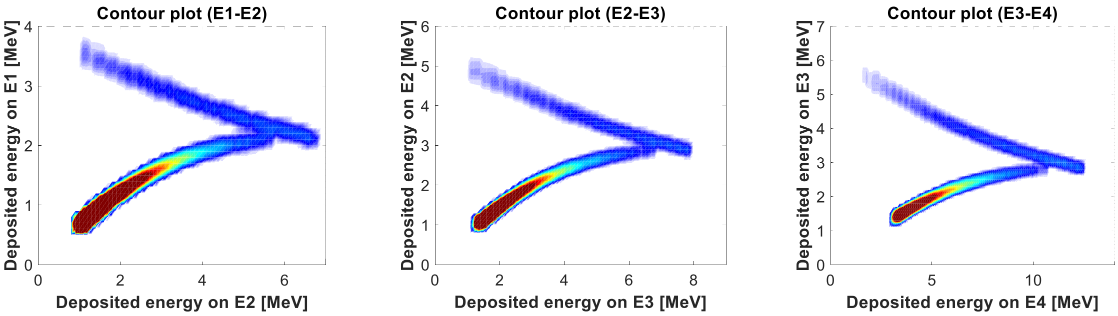

Figure 4.46: Reconstructed contour plots between each two silicon detectors based on the MCNPX simulation.

relations for protons, deuterons and tritons are overlapped, i.e. the relations between energy deposition and PH are the same for protons, deuterons and tritons. Therefore, the punch through points resulted by deuterons and tritons on each detector could also be used for energy calibration. By analyzing the measured PH of each punch through points, the energy calibration for each silicon detector has been obtained by comparing the corresponding calculated deposition energy on each silicon detector. Figure 4.47 shows the relation between calculated deposition energy resulted by different types of charged particles and the measured PH. A linear fit has been applied for each detector and the fitting formula is also presented in each figure.

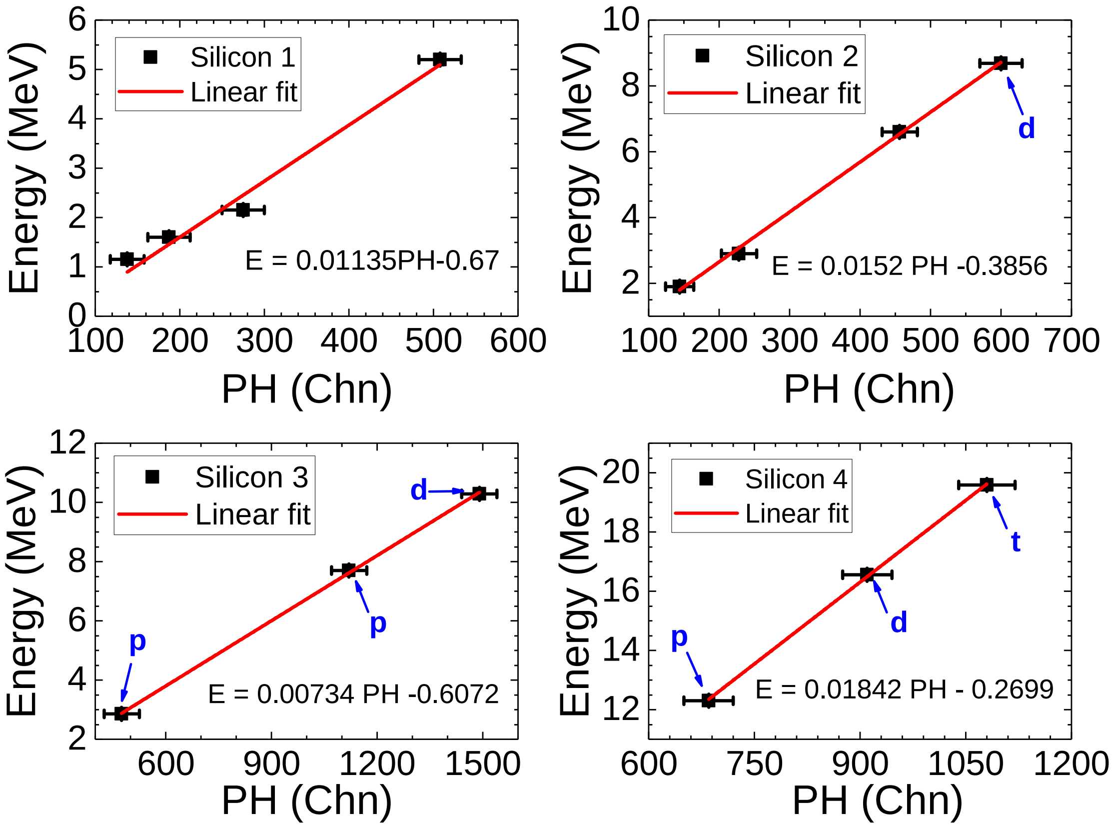

Figure 4.47: Relations between energy deposition and the measured pulse height for the four silicon detectors.

4.3.4 Measured recoil proton spectrum

For each TPR ("D1-D2", "D1-D2-D3" or "D1-D2-D3-D4") spectrometer, the coincident events could be picked up by using the TCutG tool in ROOT. As the example shown in figure 4.43 for the "D1-D2-D3-D4" TPR, the coincident events have been first selected on the E3-E4 contour plot. With the energy calibration curve for the fourth silicon detector as shown in figure 4.47, all the events have been marked with an energy information. From the calculated response function for the fourth silicon detector as shown in figure 4.45, we note that the response of each detector to incident proton is on a narrow curve when the protons are fully stopped in the detector. By fitting the curve, the deposited energy that converted from PH with the energy calibration could be used to calculated the incident proton energy. Figure 4.48 shows the measured recoil proton spectra using the three silicon-based TPR spectrometers by placing a PE scatter and removing the target.

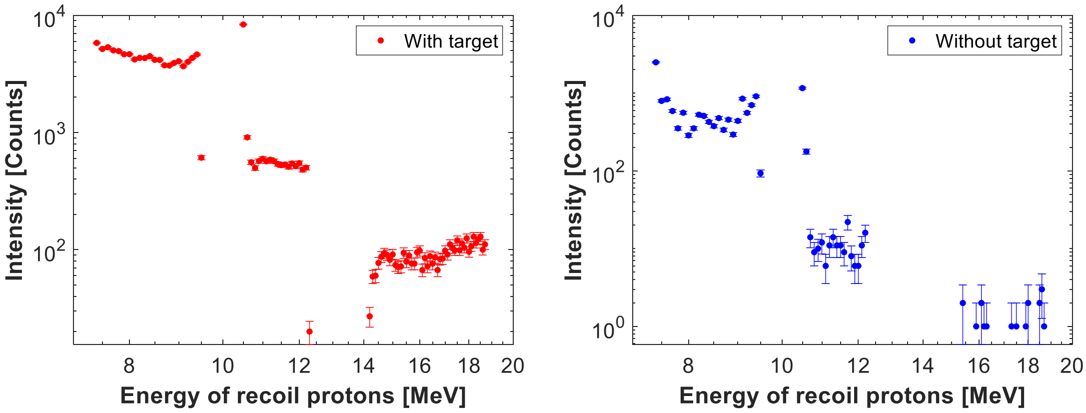

Figure 4.48: Measured recoil proton spectrum using the three silicon-based TPRs with a PE scatter (left) and without a PE scatter (right).

As all the four detectors were not assembled so close that the distance between each two could be ignored compared with the distance between the target and detectors, thus, the flux of incident protons on each detector has to be corrected. In this case, the distance between each two silicon detectors and the detector-target distance have been used by considering the reverse relation of square distance to correct the relative flux on the third silicon for the "D1-D2-D3" TPR and on the fourth detector for the "D1-D2-D3-D4" TPR.

In order to obtain the net coincident events and the corresponding recoil spectrum, the measured data, with and without the PE target, has been normalized to proton beam current (μA) from the synchrotron and the experimental duration (h). At the end, the energy spectrum of the recoil protons that be scattered on the PE target has been obtained, as shown in figure 4.49.

4.4 Prospects for neutron spectrum measurements on ChipIr

In order to measure the fast neutron spectrum on the ChipIr beam line, which is dedicated for electronics radiation studies, some TPR prototypes have been designed and tested trying to obtain the neutron spectrum for benchmarking MC based simulations and as an experimental input for SEE study. No matter the tests were using a

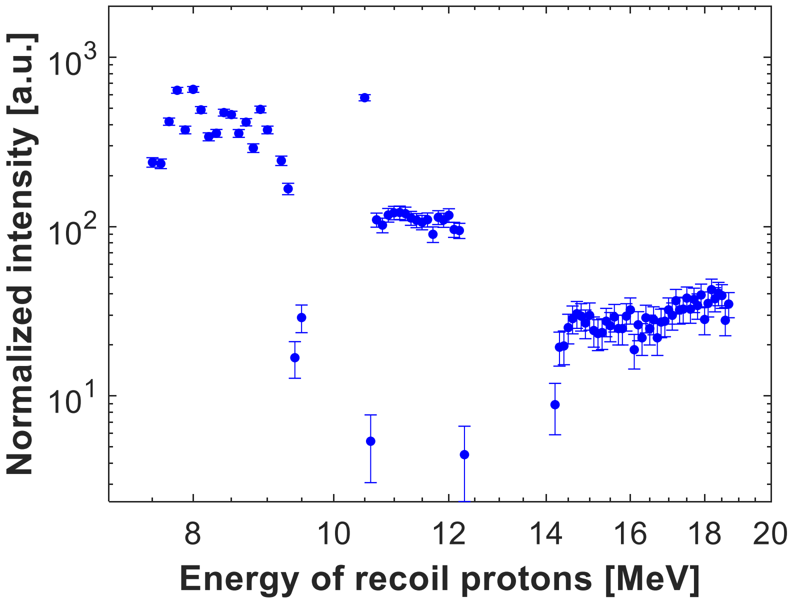

Figure 4.49: The recoil proton energy distribution of the coincident events.

double coincidence or a triple coincidence scintillator-based TPR, the pulses pile-up was too much on the used YAP scintillator, which has a relative fast response time (around 20-40 ns). The pile-up rejection cannot be significantly improved by adding more coincidence analysis. This made the reconstruction of the incoming neutron spectrum not at hand. As the massive, dedicated shielding house that would be required to suppress the background radiation down to an acceptable level cannot be built for permanent installation in the ChipIr experimental hall, thus, a new TPR design by considering the intense background on the ChipIr beam line is needed.

With the full silicon detectors based TPR prototype, the recoil proton spectrum on the ROTAX beam line has been well measured. Even the neutron beam is well collimated on the ROTAX beam line and the background contributed by scatter neutrons and gamma-rays are much lower than that on the ChipIr beam line, the experience has still been technically useful to verify the quality of the construction of the detector, i.e. to verify the correct collection of signal waveforms, to perform the energy calibration, together with the assessment of the data analysis workflow required to build the pulse height spectrum and to exploit the coincidence method for background suppression. The same design silicon-based TPR with well mounted components will be tested on the ChipIr beam line.

Chapter 5

Conclusions and outlook

Who talks of victory?
To endure is all.
“Wer spricht von Siegen? Überstehn ist alles.”
– Rainer Maria Rilke

5.1 Conclusions

This thesis presents results on fast neutron measurements applied to nuclear fusion and spallation sources, in particular, to deuterium beam diagnostics with neutrons and to fast neutron beam line characterization on a spallation neutron source. The novelty of the research activity was the development of instruments and methods for fast neutron detection with the capability to deal with complex background and for a fundamental understanding of the process of deuterium implantation and beam-target neutron emission. These results can be summarized following the two parts of the thesis: Liquid scintillator for DD reaction neutrons detection and the Telescope Proton Recoil spectrometers.

Concerning the application of a scintillator for deuterium beam diagnostics by measuring the beam-target neutron emission from the $D(d,n)^3He$ reactions, the neutron/gamma-rays discrimination has been first performed with a low energy threshold of about 1.4 MeV neutrons to avoid the scattering neutrons on neutron intensity determination. In order to predict the neutron emission, the local mixing model has been applied to describe the deuterium implantation on the dump and to calculate the time trace of neutron yield. LMM based calculation has relatively been compared with the measurement. The ratio between calculations and measurements (C/E) on a relative scale has been found to exceed unity beyond the observed fluctuation level of the data points at constant power and to scale linearly with the beam power in the range 200 kW - 950 kW. By assuming difference can be explained by a temperature dependent saturation rate of deuterons in the target, an empirical correction to neutron emission calculations for applications at SPIDER has been derived.

Concerning the application of TPR spectrometers for fast neutron spectrum measurement, two types of TPR prototypes, consisting of only silicon detectors and consisting of silicon detectors and a YAP scintillator, respectively, have been designed and tested trying to obtain the neutron spectrum for benchmarking MC based simulations and as an experimental input for SEE study. However, an unexpected pile up fraction exceeding more than a half was observed on the YAP scintillator of the scintillator-based TPR, suggesting an excessive radiation load by scattered neutrons or gamma-rays. As the pile-up rejection cannot be significantly improved by adding more coincidence analysis. This made the reconstruction of the incoming neutron spectrum not at hand. On the other hand, the two silicon coincidence analysis on the triple coincidence scintillator-based TPR was first found feasible for recoil protons detection as their relative low sensitive volume, especially non-sensitive to gamma-rays, which is the main background on the ChipIr beam line. Then a TPR spectrometer consisting of only silicon detectors has been designed by replacing the YAP scintillator. The concept is expected to mitigate the interference of γ-ray background on the data for two reasons. First, the active volume of each silicon detector is significantly less than that of the 0.2 cm or 2.54 cm thick YAP scintillatrs, which implies a reduced average counting rate (and hence pile up probability) for each detector. This part has been proved as feasible by the tests we performed on the ChipIr and ROTAX beam lines with a triple coincidence scintillator-based TPR prototype. Secondly, more discrimination windows are made possible by the use of multiple detectors, which helps at discriminating coincident neutrons against non-coincident γ-ray events. The four coincidence silicon-based TPR has been well used to measure the recoil protons in energy range 8 - 19 MeV. Even the neutron beam is well collimated on the ROTAX beam line and the background contributed by scatter neutrons and gamma-rays are much lower than that on the ChipIr beam line, the experience has still been technically useful to verify the quality of the construction of the detector, i.e. to verify the correct collection of signal waveforms, to perform the energy calibration, together with the assessment of the data analysis workflow required to build the pulse height spectrum and to exploit the coincidence method for background suppression.

5.2 Outlook

Based on these results, a similar scintillator as a monitor will be installed at the SPIDER facility for detecting neutrons from the beam-target reactions. The empirical correction for local mixing model on describing the deuterium implantation on the dump at high beam power circumstance, which was derived based on the so far data collected from the ELISE facility, will also be applied on the SPIDER for aiding the development of the CNESM neutron imaging system.

As the massive, dedicated shielding house that would be required to suppress the background radiation down to an acceptable level cannot be built for permanent installation in the ChipIr experimental hall, a TPR system with low sensitive volume detectors is needed. With the success test of the four silicon detectors-based TPR on recoil proton measurement on the ROTAX beam line, a similar design of silicon-based TPR with well mounted components will be tested on the ChipIr beam line.

Acknowledgements

Very quietly I take my leave,
As quietly as I came here.
Gently I flick my sleeves,
Not even a wisp of cloud will I bring away.
– Hsu Chih-mo

I have to admit that I am not adept in memorizing. But when I look at the backward path in my last three years' life in Italy, a lot of gorgeous moments just like movies waving in my head. On the endless and brief process, I not only gained knowledge and skills, but also reaped friendships, a more wide world view, the marriage, an adorable daughter, and more than 10 pounds weight. When I landed in Milano on 15th November, 2015, I learned my first Italian word "uscita" (not ciao!) from Massimo on his car when he picked me up. Now, I am standing at the "uscita" of my doctoral journey, I really thank those people who I met for their supporting, helping and advising.

First of all, I would like to express my sincere thanks to my two tutors: Dr. Marco Tardocchi and prof. Giuseppe Gorini. Thank them for their trust and advising in finishing this project. In the IFP's lab, Marco taught me experimental skills in electronics. His passion on what he is doing and his diligence spirited me up. Thank him for his good taking care of me when we were in Abingdon for missions on ISIS and JET. My wife likes my cooked "carbonara" just because I learned the authentic recipe from him there. Special thank should be given to Giuseppe, who I first met when he visited EAST, Hefei in May of 2015. Really thank him for his personal financial support, for his help on dealing with the bureaucracy documents with different Italian agencies, and for his support on providing a place for us when my wife visited me in 2016. With his funding support I obtained a lot of opportunities to attend many educational schools and conferences, and to perform experimental activities in many international laboratories.

Dr. Massimo Nocente, who has helped me from (even before) the beginning of my

PhD study and acted the role of my supervisor, deserves the foremost thank in this journey. We have stayed in the same office for three years, and I learned very much from the excellent office mate: code programming, plasma physics, the way of solving problems by using physics, etc. I would say without his help I might have not finished my thesis by now. We traveled together a lot for experiments or analysis tasks: INFN-LNS (Catania), ISIS, JET, EPFL...Thank him for sharing classic music with me. I was also enriched from many discussions with him on education, political affairs, Italian culture and so on (no gossip?). I felt less lonely with him when my family was not here.

Then I would like to acknowledge our nice and kind group members: Giorgia Albani, Nicola Bonanomi, Carlo Cazzaniga, Gabriele Croci, Andrea Dal Molin, Daniela Di Martino, Luca Giacomelli, Giovanni Grosso, Zhimeng Hu, Triestino Minniti (Tino), Jamalipour Mostafa, Andrea Muraro, Enrico Perelli Cippo, Roberto Pinna, Marica Rebai, Davide Rigamonti and Giuseppe Vitucci. It's really enjoyable for me to work with them. Thank them all for their help on this project or on the life in Milano! In particular, Carlo, has helped me on the TPR development, shared his experience on detectors and electronics, provided valuable comments on writing papers and this thesis, and Marica, has provided a lot of help on preparing experiments, and Tino, has helped me on using ROOT for data analysis. I would like to thank Gabriele and Luca for their help on simulating the response of diamond detectors to neutrons, even this part of work has not been included in this thesis, I learned a lot from this experience. Thank Davide for his encouragement on writing this thesis and for his help on moving house. We traveled together for summer schools and tasks and had lots of fun.

In our group I sincerely thank our two administrators: Giovanni Posadinu and Roberta Cattaneo. They helped me a lot on dealing with reimbursements and other stuff besides science. In department of physics at university of Milano-Bicocca there are two special places where people can find perfect American coffee and refreshing tea, respectively, in Roman H. Eduardo and Roberto Benocci's offices. Thank them for offering chances that we could discuss so much interesting things. Besides, thank Eduardo for his help on finding an apartment for my family, and Roberto, for his fresh fruits in every season. I really enjoy the time with you!

Frankly speaking, it's really helpless for me to live alone in a place where I couldn't speak the local language. I really thank those Chinese friends who I met in Italy, especially: Hongsheng Liu, Wendong Liang, Jiaju Zhang, Weike Wang, Yiping Zeng, Guolong Xing, et al. We had a lot of fun together. I would also like to thank those

Italian friends who I made and helped me: Costanza Ronchi, Massimiliano Natasi, Davide Chiesa, Adriano Galimberti, et al. Especially Costanza, who has helped me a lot on applying for many documents from some agencies in Monza. Thank those people who welcomed and helped me when I traveled to Abingdon in the UK: Antonio, Matteo, Stefano, Laura, et al. Thank the administrator Luca for his taking care of me when I lived at U22. It's really a surprise to me that he called my name when I visited U22 after 6 months that I left there.

I certainly must acknowledge the Italian public agencies which I have dealt with for their bureaucracy and extremely low working efficiency. I don't know how much time that I have spent for applying different types of documents. But I am pretty sure that, with the 3-year training I have faith to survive in any other countries in the world.

In the period of staying in Italy, I also received many supports from China. I would like to thank Yiwei Yang, who has provided me financial support and useful comments on finding a position after graduation, and Xufei Xie, who gave me a lot of suggestions and remarks at the beginning of my PhD carrier. Thank prof. Rong Liu and prof. Tieshuan Fan for their recommendations and efforts on finding an academic position for me in China.

Last but definitely not least, I would like to express my deepest gratitude towards my family: my parents, my parents-in-low, my sister and her husband, my wife Juan and daughter Hanru. Thank them for their endless love and support to me. I would not have made it to this point without them. In particular, my wife Juan, the girl I knew when I was 12, supported my decision for the PhD and has always standing behind me. I apologize that I couldn't spend too much time with you during the past three years, especially the last two months when I was writing this thesis.

There is a proverb in China saying that: "Do not travel far away from home where your parents live at, unless there is a way (to take care of them)", my sister and her husband have been the way when I was outside of our home. However, there were still many regrets to me because I was not there when my daughter at birth and when my grandfather passed away. I really want to say sorry to my grandfather, who was a very kind person, for having no time to stay with him in his last time. Life is never easy, care what you love while it lasts.

To life!

30/10/2018
Milan

Bibliography

[1] James Chadwick. Possible existence of a neutron. *Nature*, 129(3252):312, 1932.

[2] Glenn F Knoll. *Radiation detection and measurement.* John Wiley & Sons, 2010.

[3] Igor Pioro. *Handbook of generation IV nuclear reactors.* Woodhead Publishing, 2016.

[4] FL Ribe. Fusion reactor systems. *Reviews of Modern Physics*, 47(1):7, 1975.

[5] Carlo Rubbia, C Roche, Juan Antonio Rubio, F Carminati, Y Kadi, P Mandrillon, Jean Pierre Charles Revol, S Buono, Robert Klapisch, N Fiétier, et al. Conceptual design of a fast neutron operated high power energy amplifier. Technical report, 1995.

[6] Alexander Stanculescu. Accelerator driven systems (adss) for nuclear transmutation. *Annals of Nuclear Energy*, 62:607–612, 2013.

[7] Tatiana Angelescu, AE Cheremukhin, VM Ghete, N Ghiordănescu, IA Golutvin, S Lazanu, I Lazanu, A Mihul, A Radu, N Yu Susova, et al. Radiation hardness studies on silicon detectors in fast neutron fields. *Nuclear Instruments and Methods in Physics Research Section A: Accelerators, Spectrometers, Detectors and Associated Equipment*, 357(1):55–63, 1995.

[8] LJ Peters, MH Maor, GE Laramore, TW Griffin, and FR Hendrickson. Review of clinical results of fast neutron therapy in the usa. *Nucl. Sci. Appl*, 2(3):243–260, 1986.

[9] André Wambersie, Françoise Richard, and Noël Breteau. Development of fast neutron therapy worldwide: Radiobiological, clinical and technical aspects. *Acta oncologica*, 33(3):261–274, 1994.

[10] Richard Hoppe, Theodore L Phillips, and Mack Roach. *Leibel and Phillips Textbook of Radiation Oncology.* Elsevier Health Sciences, 2010.

[11] BD Sowerby and JR Tickner. Recent advances in fast neutron radiography for cargo inspection. *Nuclear Instruments and Methods in Physics Research Section A: Accelerators, Spectrometers, Detectors and Associated Equipment*, 580(1):799–802, 2007.

[12] TA Wellington, BA Palles, JA Mullens, JT Mihalczo, DE Archer, T Thompson, CL Britton, ND Bull Ezell, MN Ericson, E Farquhar, et al. Recent fast neutron imaging measurements with the fieldable nuclear materials identification system1. *Physics Procedia*, 66:432–438, 2015.

[13] Peter Marleau. Fast neutron detection and imaging. `http://lux.physics.ucdavis.edu/nssc_summerschool/lib/exe/fetch.php?media=peter_marleau.pdf`. Accessed 22 October 2018.

[14] EN Avrorin and AN Chebeskov. Fast reactors and nuclear nonproliferation problem. *Nuclear Energy and Technology*, 1(1):1–7, 2015.

[15] Donald James Hughes and Robert B Schwartz. Neutron cross sections. Technical report, Nuclear Cross Sections Advisory Group, AEC; Brookhaven Neutron Cross Section Compilation Group, 1958.

[16] C Patrignani, Particle Data Group, et al. Review of particle physics. *Chinese physics C*, 40(10):100001, 2016.

[17] John Lindl, Otto Landen, John Edwards, Ed Moses, and NIC team. Review of the national ignition campaign 2009-2012. *Physics of Plasmas*, 21(2):020501, 2014.

[18] Jet Team et al. Fusion energy production from a deuterium-tritium plasma in the jet tokamak. *Nuclear Fusion*, 32(2):187, 1992.

[19] J Ongena, R Koch, R Wolf, and H Zohm. Magnetic-confinement fusion. *Nature Physics*, 12(5):398, 2016.

[20] J Li, HY Guo, BN Wan, XZ Gong, YF Liang, GS Xu, KF Gan, JS Hu, HQ Wang, L Wang, et al. A long-pulse high-confinement plasma regime in the experimental advanced superconducting tokamak. *Nature physics*, 9(12):817, 2013.

[21] Baonian Wan, Jiangang Li, Houyang Guo, Yunfeng Liang, Guosheng Xu, et al. Progress of long pulse and h-mode experiments in east. *Nuclear Fusion*, 53(10):104006, 2013.

[22] JE Menard, S Gerhardt, M Bell, J Bialek, A Brooks, John Canik, J Chrzanowski, M Denault, L Dudek, DA Gates, et al. Overview of the physics and engineering design of nstx upgrade. *Nuclear Fusion*, 52(8):083015, 2012.

[23] Albrecht Herrmann and Otto Gruber. Chapter 1: Asdex upgrade-introduction and overview. *Fusion Science and Technology*, 44(3):569–577, 2003.

[24] A Isayama, Y Kamada, N Hayashi, T Suzuki, T Oikawa, T Fujita, T Fukuda, S Ide, H Takenaga, K Ushigusa, et al. Achievement of high fusion triple product, steady-state sustainment and real-time ntm stabilization in high-βp elmy h-mode discharges in jt-60u. *Nuclear Fusion*, 43(10):1272, 2003.

[25] STTT Coda. Overview of recent and current research on the tcv tokamak. *Nuclear Fusion*, 53(EPFL-ARTICLE-191260):104011, 2013.

[26] RC Wolf, Anwaar Ali, A Alonso, Jürgen Baldzuhn, Craig Beidler, M Beurskens, C Biedermann, H-S Bosch, S Bozhenkov, Rudolf Brakel, et al. Major results from the first plasma campaign of the wendelstein 7-x stellarator. *Nuclear Fusion*, 57(10):102020, 2017.

[27] Edward I Moses and Craig R Wuest. The national ignition facility: laser performance and first experiments. *Fusion Science and Technology*, 47(3):314–322, 2005.

[28] R Betti and OA Hurricane. Inertial-confinement fusion with lasers. *Nature Physics*, 12(5):435, 2016.

[29] S Le Pape, LF Berzak Hopkins, L Divol, A Pak, EL Dewald, S Bhandarkar, LR Bennedetti, T Bunn, J Biener, J Crippen, et al. Fusion energy output greater than the kinetic energy of an imploding shell at the national ignition facility. *Physical Review Letters*, 120(24):245003, 2018.

[30] Cornelis Marius Braams and Peter E Stott. *Nuclear fusion: half a century of magnetic confinement fusion research.* CRC Press, 2002.

[31] John Wesson and David J Campbell. *Tokamaks*, volume 149. Oxford University Press, 2011.

[32] John D Lawson. Some criteria for a power producing thermonuclear reactor. *Proceedings of the Physical Society. Section B*, 70(1):6, 1957.

[33] EUROfusion. Scheme of the nbi principle. `https://www.euro-fusion.org/wpcms/wp-content/uploads/2011/07/8c.jpg`. Accessed 29 August 2018.

[34] M Kuriyama, N Akino, T Aoyagi, N Ebisawa, N Isozaki, A Honda, T Inoue, T Itoh, M Kawai, M Kazawa, et al. Operation of the negative-ion based nbi for jt-60u. *Fusion engineering and design*, 39:115–121, 1998.

[35] HPL De Esch, D Stork, C Challis, and B Tubbing. The optimization of neutral beams for ignition and burn control on next-step reactors. *Fusion Engineering and Design*, 26(1-4):589–604, 1995.

[36] T Inoue, R Hemsworth, V Kulygin, and Y Okumura. Iter r&d: Auxiliary systems: Neutral beam heating and current drive system. *Fusion engineering and design*, 2(55):291–301, 2001.

[37] V Toigo, D Boilson, T Bonicelli, R Piovan, M Hanada, A Chakraborty, G Agarici, V Antoni, U Baruah, M Bigi, et al. Progress in the realization of the prima neutral beam test facility. *Nuclear Fusion*, 55(8):083025, 2015.

[38] V Toigo, R Piovan, S Dal Bello, E Gaio, A Luchetta, R Pasqualotto, P Zaccaria, M Bigi, G Chitarin, D Marcuzzi, et al. The prima test facility: Spider and mitica test-beds for iter neutral beam injectors. *New Journal of Physics*, 19(8):085004, 2017.

[39] P Sonato, V Antoni, M Bigi, G Chitarin, A Luchetta, D Marcuzzi, R Pasqualotto, N Pomaro, G Serianni, V Toigo, et al. Status of prima, the test facility for iter neutral beam injectors. In *AIP Conference Proceedings*, volume 1515, pages 549–558. AIP, 2013.

[40] R Pasqualotto, G Serianni, P Sonato, M Agostini, M Brombin, G Croci, M Dalla Palma, M De Muri, E Gazza, G Gorini, et al. Diagnostics of the iter neutral beam test facility. *Review of Scientific Instruments*, 83(2):02B103, 2012.

[41] Roberto Pasqualotto, M Agostini, M Barbisan, M Brombin, R Cavazzana, G Croci, M Dalla Palma, RS Delogu, M De Muri, A Muraro, et al. A suite of diagnostics to validate and optimize the prototype iter neutral beam injector. *Journal of Instrumentation*, 12(10):C10009, 2017.

[42] A Muraro, G Croci, G Albani, C Cazzaniga, G Claps, M Cavenago, G Grosso, M Dalla Palma, M Fincato, F Murtas, et al. Status of the cnesm diagnostic for spider. *Fusion Engineering and Design*, 96:311–314, 2015.

[43] Han S Uhm and WM Lee. High-dose neutron generation from plasma ion implantation. *Journal of applied physics*, 69(12):8056–8063, 1991.

[44] Marica Rebai. *Fast neutron instrumentation for beam diagnostics*. PhD thesis, 2012.

[45] M Rebai, M Cavenago, G Croci, M Dalla Palma, G Gervasini, F Ghezzi, G Grosso, F Murtas, R Pasqualotto, E Perelli Cippo, et al. A neutron diagnostic for high current deuterium beams. *Review of Scientific Instruments*, 83(2):02B721, 2012.

[46] M Rebai, G Croci, G Grosso, A Muraro, E Perelli Cippo, M Tardocchi, M Dalla Palma, R Pasqualotto, M Tollin, F Murtas, et al. Conceptual design of a neutron diagnostic for 2-d deuterium power density map reconstruction in mitica. *Journal of Instrumentation*, 12(01):C01007, 2017.

[47] F Murtas, G Croci, G Claps, M Cavenago, M Dalla Palma, G Gervasini, G Grosso, R Pasqualotto, E Perelli Cippo, M Rebai, et al. A new gem based neutron diagnostic concept for high power deuterium beams. In *Nuclear Science Symposium and Medical Imaging Conference (NSS/MIC), 2011 IEEE*, pages 405–408. IEEE, 2011.

[48] G Croci, M Rebai, G Claps, M Cavenago, M Dalla Palma, G Gervasini, G Grosso, F Murtas, R Pasqualotto, E Perelli Cippo, et al. ngem neutron diagnostic concept for high power deuterium beams. *Journal of Instrumentation*, 7(03):C03010, 2012.

[49] A Muraro, G Croci, G Albani, G Claps, M Cavenago, C Cazzaniga, M Dalla Palma, G Grosso, F Murtas, R Pasqualotto, et al. Performance of the full size ngem detector for the spider experiment. *Nuclear Instruments and Methods in Physics Research Section A: Accelerators, Spectrometers, Detectors and Associated Equipment*, 813:147–152, 2016.

[50] A Muraro. Gem based detectors for fast and thermal neutrons. *PhD thesis*, 2018.

[51] Tatsuhiko Sato, Hiroshi Yasuda, Koji Niita, Akira Endo, and Lembit Sihver. Development of parma: Phits-based analytical radiation model in the atmosphere. *Radiation research*, 170(2):244–259, 2008.

[52] Robert Hart. What is a cosmic ray? `http://cosmicray.com.au/what-is-a-cosmic-ray`. Accessed 30 August 2018.

[53] JAEA. What is expacs? `https://phits.jaea.go.jp/expacs/main-eng.htm`. Accessed 30 August 2018.

[54] A Taber and Eugene Normand. Single event upset in avionics. *IEEE Transactions on Nuclear Science*, 40(2):120–126, 1993.

[55] Bernard W Riemer, Franz X Gallmeier, and Laura J Dominik. Single event effects test facility at oak ridge national laboratory. In *Digital Avionics Systems Conference (DASC), 2015 IEEE/AIAA 34th*, pages 8C6–1. IEEE, 2015.

[56] Eugene Normand. Single-event effects in avionics. *IEEE Transactions on nuclear science*, 43(2):461–474, 1996.

[57] Eugene Normand. Single event upset at ground level. *IEEE transactions on Nuclear Science*, 43(6):2742–2750, 1996.

[58] Edward Petersen. *Single event effects in aerospace.* John Wiley & Sons, 2011.

[59] Robert C Baumann. Radiation-induced soft errors in advanced semiconductor technologies. *IEEE Transactions on Device and materials reliability*, 5(3):305–316, 2005.

[60] Carlo Cazzaniga and Christopher D Frost. Progress of the scientific commissioning of a fast neutron beamline for chip irradiation. In *Journal of Physics: Conference Series*, volume 1021, page 012037. IOP Publishing, 2018.

[61] Christopher D Frost, Stuart Ansell, and Giuseppe Gorini. A new dedicated neutron facility for accelerated see testing at the isis facility. In *Reliability Physics Symposium, 2009 IEEE International*, pages 952–955. IEEE, 2009.

[62] Bernie Riemer and Franz X Gallmeier. Definition of capabilities needed for a single event effects test facility. Technical report, Oak Ridge National Lab.(ORNL), Oak Ridge, TN (United States). Spallation Neutron Source (SNS), 2014.

[63] BE Takala. The ice house-neutron testing leads to more-reliable electronics. *Los Alamos Science*, 30:96, 2006.

[64] Ewart W Blackmore. Development of a large area neutron beam for system testing at triumf. In *Radiation Effects Data Workshop, 2009 IEEE*, pages 157–160. IEEE, 2009.

[65] Alexander V Prokofiev, Jan Blomgren, Mitja Majerle, Ralf Nolte, Stefan Rottger, Simon P Platt, Xiao Xiao Cai, and Andrey N Smirnov. Characterization of the anita neutron source for accelerated see testing at the svedberg laboratory. In *Radiation Effects Data Workshop, 2009 IEEE*, pages 166–173. IEEE, 2009.

[66] Yosuke Iwamoto, Mitsuhiro Fukuda, Yukio Sakamoto, Atsushi Tamii, Kichiji Hatanaka, Keiji Takahisa, Keiichi Nagayama, Hiroaki Asai, Kenji Sugimoto, and Isamu Nashiyama. Evaluation of the white neutron beam spectrum for single-event effects testing at the rcnp cyclotron facility. *Nuclear Technology*, 173(2):210–217, 2011.

[67] Liang Tairan, Li Zhiduo, Yin Wen, Shen Fei, Yu Quanzhi, and Liang Tianjiao. Simulation of a high energy neutron irradiation facility at beamline 11 of the china spallation neutron source. *Nuclear Instruments and Methods in Physics Research Section A: Accelerators, Spectrometers, Detectors and Associated Equipment*, 860:24–28, 2017.

[68] Weijun Ni, Hantao Jing, Liying Zhang, and Li Ou. Possible atmospheric-like neutron beams at csns. *Radiation Physics and Chemistry*, 152:43–48, 2018.

[69] Laura Dominik, Eugene Normand, Michael J Dion, and Phillip Ferguson. Proposal for a new integrated circuit and electronics neutron experiment source at oak ridge national laboratory. *Proceedings of the 2009 IRPS*, 2009.

[70] Antonın Krása. Spallation reaction physics. *Czech Republic: Czech Technical University Lecture*, 2010.

[71] Günter Siegfried Bauer. Physics and technology of spallation neutron sources. *Nuclear Instruments and Methods in Physics Research Section A: Accelerators, Spectrometers, Detectors and Associated Equipment*, 463(3):505–543, 2001.

[72] MNH Comsan. Spallation neutron sources for science and technology. 2011.

[73] Carlo Cazzaniga, Bharat Bhuva, Marta Bagatin, Simone Gerardin, Nicolò Marchese, and Christopher D Frost. Atmospheric-like neutron attenuation during accelerated neutron testing with multiple printed circuit boards. *IEEE Transactions on Nuclear Science*, 2018.

[74] C Andreani, R Senesi, A Paccagnella, M Bagatin, S Gerardin, C Cazzaniga, CD Frost, P Picozza, G Gorini, R Mancini, et al. Fast neutron irradiation tests of flash memories used in space environment at the isis spallation neutron source. *AIP Advances*, 8(2):025013, 2018.

[75] C Andreani, A Pietropaolo, A Salsano, G Gorini, M Tardocchi, A Paccagnella, S Gerardin, CD Frost, S Ansell, and SP Platt. Facility for fast neutron irradiation tests of electronics at the isis spallation neutron source. *Applied Physics Letters*, 92(11):114101, 2008.

[76] MS Gordon, P Goldhagen, KP Rodbell, TH Zabel, HHK Tang, JM Clem, and P Bailey. Measurement of the flux and energy spectrum of cosmic-ray induced neutrons on the ground. *IEEE Transactions on Nuclear Science*, 51(6):3427–3434, 2004.

[77] JEDEC Standard JESD89A. Measurement and reporting of alpha particle and terrestrial cosmic ray-induced soft errors in semiconductor devices. *JEDEC solid state technology association*, 1(6):8, 2006.

[78] International Electrotechnical Commission. Process management for avionics–atmospheric radiation effects–part 2: Guidelines for single event effects testing for avionics systems. *International Standard*, IEC 62396-2:2017, 2017.

[79] International Electrotechnical Commission. Semiconductor devices–mechanical and climatic test methods–part 44: Neutron beam irradiated single event effect (see) test method for semiconductor devices. *International Standard*, IEC 60749-44:2016, 2016.

[80] Davide Chiesa, Massimiliano Nastasi, Carlo Cazzaniga, Marica Rebai, Laura Arcidiacono, Ezio Previtali, Giuseppe Gorini, and Christopher D Frost. Measurement of the neutron flux at spallation sources using multi-foil activation. *Nuclear Instruments and Methods in Physics Research Section A: Accelerators, Spectrometers, Detectors and Associated Equipment*, 2018.

[81] RW Pattie, NB Callahan, C Cude-Woods, ER Adamek, Leah J Broussard, SM Clayton, SA Currie, EB Dees, Xinjian Ding, EM Engel, et al. Measurement of the neutron lifetime using a magneto-gravitational trap and in situ detection. *Science*, 360(6389):627–632, 2018.

[82] P Ouseph. *Introduction to nuclear radiation detectors*, volume 2. Springer Science & Business Media, 1975.

[83] Ej301 scintillator. `https://eljentechnology.com/products/liquid-scintillators/ej-301-ej-309`. Accessed 29 August 2018.

[84] Yap(ce) scintillator. `https://www.advatech-uk.co.uk/yap_ce.html`. Accessed 29 August 2018.

[85] M Moszyński, T Ludziejewski, D Wolski, W Klamra, and LO Norlin. Properties of the yag: Ce scintillator. *Nuclear Instruments and Methods in Physics Research Section A: Accelerators, Spectrometers, Detectors and Associated Equipment*, 345(3):461–467, 1994.

[86] John Betteley Birks. *The Theory and Practice of Scintillation Counting: International Series of Monographs in Electronics and Instrumentation*, volume 27. Elsevier, 2013.

[87] Marvin L Roush, MA Wilson, and William F Hornyak. Pulse shape discrimination. *Nuclear Instruments and Methods*, 31(1):112–124, 1964.

[88] RA Winyard, JE Lutkin, and GW McBeth. Pulse shape discrimination in inorganic and organic scintillators. i. *Nuclear Instruments and Methods*, 95(1):141–153, 1971.

[89] P-A Söderström, Johan Nyberg, and Roland Wolters. Digital pulse-shape discrimination of fast neutrons and γ rays. *Nuclear Instruments and Methods in Physics Research Section A: Accelerators, Spectrometers, Detectors and Associated Equipment*, 594(1):79–89, 2008.

[90] RF Lang, D Masson, J Pienaar, and S Röttger. Improved pulse shape discrimination in ej-301 liquid scintillators. *Nuclear Instruments and Methods in Physics Research Section A: Accelerators, Spectrometers, Detectors and Associated Equipment*, 856:26–31, 2017.

[91] Gioacchino Ranucci. An analytical approach to the evaluation of the pulse shape discrimination properties of scintillators. *Nuclear Instruments and Methods in Physics Research Section A: Accelerators, Spectrometers, Detectors and Associated Equipment*, 354(2-3):389–399, 1995.

[92] X Xufei, M Nocente, F Bonomo, P Franzen, M Fröschle, G Grosso, F Grünauer, R Pasqualotto, M Tardocchi, T Fan, et al. Neutron measurements from beam-target reactions at the elise neutral beam test facility. *Review of Scientific Instruments*, 85(11):11D864, 2014.

[93] TB Ryves. A proton recoil telescope for 12–20 mev neutrons. *Nuclear Instruments and Methods*, 135(3):455–458, 1976.

[94] Alan G Seamster, Ray EL Green, and Ralph G Korteling. Silicon detector δe, e particle identification: A theoretically based analysis algorithm and remarks on the fundamental limits to the resolution of particle type by δe, e measurements. *Nuclear Instruments and Methods*, 145(3):583–591, 1977.

[95] Hans Bethe. Zur theorie des durchgangs schneller korpuskularstrahlen durch materie. *Annalen der Physik*, 397(3):325–400, 1930.

[96] Rathin Saha. The possibility of using a single surface barrier detector as a δe-e telescope for identification of light charged particles (z= 1, 2) and fragments with Z$\leq$ 4. *Nuclear Instruments and Methods in Physics Research Section A: Accelerators, Spectrometers, Detectors and Associated Equipment*, 620(2-3):314–323, 2010.

[97] G Pausch, W Bohne, D Hilscher, H-G Ortlepp, and D Polster. Particle identification in a wide dynamic range based on pulse-shape analysis with solid-state detectors. *Nuclear Instruments and Methods in Physics Research Section A: Accelerators, Spectrometers, Detectors and Associated Equipment*, 349(1):281–284, 1994.

[98] MZMJ Berger. Stopping-power and range tables for electrons, protons, and helium ions: Physical reference data. 1999.

[99] CAJ Ammerlaan, RF Rumphorst, and LA Ch Koerts. Particle identification by pulse shape discrimination in the pin type semiconductor detector. *Nuclear Instruments and Methods*, 22:189–200, 1963.

[100] G Pausch, W Bohne, and D Hilscher. Particle identification in solid-state detectors by means of pulse-shape analysis: results of computer simulations. *Nuclear Instruments and Methods in Physics Research Section A: Accelerators, Spectrometers, Detectors and Associated Equipment*, 337(2-3):573–587, 1994.

[101] Guntram Pausch, H Grawe, D Hilscher, M Moszynski, R Schubart, M De Poli, W Bohne, D Wolski, and GF De Angelis. Application of the pulse-shape technique to proton-alpha discrimination in si-detector arrays. Technical report, SCAN-9507109, 1995.

[102] G Pausch, M Moszynski, W Bohne, J Cederkall, H Grawe, W Klamra, M-O Lampert, P Rohr, R Schubart, W Seidel, et al. Limitations of the pulse-shape technique for particle discrimination in planar si detectors. *IEEE Transactions on Nuclear Science*, 44(3):1040–1045, 1997.

[103] M Mutterer, WH Trzaska, GP Tyurin, AV Evsenin, J Von Kalben, J Kemmer, M Kapusta, VG Lyapin, and SV Khlebnikov. Breakthrough in pulse-shape based particle identification with silicon detectors. In *Nuclear Science Symposium, 1999. Conference Record. 1999 IEEE*, volume 1, pages 148–151. IEEE, 1999.

[104] J Lu, P Figuera, F Amorini, G Cardella, A DiPietro, A Musumarra, M Papa, G Pappalardo, F Rizzo, and S Tudisco. Pulse shape discrimination of charged particles with a silicon strip detector. *Nuclear Instruments and Methods in Physics Research Section A: Accelerators, Spectrometers, Detectors and Associated Equipment*, 471(3):374–379, 2001.

[105] H Hamrita, E Rauly, Y Blumenfeld, B Borderie, M Chabot, P Edelbruck, L Lavergne, J Le Bris, Th Legou, N Le Neindre, et al. Charge and current-sensitive preamplifiers for pulse shape discrimination techniques with silicon detectors. *Nuclear Instruments and Methods in Physics Research Section A: Accelerators, Spectrometers, Detectors and Associated Equipment*, 531(3):607–615, 2004.

[106] M Alderighi, A Anzalone, L Auditore, N Arena, R Bassini, J Blicharska, C Boiano, V Campagna, G Cardella, S Cavallaro, et al. Pulse shape method applied to silicon detectors of chimera array. *Nuclear Physics, Section A*, (734):E88–E91, 2004.

[107] L Bardelli, M Bini, G Casini, P Edelbruck, G Pasquali, G Poggi, S Barlini, R Berjillos, B Borderie, R Bougault, et al. Progresses in the pulse shape identification with silicon detectors within the fazia collaboration. *Nuclear Instruments and Methods in Physics Research Section A: Accelerators, Spectrometers, Detectors and Associated Equipment*, 654(1):272–278, 2011.

[108] N Le Neindre, R Bougault, S Barlini, E Bonnet, B Borderie, G Casini, A Chbihi, P Edelbruck, JD Frankland, D Gruyer, et al. Comparison of charged particle identification using pulse shape discrimination and δe- e methods between front and rear side injection in silicon detectors. *Nuclear Instruments and Methods in Physics Research Section A: Accelerators, Spectrometers, Detectors and Associated Equipment*, 701:145–152, 2013.

[109] JA Duenas, D Mengoni, VV Parkar, R Berjillos, M Assie, D Beaumel, AM Sánchez-Benítez, and I Martel. Identification of light particles by means of pulse shape analysis with silicon detector at low energy. *Nuclear Instruments and Methods in Physics Research Section A: Accelerators, Spectrometers, Detectors and Associated Equipment*, 676:70–73, 2012.

[110] Roberto Pasqualotto, M Agostini, M Barbisan, M Bernardi, M Brombin, R Cavazzana, G Croci, M Dalla Palma, RS Delogu, G Gorini, et al. Progress on development of spider diagnostics. In *AIP Conference Proceedings*, volume 1869, page 030020. AIP Publishing, 2017.

[111] BL Doyle, DK Brice, and WR Wampler. A local mixing model for deuterium replacement in solids. *Radiation Effects Letters*, 57(3):81–88, 1980.

[112] DK Brice, BL Doyle, and WR Wampler. Extended local mixing model for hydrogen retention and isotope exchange. *Journal of Nuclear Materials*, 111:598–605, 1982.

[113] DK Brich and WR Wampler. The local mixing model with sputtering/redeposition and projectile-implanted atom interaction. *Journal of Nuclear Materials*, 145:368–372, 1987.

[114] DK Brice and BL Doyle. A trap activation model for hydrogen retention and isotope exchange in some refractory marterials. *Journal of Nuclear Materials*, 103:503–507, 1981.

[115] Riccardo Nocentini, Ursel Fantz, Peter Franzen, Markus Froeschle, Bernd Heinemann, Rudolf Riedl, Benjamin Ruf, Dirk Wuenderlich, et al. Beam diagnostic tools for the negative hydrogen ion source test facility elise. *Fusion Engineering and Design*, 88(6-8):913–917, 2013.

[116] James F Ziegler, Matthias D Ziegler, and Jochen P Biersack. Srim–the stopping and range of ions in matter (2010). *Nuclear Instruments and Methods in Physics Research Section B: Beam Interactions with Materials and Atoms*, 268(11-12):1818–1823, 2010.

[117] W Möller. The behaviour of hydrogen atoms implanted into metals. *Nuclear Instruments and Methods in Physics Research*, 209:773–790, 1983.

[118] J Sanz, M García, F Ogando, A Mayoral, D López, P Sauvan, and B Brañas. First ifmif/eveda radioprotection studies for the preliminary design of the accelerator beam dump. *Fusion Science and Technology*, 56(1):273–280, 2009.

[119] Jinchoon Kim. Dd neutron and x-ray yields from high-power deuterium beam injectors. *Nuclear Technology*, 44(2):315–321, 1979.

[120] TTC Jones, SJ Cox, A Emmanoulidis, and MJ Loughlin. Prediction of neutron source, tritium production and activation for long-pulse operation of the iter neutral beam test facility. *Nuclear fusion*, 46(6):S352, 2006.

[121] MB Chadwick, P Obložinskỳ, M Herman, NM Greene, RD McKnight, DL Smith, PG Young, RE MacFarlane, GM Hale, SC Frankle, et al. Endf/b-vii. 0: next generation evaluated nuclear data library for nuclear science and technology. *Nuclear data sheets*, 107(12):2931–3060, 2006.

[122] Bernd Heinemann, H Falter, Ursel Fantz, Peter Franzen, Markus Fröschle, R Gutser, W Kraus, R Nocentini, R Riedl, E Speth, et al. Design of the “half-size” iter neutral beam source for the test facility elise. *Fusion Engineering and Design*, 84(2-6):915–922, 2009.

[123] B Heinemann, H-D Falter, U Fantz, P Franzen, M Froeschle, W Kraus, C Martens, R Nocentini, R Riedl, E Speth, et al. The negative ion source test facility elise. *Fusion Engineering and Design*, 86(6-8):768–771, 2011.

[124] P Franzen, D Wünderlich, R Riedl, R Nocentini, F Bonomo, U Fantz, M Fröschle, B Heinemann, C Martens, W Kraus, et al. Status of the elise test facility. In *AIP Conference Proceedings*, volume 1655, page 060001. AIP Publishing, 2015.

[125] B Heinemann, U Fantz, W Kraus, D Wünderlich, F Bonomo, M Fröschle, I Mario, R Nocentini, R Riedl, and C Wimmer. Latest achievements of the negative ion beam test facility elise. *Fusion Engineering and Design*, 2018.

[126] P Franzen, U Fantz, D Wünderlich, B Heinemann, R Riedl, W Kraus, M Fröschle, B Ruf, R Nocentini, NNBI Team, et al. Progress of the elise test facility: results of caesium operation with low rf power. *Nuclear Fusion*, 55(5):053005, 2015.

[127] D Wünderlich, U Fantz, B Heinemann, W Kraus, R Riedl, C Wimmer, NNBI Team, et al. Progress of the elise test facility: towards one hour pulses in hydrogen. *Nuclear Fusion*, 56(10):106004, 2016.

[128] M Nocente, M Tardocchi, A Olariu, S Olariu, RC Pereira, IN Chugunov, A Fernandes, DB Gin, G Grosso, VG Kiptily, et al. High resolution gamma ray spectroscopy at mhz counting rates with labr _{3} scintillators for fusion plasma applications. *IEEE Transactions on Nuclear Science*, 60(2):1408–1415, 2013.

[129] M Nocente, M Tardocchi, I Chugunov, RC Pereira, T Edlington, AM Fernandes, D Gin, G Grosso, V Kiptily, A Murari, et al. Energy resolution of gamma-ray spectroscopy of jet plasmas with a labr 3 scintillator detector and digital data acquisition. *Review of scientific instruments*, 81(10):10D321, 2010.

[130] B Heinemann, U Fantz, P Franzen, M Froeschle, M Kircher, W Kraus, C Martens, R Nocentini, R Riedl, B Ruf, et al. Negative ion test facility elise - status and first results. *Fusion Engineering and Design*, 88(6-8):512–516, 2013.

[131] Riccardo Nocentini, Federica Bonomo, Marina Ricci, Antonio Pimazzoni, Ursel Fantz, Bernd Heinemann, Rudolf Riedl, and Dirk Wünderlich. Beam calorimetry at the large negative ion source test facility elise: Experimental setup and latest results. *Fusion Engineering and Design*, 109:673–677, 2016.

[132] Antonio Pimazzoni. Investigation of elise beam properties by means of the diagnostic calorimeter. 2014.

[133] Molybdenum disulfide. `https://en.wikipedia.org/wiki/Molybdenum_disulfide#cite_note-b92-1`. Accessed 07 September 2018.

[134] William M Haynes. *CRC handbook of chemistry and physics.* CRC press, 2014.

[135] Volker Buck. Structure and density of sputtered mos2-films. *Vacuum*, 36(1-3):89–94, 1986.

[136] R Nocentini, F Bonomo, A Pimazzoni, U Fantz, P Franzen, M Fröschle, B Heinemann, R Pasqualotto, R Riedl, B Ruf, et al. Advanced ion beam calorimetry for the test facility elise. In *AIP Conference Proceedings*, volume 1655, page 060006. AIP Publishing, 2015.

[137] Denise B Pelowitz, Joe W Durkee, Jay S Elson, Michael L Fensin, John S Hendricks, Michael R James, Russell C Johns, Fregg W Mc Kinney, Stepan G Mashnik, Laurie S Waters, et al. Mcnpx 2.7 e extensions. Technical report, Los Alamos National Lab.(LANL), Los Alamos, NM (United States), 2011.

[138] MB Chadwick, PG Young, S Chiba, SC Frankle, GM Hale, HG Hughes, AJ Koning, RC Little, RE MacFarlane, RE Prael, et al. Cross-section evaluations to 150 mev for accelerator-driven systems and implementation in mcnpx. *Nuclear Science and Engineering*, 131(3):293–328, 1999.

[139] MB Chadwick, PG Young, RE MacFarlane, Moller P, GM Hale, RC Little, AJ Koning, and S Chiba. La150 documentation of cross sections, heating, and damage: Part a (incident neutrons) and part b (incident protons). *LA-UR-99-1222*, 1999.

[140] Satoshi Kunieda, Osamu Iwamoto, Nobuyuki Iwamoto, Futoshi Minato, Tsutomu Okamoto, Tatsuhiko Sato, Hiroshi Nakashima, Yosuke Iwamoto, Hiroki Iwamoto, Fumito Kitatani, et al. Overview of jendl-4.0/he and benchmark calculations. Technical report, 2016.

[141] C Cazzaniga, M Tardocchi, G Croci, C Frost, L Giacomelli, G Grosso, Anders Hjalmarsson, M Rebai, NJ Rhodes, EM Schooneveld, et al. First measurement of the vesuvio neutron spectrum in the 30–80 mev energy range using a proton recoil telescope technique. *Journal of Instrumentation*, 8(11):P11008, 2013.

[142] C Cazzaniga, M Nocente, M Tardocchi, Alberto Fazzi, Anders Hjalmarsson, D Rigamonti, Göran Ericsson, and G Gorini. Thin yap: Ce and labr3: Ce scintillators as proton detectors of a thin-film proton recoil neutron spectrometer for fusion and spallation sources applications. *Nuclear Instruments and Methods in Physics Research Section A: Accelerators, Spectrometers, Detectors and Associated Equipment*, 751:19–22, 2014.

[143] C Cazzaniga, M Rebai, M Tardocchi, G Croci, M Nocente, S Ansell, CD Frost, and G Gorini. A telescope proton recoil spectrometer for fast neutron beam-lines. *Progress of Theoretical and Experimental Physics*, 2015(7), 2015.

[144] C Cazzaniga, A Cremona, M Nocente, M Rebai, D Rigamonti, M Tardocchi, G Croci, Göran Ericsson, A Fazzi, Anders Hjalmarsson, et al. Light response of yap: Ce and labr3: Ce scintillators to 4–30 mev protons for applications to telescope proton recoil neutron spectrometers. *Nuclear Instruments and Methods in Physics Research Section A: Accelerators, Spectrometers, Detectors and Associated Equipment*, 820:85–88, 2016.

[145] CIVIDEC instrumentation. C2 broadband amplifier. `https://cividec.at/electronics-C2.html`. Accessed 19 October 2018.

[146] CAEN. Dt5730 desktop waveform digitizer. `http://www.caen.it/csite/CaenProd.jsp?parent=14&idmod=757`. Accessed 19 October 2018.

[147] Martin J Berger. Estar, pstar, and astar: Computer programs for calculating stopping-power and range tables for electrons, protons, and helium ions. 1992.

[148] Lev Davidovich Landau. On the energy loss of fast particles by ionization. *J. Phys.*, 8:201–205, 1944.

[149] Ilka Antcheva, Maarten Ballintijn, Bertrand Bellenot, Marek Biskup, Rene Brun, Nenad Buncic, Ph Canal, Diego Casadei, Olivier Couet, Valery Fine, et al. Root–a c++ framework for petabyte data storage, statistical analysis and visualization. *Computer Physics Communications*, 180(12):2499–2512, 2009.

Synopsis of attached papers

- **Paper I**

  M. Nocente, **S. Feng**, D. Wünderlich, F. Bonomo, G. Croci, U. Fantz, B. Heinemann, W. Kraus, I. Mario, R. Pasqualotto, M. Tardocchi and G. Gorini.

  Experimental investigation of beam-target neutron emission at the ELISE neutral beam test facility

  Fusion Engineering and Design, **123** (2017): 843-846.

  In this paper we performed a dedicated experiment on beam-target neutron emission at the ELISE neutral beamtest facility to investigate the accuracy of Local Mixing Model based calculations of neutron emission of relevance for the design of neutron diagnostics at the SPIDER neutral beam prototype. Compared to a previous experiment, we make use of fully developed infra-red and calorimetry diagnostics to include accurate data on beam profile and current in calculations. Results show that variations of the neutron emission can be predicted with an accuracy better than 10%, which compares to 30% in our previous investigation. At the same time, convincing evidence of diffusion effects beyond the Local Mixing Model is identified in the data. Implications of these findings for neutron emission at SPIDER are discussed.

- **Paper II**

  S. Feng, M. Nocente, D. Wünderlich, F. Bonomo, G. Croci, U. Fantz, B. Heinemann, W. Kraus, I. Mario, A. Muraro, R. Pasqualotto, M. Rebai, M. Tardocchi and G. Gorini.

  Neutron measurements at the ELISE neutral beam test facility and implications for neutron based diagnostics at SPIDER

  Review of Scientific Instruments, **89** (2018): 10I139.

  In this paper we continued our observation from paper I and performed a dedicated experiment on neutron emission from beam-target reactions with beam parameters approaching those expected at SPIDER at the ELISE neutral beam test facility. The time trace of neutron emission has been measured using a calibrated liquid scintillator detector at increasing power densities on the target. Compared to calculations based on the local mixing model, a systematic discrepancy was observed exceeding the statistical accuracy of the measurements and increasing as a linear function of the power density. We then derived an empirical temperature dependent correction with our collected data for applications to neutron measurements at SPIDER.

- **Paper III**

  S. Feng, C. Cazzaniga, T. Minniti, M. Nocente, C. Frost, G. Gorini, A. Muraro, S. Romano and M. Tardocchi.

  Response of a telescope proton recoil spectrometer based on a YAP: Ce scintillator to 5–80 MeV protons for applications to measurements of the fast neutron spectrum at the ChipIr irradiation facility

  Nuclear Instruments and Methods in Physics Research Section A: Accelerators, Spectrometers, Detectors and Associated Equipment, **912** (2018): 36–38.

  In this paper we developed a telescope proton recoil spectrometer consisting of a $500\mu m$ thick silicon detector and a 2.54 cm × 2.54 cm YAP:Ce inorganic scintillator to measure the neutron spectrum at ChipIr, a fast neutron beam line that has recently started operations at the ISIS neutron source in the UK. The spectrometer has been tested with protons in the energy range 5–80 MeV at the INFN-LNS cyclotron accelerator. The light yield of the YAP scintillator to protons has been characterized relative to gamma-rays of same energies and found to scale linearly with the proton energy in the whole range. Background rejection using a $\Delta E - E$ technique by combining data from the silicon and YAP:Ce detectors has also been tested successfully.

Paper I

Fusion Engineering and Design 123 (2017) 843–846

Contents lists available at ScienceDirect

Fusion Engineering and Design

journal homepage: www.elsevier.com/locate/fusengdes

Experimental investigation of beam-target neutron emission at the ELISE neutral beam test facility

M. Nocente[a,b], S. Feng[a], D. Wünderlich[c], F. Bonomo[c], G. Croci[a,b,*], U. Fantz[c], B. Heinemann[c], W. Kraus[c], I. Mario[d], R. Pasqualotto[e], M. Tardocchi[b], G. Gorini[a,b]

[a] *Dipartimento di Fisica "G. Occhialini", Universitá di Milano-Bicocca, Milano, Italy*
[b] *Istituto di Fisica del Plasma, Consiglio Nazionale delle Ricerche, Milano, Italy*
[c] *Max-Planck-Institut für Plasmaphysik, Garching, Germany*
[d] *Universitá degli Studi di Padova, Padova, Italy*
[e] *Consorzio RFX, Padova, Italy*

HIGHLIGHTS

- An experiment on beam-target neutron emission has been performed.
- The experiment is of relevance to predict neutron emission at the SPIDER facility.
- Data are compared to predictions based on the local mixing model.
- Variations of the neutron emission can be described with 10% accuracy with this model.
- Indication of effects beyond the local mixing model is also identified in the data.
- These may reduce neutron emission by 40% at SPIDER compared to a previous calculation.

ARTICLE INFO

Article history:
Received 3 October 2016
Received in revised form 24 March 2017
Accepted 25 March 2017
Available online 14 April 2017

Keywords:
Beam-target neutron emission
Neutral beam injection
Neutron detectors

ABSTRACT

A dedicated experiment on beam-target neutron emission has been performed at the ELISE neutral beam test facility to investigate the accuracy of Local Mixing Model based calculations of neutron emission of relevance for the design of neutron diagnostics at the SPIDER neutral beam prototype. Compared to a previous experiment, we make use of fully developed infra-red and calorimetry diagnostics to include accurate data on beam profile and current in the calculations. Results show that variations of the neutron emission can be predicted with an accuracy better than 10%, which compares to 30% in our previous investigation. At the same time, convincing evidence of diffusion effects beyond the Local Mixing Model is identified in the data. Implications of these findings for neutron emission at SPIDER are discussed.

1. Introduction

In fusion plasmas, 2.5 MeV neutron measurements are traditionally used to provide information of the fuel ion energy distribution in tokamaks [1–3]. More recently, as the focus of fusion research progressively shifts from physics to technological applications, 2.5 MeV neutron detectors using Gas Electron Multipliers [4] have been also proposed as diagnostics of the beam homogeneity for the SPIDER and MITICA Neutral Beam Injection Prototypes (NBI) in Padua. The detector exploits the beam-target neutron emission that occurs when the deuterium beam penetrates in the metallic dump of the NBI prototype.

In order to investigate the detailed physics behind this process and aid the detector design, in 2014 a parasitic experiment [5] was performed at the ELISE facility [6,7] of the Max Planck Institut für Plasmaphysik in Garching. In this first study, a calibrated EJ301 liquid scintillator was used to measure neutron emission and benchmark calculations based on the Local Mixing Model (LMM) of deuterium implantation in the dump. The experimental results were generally found to be consistent with calculations but, at a detailed level, an overestimation of up to 30% of the emission was often observed.

A dedicated experiment was performed at ELISE to clarify this discrepancy and is presented here. The new study makes use of fully developed infra-red and calorimetry diagnostics to provide

---

[*] Corresponding author at: Dipartimento di Fisica "G. Occhialini", Universitá di Milano-Bicocca, Milano, Italy.
E-mail address: gabriele.croci@cern.ch (G. Croci).

http://dx.doi.org/10.1016/j.fusengdes.2017.03.152

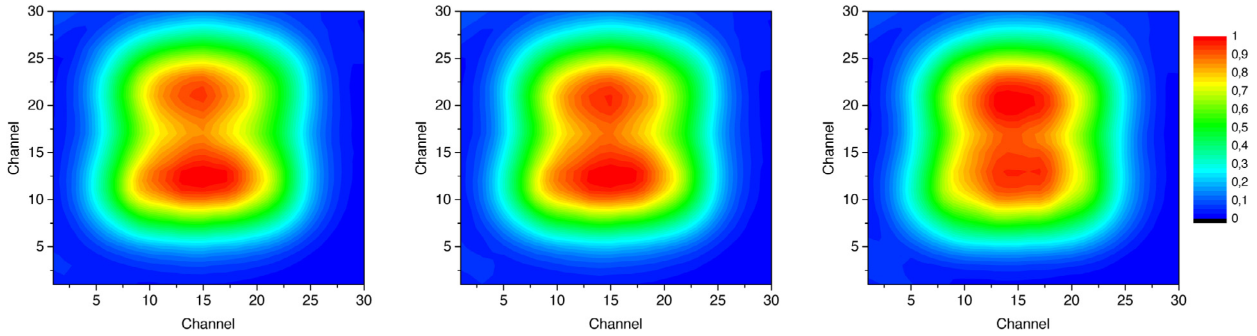

Fig. 1. Beam profiles measured during the neutron emission experiment with the ELISE infra-red camera and normalised to unity. Measurements are shown at $t = 800$, 1200 and 1600 s (from left to right). The times indicated here refer to those in Fig. 2.

more accurate input data for the calculations. Results are analysed as a test of the capability of the LMM to predict the magnitude of neutron emission in beam-target reactions and to trace possible evidence of diffusion effects beyond the LMM in the data.

2. Beam-target neutron emission experiment

The neutron emission experiment we performed consists in a set of pulses at increasing value of the beam current (I) in the range $I = 5$–17 A and at a fixed total voltage $V = 30$ kV. The beam optics was carefully designed so to illuminate most of the dump surface and to achieve very similar beam profiles when the machine was operated at increasing values of the current (see Fig. 1). An infra-red (IR) camera was used to measure the beam profile in each of the discharges we performed. The profile was determined by an image of the infrared map from the dump and which, after careful analysis, provides the power density distribution (W/m^2) on the dump on a 30 × 30 grid.

Neutron emission from the dump was monitored by means of the same neutron detector used in our previous experiment [5], i.e. a calibrated EJ301 liquid scintillator produced by Scionix and coupled to a Hamamatsu H10580 photomultiplier tube. Signals from the liquid scintillator were recorded by a 14 bit, 400 MS/s digitiser based on the ATCA platform [8,9]. A standard neutron/gamma-ray separation algorithm was adopted to discriminate the 3 times more abundant neutrons from gamma-rays and with an estimated failure rate of 5.7%, independently of the beam current.

In order to interpret data, for each of the pulse we performed, the expected time dependent neutron yield was determined based on the Local Mixing Model (LMM) of deuterium deposition in the dump made by 99% of copper. As in [5], we used the TRansport of Ion in Matter (TRIM) code [10] to evaluate the beam penetration in the dump. This was the input to calculate the local deuterium density $n_D(x, t)$, from which the neutron yield $y(x, t)$ (neutrons/m^3/s) is obtained as $y(x, t) = n_D(x, t)\phi(x, t)\sigma$. Here, x indicates an axis orthogonal to the dump surface. ϕ and σ are the impinging deuterium flux and the (energy dependent) 2.5 MeV neutron cross-section, respectively. As more deuterium is implanted in the dump, the concentration $n_D(x, t)$ increases with time until a saturation level is reached (20% of total atoms based on our previous experiment). The total neutron emission Y, which is obtained by integrating $y(x, t)$ over the dump volume, depends on time, as it reflects the increasing deuterium concentration in the dump until it reaches the steady state condition. An essential parameter for the simulations is the impinging deuterium flux ϕ, that is obtained from the current I, whose precise evaluation requires additional care. In our first experiment, we estimated the current reaching the dump by the total extracted current I_{ex}, i.e. the negative ion current that is extracted from the radio-frequency source. The accelerated current reaching the dump, I_{acc}, can be however different from I_{ex}, up to about 20–30%, as some ions are stopped by the grounded grid and the ground shield in their path from the radio-frequency source to the dump [11]. An important improvement of our new experiment has been the capability to precisely evaluate the current reaching the dump, I_{acc}, thanks to water calorimetry measurements at ELISE [12].

3. Results

Fig. 2 left shows the neutron counting rate during our experiment, which consisted of 170 pulses performed in 3 consecutive days after a few days of technical tests in the third deuterium campaign at ELISE. For each pulse we collected data for 10 s and evaluated the average counting rate per pulse shown in the figure. The x axis is the cumulated beam time, i.e. the effective time of beam operations, net of pauses. The current values that were actually delivered by the machine are shown in Fig. 2 right. We aimed in particular at performing measurements at $I = 7$, 12, 15 and 17 A, where the first value corresponds to a region where <10% discrepancies between calculations and data were found in our first experiment. In order to reach the highest currents we optimised Cesium conditioning of the radio-frequency source, the effect of which is seen, for example, in the moderately rising slope at $t = 600$ s in Fig. 2 right. The acceleration voltage was always stable at 30 kV.

As neutron emission responds to changes of the current reaching the calorimeter, as well as to the build up of deuterium concentration in the dump, for each value of I_{ex} we performed several pulses until a sufficiently stationary neutron rate was observed so to enable a clean comparison between data and simulations. This is shown by the dashed and dotted lines in Fig. 2 left, where calculation results based on I_{ex} and I_{acc} are displayed together. As the simulation provides the neutron emission Y as a function of time, we need to evaluate the calibration coefficient k that converts from Y to the experimentally measured neutron rate r_n. Similarly to our previous experiment we have determined k by the ratio between measurements and simulations using data points at $I = 7$ A, so that here the two simulation curves are superimposed on each other. When this is done, from the results of Fig. 2 we observe that, at $t > 600$ s, calculations based on I_{acc} agree better with experimental results, as expected, showing that well calibrated neutron measurements are sensitive even to current variations smaller than 20%, such as the difference between I_{ex} and I_{acc}. As far as the beginning phase ($t < 100$ s) at $I = 7$ A is concerned, we note that our model is less accurate. This is due to some missing beam profile measurements during the technical discharges performed in the days preceding our experiment and is reflected in some uncertainties in our determination of the detailed build up of deuterium concentration before full saturation is reached (stationary neutron emission) at $t > 300$ s.

A closer inspection to Fig. 2 however reveals that, albeit at the level of <10%, there still seems to be a systematic discrepancy

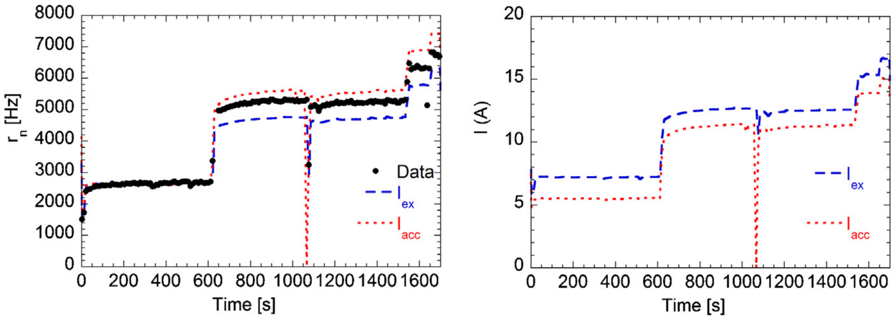

Fig. 2. (left) Measured neutron rate in the experiment performed at ELISE. Data (dots) are compared to a calculation based on the LMM and using as input either the extracted ionic current (I_{ex}, blue-dashed) or the accelerated current determined by calorimetry measurements (I_{acc}, red-dotted). The error bars on the data are of the same size as the dots. (right) Values of I_{acc} and I_{ex} delivered by the machine during the experiment. The drop of I_{acc} at $t \approx 1100$ s is due to a fault of the calorimeter diagnostic in one pulse. (For interpretation of the references to colour in this figure legend, the reader is referred to the web version of this article.)

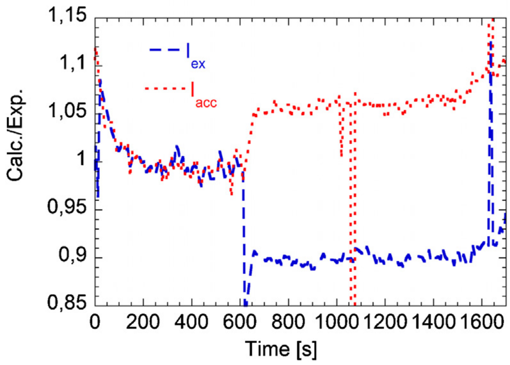

Fig. 3. Ratio between neutron emission the calculations based on I_{acc} and I_{ex} and measured data of Fig. 2.

between measurements and I_{acc} based simulations. This is better indicated by the simulation-to-experiment ratio in Fig. 3, from which we note that I_{acc} based calculations tend to overestimate neutron emission. On the contrary, I_{ex} based calculations always underestimate emission, but the agreement with measurements is improved as I gets larger. Compared to our former experiment, where we observed a disagreement at the level of ≈30% already at $I = 8–10$ A, we can conclude that an accurate knowledge of the beam profile and current is essential for a reliable determination of the neutron emission and improves the agreement to a better than 10% level. The discrepancies observed earlier were most likely due to insufficient input diagnostic information. At the same time, however, we found no way to reconcile the remaining difference and we conclude that some additional deuterium diffusion caused by temperature effects away from the saturation state must be included in the model to completely account for the observations. This process, which is outside the LMM used here, does not play a very important role at the currents and voltages we have tested so far, as we were able to predict neutron emission with an accuracy better than 10%. However, our data provide reasonable evidence that diffusion outside the LMM is at play in beam-target neutron emission experiments and becomes progressively more important as I is increased, as shown in Fig. 3.

4. Discussion

The experiment described in this paper was performed at beam current values $I = 7–17$ A and at a fixed acceleration voltage of 30 kV in pulses lasting 10 seconds each. A maximum discrepancy of about 10% was observed between measurements and simulations once complete diagnostic information on the beam parameters were carefully included in the calculations under well controlled conditions. For comparison, SPIDER is meant to operate with $I = 40$ A, $V = 100$ kV, up to 1 h beam pulses and a twice larger beam dump. The power $I \cdot V$ delivered on the dump by the beam at SPIDER will therefore be about 8 times larger compared to our experiment. If we assume that deuterium diffusion outside the LMM scales as the beam power density, LMM based neutron emission calculations for SPIDER [13] may be overestimated by up to a factor 1.4. This suggests that a quantification of the diffusion coefficient that needs to be added to the neutron emission model is needed for reliable predictions at SPIDER. In this paper, we do not have data at $I > 17$ V and $V > 30$ kV to aim at this quantification, but we limit ourselves to highlighting the parameters (beam profile, current on the dump) that are important for careful beam-target neutron calculations and to providing clear experimental evidence of the role of diffusion effects beyond the LMM in beam-target neutron emission. At the same time, we mention here that such quantification may be possible in future high power deuterium campaigns at ELISE if the machine is operated at parameters close to the maximum design performance, i.e. $I = 20$ A and $V = 60$ kV. This would correspond to a power on the dump of 1.2 MW, i.e. still a factor of 3 less than SPIDER, but also a factor 2 more than obtained at the largest currents of the present experiment, which is judged relevant to quantitatively study deuterium diffusion effects.

5. Conclusions

A dedicated experiment on beam-target neutron emission has been performed at the ELISE neutral beam test facility to investigate the accuracy of Local Mixing Model based calculations of neutron emission of relevance for the design of neutron diagnostics at SPIDER. Compared to a previous investigation, the experiment made use of fully developed beam current and profile diagnostics. We find that variations of the neutron emission can be described with an accuracy better than 10% at $V = 30$ kV and $I = 7–17$ A, which compares to about 30% in the previous experiment where no accurate knowledge of the beam profile and current was available. The emission is mostly sensitive to variations of the current hitting the dump. At a more detailed level, the experimental results also reveal that diffusion effects beyond the Local Mixing Model are at play in beam-target reactions and may reduce neutron emission up to a factor 1.4 in full power operations at SPIDER compared to a previous evaluation.

Acknowledgments

The work leading to this publication was funded partially by Fusion for Energy under the Contract No. F4E-RFXPMS_A-WP-2016.

The views and expression expressed herein do not necessarily reflect those of the Fusion for Energy and ITER organizations.

References

[1] M. Nocente, et al., Nucl. Fusion 54 (10) (2014) 104010.
[2] C. Cazzaniga, et al., Rev. Sci. Instrum. 85 (4) (2014) 043506.
[3] J. Eriksson, et al., Nucl. Fusion 55 (12) (2015) 123026.
[4] G. Croci, et al., JINST 7 (2012) C03010.
[5] X. Xufei, et al., Rev. Sci. Instrum. 85 (2014) 11D864.
[6] P. Franzen, et al., Nucl. Fusion 55 (2015) 053005.
[7] B. Heinemann, et al., Fusion Eng. Des. 84 (2009) 915.
[8] M. Nocente, et al., Rev. Sci. Instrum. 81 (2010) 10D321.
[9] M. Nocente, et al., IEEE Trans. Nucl. Sci. 60 (2) (2013) 1408.
[10] J. Ziegler, SRIM/TRIM code, http://www.srim.org.
[11] P. Franzen, AIP Conf. Proc. 1655 (2015) 060001.
[12] R. Nocentini, et al., Fusion Eng. Des. 88 (6–8) (2013) 913.
[13] M. Rebai, PhD thesis, http://hdl.handle.net/10281/28449.

Paper II

REVIEW OF SCIENTIFIC INSTRUMENTS **89**, 10I139 (2018)

Neutron measurements at the ELISE neutral beam test facility and implications for neutron based diagnostics at SPIDER

S. Feng,[1,a)] M. Nocente,[1,2,b)] D. Wünderlich,[3] F. Bonomo,[3] G. Croci,[1,2] U. Fantz,[3]
B. Heinemann,[3] W. Kraus,[3] I. Mario,[3] A. Muraro,[2] R. Pasqualotto,[4]
M. Rebai,[2] M. Tardocchi,[2] and G. Gorini[1,2]
[1]*Dipartimento di Fisica "G. Occhialini," Università di Milano-Bicocca, Milano, Italy*
[2]*Istituto di Fisica del Plasma "P. Caldirola," Consiglio Nazionale delle Ricerche, Milano, Italy*
[3]*Max Planck Institut für Plasmaphysik, Garching, Germany*
[4]*Consorzio RFX, Padova, Italy*

(Presented 16 April 2018; received 19 April 2018; accepted 3 July 2018;
published online 17 October 2018)

Along the route to the development of a neutral beam injector for ITER, the Padua based Source for Production of Ion of Deuterium Extracted from Rf plasma (SPIDER) and megavolt ITER injector and concept advancement facilities will make use of neutron diagnostics to quantify the homogeneity of the neutral beam profile by measuring the map of the neutron emission from the beam dump with the close-contact neutron emission surface mapping (CNESM) system. Neutrons are here produced from beam-target reactions between the deuterium beam and the deuterons previously adsorbed in the calorimeter. In order to aid the interpretation of the diagnostic data, a dedicated experiment on neutron emission from beam-target reactions with beam parameters approaching those expected at SPIDER has been performed at the Extraction from a Large Ion Source Experiment (ELISE) neutral beam test facility. The time trace of neutron emission has been measured using a calibrated liquid scintillator detector at increasing power densities on the target. Compared to calculations based on the local mixing model, a systematic discrepancy was observed exceeding the statistical accuracy of the measurements and increasing as a linear function of the power density. The data are used to derive an empirical temperature dependent correction for applications to neutron measurements at SPIDER. *Published by AIP Publishing.* https://doi.org/10.1063/1.5036823

I. INTRODUCTION

The PRIMA (Padova Research on ITER Megavolt Accelerator) neutral beam test facility which is designed to demonstrate the feasibility of a prototype neutral beam injector for ITER is under construction in Padova, Italy.[1,2] PRIMA includes the negative ion source SPIDER (Source for Production of Ion of Deuterium Extracted from Rf plasma) and the full power injector MITICA (Megavolt ITER Injector and Concept Advancement). SPIDER is the necessary step before MITICA because it has to demonstrate extraction and acceleration to 100 keV of a large negative ion hydrogen or deuterium beam with uniform intensity and low divergence. In order to well estimate the beam uniformity and divergence, a set of diagnostics including the CNESM (close-contact neutron emission surface mapping) system have been designed.[3] The CNESM system is based on Gas Electron Multiplier (GEM) detectors for neutron detection with the aim to resolve the 2D beam intensity profile in deuterium operations at SPIDER.[4–7] Here, fusion reactions between beam deuterons and deuterons implanted in the copper beam dump will produce about 10^{12} neutrons/s spread over 1 m^2. Then the footprint of the deuterium beam that hits the dump can be retrieved from the spatial map of the neutron emission intensity obtained by the CNESM.[8–10] In SPIDER, CNESM will be benchmarked by the Short-Time Retractable Instrumented Kalorimeter Experiment (STRIKE), an inertially cooled calorimeter as the main diagnostics for the beam profile mainly based on Infrared (IR) measurements. As IR measurements cannot be used on MITICA due to engineering constraints, the experience gained at SPIDER will be instrumental to make CNESM the reference system for deuterium beam profile measurements on MITICA.[11] In order to aid the detector development, neutron emission from $D(d,n)^3$He reactions in the beam target experiment must be investigated first.

A parasitic experiment was first performed at the Extraction from a Large Ion Source Experiment (ELISE) facility.[12] The time evolution of beam-target neutron emission from the dump was measured by using a calibrated EJ301 liquid scintillator and has been compared with calculations based on the Local Mixing Model (LMM)[13,14] on a relative scale. Calculations could reproduce the general qualitative features of the measured time trace of neutron emission but, at a more quantitative level, overestimated the neutron emission up to 30%, which could be due to systematic uncertainties of the input data. Benefiting from later refinements of the method to analyze data from the diagnostic calorimeter,[11] a moderate discrepancy up to 12% between the LMM based calculation and data in the power range 160 kW to 440 kW has been revealed

---

Note: Paper published as part of the Proceedings of the 22nd Topical Conference on High-Temperature Plasma Diagnostics, San Diego, California, April 2018.

[a)] Electronic mail: f.song@campus.unimib.it
[b)] Electronic mail: massimo.nocente@mib.infn.it

in a new experiment.[15] This, if extrapolated to SPIDER, would imply a deficit as large as 70% in full power deuterium operations. On the other hand, the power density on the dump at SPIDER will be a factor four larger than the values tested at ELISE in our previous experiment[15] and a linear, empirical extrapolation of our results to SPIDER might be questionable.

To the purpose of verifying whether the deficit still extrapolates linearly toward the beam power expected at SPIDER, we have performed a dedicated experiment that explores a parameter range approaching the maximum capabilities allowed by the ELISE facility[16] of the Max Planck Institut für Plasmaphysik (IPP) (Garching, Germany), where the beam power was scanned from about 200 kW to 950 kW by modifying the beam current and/or voltage in a controlled manner. Particular attention was paid to ensuring a constant beam size and profile as the power was scanned. A neutron detector was used to monitor the time trace of neutron emission and the result has been compared with LMM based calculations on a relative scale (see below). The results are also used to determine an empirical correction for CNESM applications at SPIDER.

II. BEAM-TARGET NEUTRON EMISSION EXPERIMENT

A. Operation of pulsed deuterium beams

ELISE is a half size ITER neutral beam injection (NBI) test facility which can produce a negative ion beam up to 60 keV for 10 s (s) every 3 min.[17,18] The experiment here described is based on 231 deuterium pulses in 3 different experimental days. For each pulse, we measured the time trace of the neutron emission as a function of time with the calibrated liquid scintillator described below. The filling pressure was set to 0.6 Pa and the operation parameters including the average beam currents, high voltages (HV), and power on the dump in the experiment are shown in Table I. For pulses marked by an asterisk, the power on the dump was gradually increased up to the target value. For those pulses, the starting value of the power, HV, and current used are also indicated within parentheses. The highest beam power deposited on the dump was achieved at about 950 kW.

A copper calorimeter (with a total surface of 1.2 m × 1.2 m) consists of 30 × 30 blocks[11] and is placed at a distance of 3.5 m from the extraction and acceleration system[19] to stop the beam. Each block is made of pure copper (38 × 38 × 25 mm) and can be considered as an inertial dump. It is cooled down in the time interval between two consecutive pulses by the cooling system on the rear side of the blocks. The side facing the beam is coated with molybdenum disulfide (MoS_2) to perform IR analysis. This is done by a FLIR A655sc IR micro-bolometer camera which is triggered 5 s before the HV phase and acquires IR images for 1 min, including the 10 s beam time. Thermocouples installed in 48 copper blocks of the calorimeter make it possible to calibrate the camera on an absolute scale. From the power deposition on the calorimeter surface, one can then determine a 2D profile of the beam current on the dump, as well as the beam size and uniformity for later use in the calculations (see Sec. III). A 2D beam power map (profile) at low (300 kW) and high (900 kW) power deposition (W/m^2) is shown in Fig. 1. The profile is very similar in the two cases as, in the experiment, we have designed the beam parameters on purpose to achieve comparable profiles at different powers.

TABLE I. Operation parameters of the deuterium beam in the neutron emission experiment.

Nr. pulses	Power (kW)	HV (keV)	Current (A)
4	190	30.1	6.3
20	214	30.1	7.1
22	304	30.1	10.1
21	397	35.1	11.3
21	500	37.6	13.3
23	605	42	14.4
16*	683 (160)	46.5 (30.1)	14.7 (5.3)
22	706	47.1	15
28	784	49.3	15.9
8*	592 (210)	44.5 (35)	13.3 (6.0)
21	655	45.5	14.4
25	898	54.1	16.6

B. Time trace of neutron emission measurements

Neutron emission is measured by the calibrated Scionix-EJ301A liquid scintillator used also in our previous experiment.[12] The scintillator measures the neutron counting rate and was coupled to an active base H10580 Hamamatsu photomultiplier tube (PMT). The detector was installed in vicinity of one of the two inner walls of the ELISE facility, at a distance of approximately 2.8 m behind the beam dump and with same experimental arrangement described in Ref. 12. Signals coming from the detector were digitized by means of a 14 bit, 400 MS/s custom digitizer based on the Advanced Telecommunications Computing Architecture (ATCA) platform.[20,21] A neutron low energy threshold of 1.15 MeV was used in the measurements. Neutron/gamma-ray discrimination is based on standard long/short gate charge integration. We estimate the probability of a wrong neutron/gamma-ray event discrimination to be about 6%. A neutron/gamma-ray ratio of about 3 was found experimentally.

III. LOCAL MIXING MODEL BASED CALCULATIONS

Neutron emission calculations are based on the LMM model of deuterium implantation in the dump, where diffusion or migration of deuterium is neglected once it is implanted. In more details, the flux of deuterium beam on the ith row and jth column block of the dump, at a depth z and at a time t, $\Phi_{i,j}(z, t)$, can be calculated as

$$\Phi_{i,j}(z,t) = \Phi_{i,j}(0,t)\left(1 - \int_0^z p(x)dx\right). \quad (1)$$

Here $p(x)$ is the probability for the deposition of a deuteron at a depth x and depends on the incident energy significantly. In the LMM, no other reactions but deposition has been assumed and the probability of deposition in depth has been normalised to one. The TRansport of Ion in Matter (TRIM) code[22] has been applied to calculate the $p(x)$ for 27-60 keV incident deuterons with a step of 0.5 keV. The dump density was set to 8.902 g/cm^3. $\Phi_{i,j}(0, t)$ is the incident deuterium flux. This is

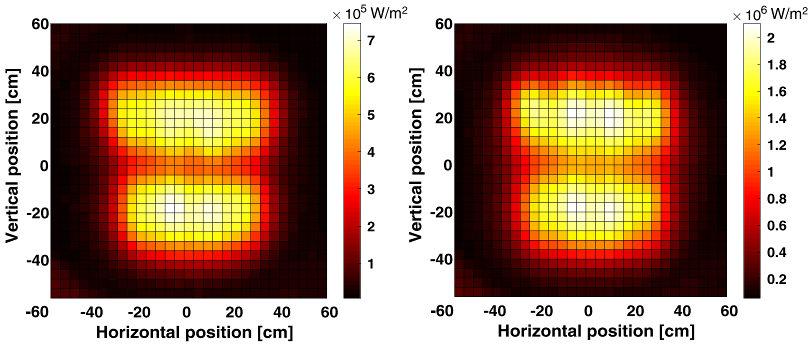

FIG. 1. Beam profile measured in the neutron emission experiment by the ELISE infra-red camera at low (300 kW, left) and high (900 kW, right) power deposition.

in turn given by

$$\Phi_{i,j}(0,t) = \frac{I_{i,j}}{\Delta S \cdot q}, \tag{2}$$

where $I_{i,j}$ is the current that reaches the ith row and jth column block of the dump, ΔS is the area of each block, and q is the ion charge. $I_{i,j}$ is obtained by dividing the known power on each block by the acceleration voltage.

The time resolved neutron yield from the dump $Y(t)$ can be determined from $\Phi_{i,j}(z, t)$ as

$$Y(t) = \sum_{i=1}^{30}\sum_{j=1}^{30}\int_0^R \Phi_{i,j}(z,t)n_{i,j}(z,t)\sigma(z,t)dz \times \Delta S. \tag{3}$$

Here, $n_{i,j}(z, t)$ is the time dependent number of deuterons that get deposited per unit volume at a depth z, and $\sigma(z, t)$ is the $D(d,n)^3$He neutron production cross section (see below).

Ion implantation of hydrogen isotopes into metals can yield high concentrations of atoms.[23] The concentration here is defined as the percentage of deuterons to target atoms per unit volume. As the incident deuterons penetrate in the dump, the local deuteron concentration increases until a maximum is reached (saturation) and which depends on the target material.[13] Based on the results of our previous experiment,[9,12] we have used 20% as concentration at saturation.[24]

The cross section $\sigma(z, t)$ is related to the deuteron energy. The energies of deuterons at depth z have been calculated by using the total stopping power data from the TRIM code so as to convert the energy dependent $D(d,n)^3$He cross section to a function that depends on the depth z. Figure 2 shows an example of the deuteron energy and the $D(d,n)^3$He cross section as a function of depth for 40 keV incident deuterons. From the figure, we note that the effective layer from which neutrons are produced is only 0.5 μm thick and that most neutrons are produced within the first 0.2 μm.

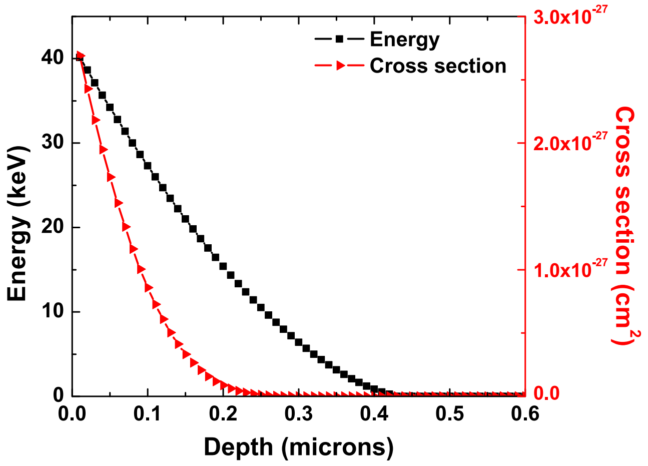

FIG. 2. Deuteron energy (left scale) and the $D(d,n)^3$He cross section (right scale) as a function of depth at 40 keV.

IV. RESULTS

Before the dedicated experiment, a set of experiments with a 22-44 keV deuterium beam was performed from the beginning of the deuterium campaign so that we could assume that deuterium density reached saturation before our dedicated investigation. Figure 3 shows the LMM based calculation of the time trace of neutron emission together with the measurement in our dedicated experiment. The calculation is based on Eq. (3) and uses as input the measured diagnostic information on the beam (current, voltage, and profile). In general, the LMM based calculation reproduces the basic features of the emission, i.e., the step ladder increase of the neutron yield as the beam power on the target is increased. In order to compare simulations and measurements in a more quantitative way, the conversion coefficient k from $Y(t)$ (neutron/s from the target) to the detector counting rate must be determined. As k depends only on the neutron transport from the dump to the detector, it can be empirically evaluated by the ratio between the simulation and measurements at one experimental point where the

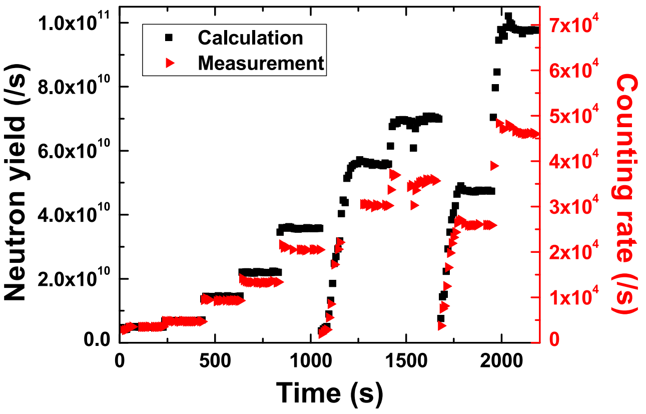

FIG. 3. Calculated neutron emission from the dump as a function of time (left axis) compared to the measured counting rate (right axis).

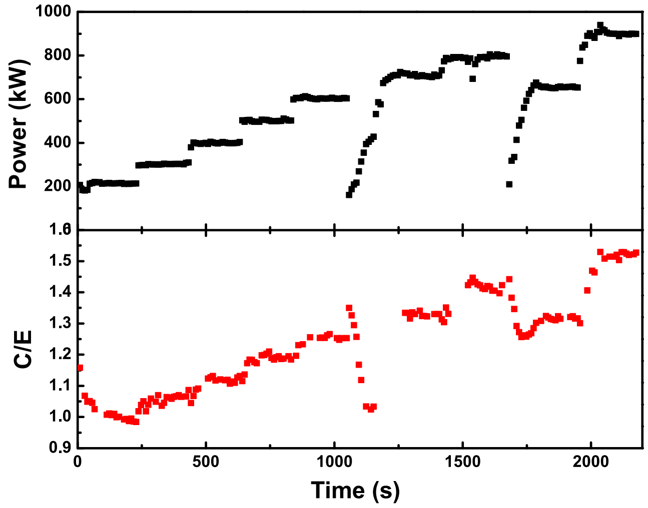

FIG. 4. (top) Beam power impinging on the dump as a function of time (bottom) Ratio between the calculated and measured neutron yield as a function of time.

LMM based calculation is assumed to be correct, and data at 200 kW on the dump between t = 114 s and t = 209 s have been used to calculate *k*.

Using this value, we can then compare measurements and calculations on a quantitative ground, albeit on a relative scale, as shown in Fig. 4. If the LMM model held exactly at any power on the dump, we would expect a ratio between the calculated and experimental neutron rate $C/E = 1$, but this contradicts the experimental data. Instead, we observe that the model calculates systematically more neutrons than found experimentally, i.e., $C/E > 1$. A graph of C/E as a function of the power on the dump (Fig. 5) shows a linear correlation between the two parameters, but for a few outliers. These correspond to the first few pulses of each experimental day when, presumably, a full saturation of the deuterium concentration in the dump was not yet reached. A linear fit to the data of Fig. 5 yields $C/E = (7.1 \pm 0.1) \times 10^{-4} \times Power + (0.841 \pm 0.008)$. The C/E values obtained by the experimental fit in this paper agree within 5% with those found in our previous study[15] in the lower power range where the two experiments overlap.

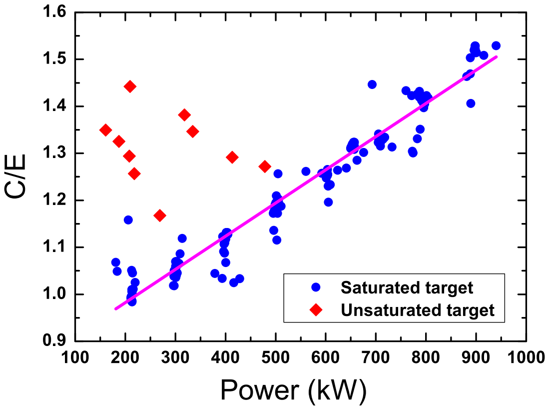

FIG. 5. Ratio *C/E* between the calculated and measured neutron emission as a function of the power on the dump.

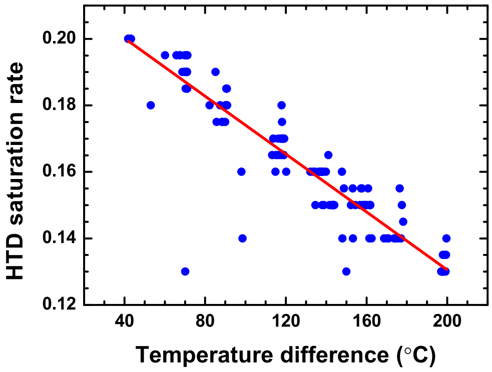

FIG. 6. Temperature dependent saturation rate as a function of the temperature difference after and before the beam irradiation.

V. DISCUSSION

LMM based calculations require three measured quantities as input, i.e., the beam profile, the current on the dump, and the beam voltage. Each of them has an estimated uncertainty of 5%, which yields to an uncertainty in the calculation and is reflected in the fluctuation of the points at each constant power level in Fig. 5. Although this is certainly a visible effect, its magnitude is lower than the systematic trend of the deficit observed in the same figure and we judge it to have a negligible impact on our conclusion on the discrepancy between LMM based calculation and data.

In order to understand the results of Fig. 5, we can make the hypothesis that the dominant effect is a reduction of the deuterium concentration at saturation as a function of temperature. Qualitatively, one can expect temperature to promote the diffusion of deuterium in the dump and we here speculate that this is manifested in the different concentrations reached at saturation as a function of temperature. The IR diagnostics installed at ELISE determines the difference ΔT between the average temperature of each individual block of the beam dump before and after irradiation.[11] By defining the hypothetical temperature dependent saturation rate (HTDSR) as the concentration at saturation required to exactly match the experimental data at each temperature, we can use the results of the experiment to find HTDSR as a function of ΔT averaged over the dump surface (Fig. 6). As for Fig. 3, we have assumed that the concentration at saturation is 20% at a power of 200 kW. Data show a linear decrease of HTDSR versus ΔT which is described as $HTDSR = -4.35 \times 10^{-4} \times \Delta T + 0.218$. This formula can be used as an empirical correction for neutron emission calculations at SPIDER.

VI. CONCLUSIONS

A dedicated experiment on beam-target neutron emission has been performed at the ELISE neutral beam test facility to study the discrepancy between measurements and calculations in a power density range approaching that of SPIDER. The time trace of the neutron emission has been monitored by a calibrated neutron detector and the local mixing model has been applied for predictions. The ratio between calculations and measurements (C/E) on a relative scale has been found to exceed unity beyond the observed fluctuation level of the data points at constant power and to scale linearly with the beam power in the range 200 kW–950 kW. Assuming this can be explained by a temperature dependent saturation rate of deuterons in the target, an empirical correction to neutron emission calculations for applications at SPIDER has been derived.

ACKNOWLEDGMENTS

The work leading to this publication was funded partially by the Fusion for Energy under the Contract No. F4E-RFXPMS A-WP-2017. The views and expression expressed herein do not necessarily reflect those of the Fusion for Energy and ITER organizations.

[1] V. Toigo, D. Boilson, T. Bonicelli, R. Piovan, M. Hanada, A. Chakraborty, G. Agarici, V. Antoni, U. Baruah, M. Bigi *et al.*, Nucl. Fusion **55**, 083025 (2015).

[2] V. Toigo, R. Piovan, S. Dal Bello, E. Gaio, A. Luchetta, R. Pasqualotto, P. Zaccaria, M. Bigi, G. Chitarin, D. Marcuzzi *et al.*, New J. Phys. **19**, 085004 (2017).

[3] R. Pasqualotto, M. Agostini, M. Barbisan, M. Bernardi, M. Brombin, R. Cavazzana, G. Croci, M. D. Palma, R. Delogu, G. Gorini *et al.*, AIP Conf. Proc. **1869**, 030020 (2017).

[4] F. Murtas, G. Croci, G. Claps, M. Cavenago, M. Dalla Palma, G. Gervasini, G. Grosso, R. Pasqualotto, E. P. Cippo, M. Rebai *et al.*, in *2011 IEEE Nuclear Science Symposium and Medical Imaging Conference (NSS/MIC)* (IEEE, 2011), pp. 405–408.

[5] G. Croci, M. Rebai, G. Claps, M. Cavenago, M. Dalla Palma, G. Gervasini, G. Grosso, F. Murtas, R. Pasqualotto, E. P. Cippo *et al.*, J. Instrum. **7**, C03010 (2012).

[6] A. Muraro, G. Croci, G. Albani, C. Cazzaniga, G. Claps, M. Cavenago, G. Grosso, M. Dalla Palma, M. Fincato, F. Murtas *et al.*, Fusion Eng. Des. **96**, 311 (2015).

[7] A. Muraro, G. Croci, G. Albani, G. Claps, M. Cavenago, C. Cazzaniga, M. Dalla Palma, G. Grosso, F. Murtas, R. Pasqualotto *et al.*, Nucl. Instrum. Methods Phys. Res., Sect. A **813**, 147 (2016).

[8] M. Rebai, M. Cavenago, G. Croci, M. Dalla Palma, G. Gervasini, F. Ghezzi, G. Grosso, F. Murtas, R. Pasqualotto, E. Perelli Cippo *et al.*, Rev. Sci. Instrum. **83**, 02B721 (2012).

[9] M. Rebai, Ph.D. thesis, Università degli Studi di Milano-Bicocca, 2012, http://hdl.handle.net/10281/28449.

[10] M. Rebai, G. Croci, G. Grosso, A. Muraro, E. P. Cippo, M. Tardocchi, M. Dalla Palma, R. Pasqualotto, M. Tollin, F. Murtas *et al.*, J. Instrum. **12**, C01007 (2017).

[11] R. Nocentini, F. Bonomo, A. Pimazzoni, U. Fantz, P. Franzen, M. Fröschle, B. Heinemann, R. Pasqualotto, R. Riedl, B. Ruf *et al.*, AIP Conf. Proc. **1655**, 060006 (2015).

[12] X. Xufei, M. Nocente, F. Bonomo, P. Franzen, M. Fröschle, G. Grosso, F. Grünauer, R. Pasqualotto, M. Tardocchi, T. Fan *et al.*, Rev. Sci. Instrum. **85**, 11D864 (2014).

[13] B. L. Doyle, D. K. Brice, and W. R. Wampler, Radiat. Eff. **57**(3), 81 (1981).

[14] D. Brice, B. Doyle, and W. Wampler, J. Nucl. Mater. **111**, 598 (1982).

[15] M. Nocente, S. Feng, D. Wünderlich, F. Bonomo, G. Croci, U. Fantz, B. Heinemann, W. Kraus, I. Mario, R. Pasqualotto *et al.*, Fusion Eng. Des. **123**, 843 (2017).

[16] P. Franzen, U. Fantz, D. Wünderlich, B. Heinemann, R. Riedl, W. Kraus, M. Fröschle, B. Ruf, R. Nocentini, NNBI Team *et al.*, Nucl. Fusion **55**, 053005 (2015).

[17] D. Wünderlich, U. Fantz, B. Heinemann, W. Kraus, R. Riedl, C. Wimmer, NNBI Team *et al.*, Nucl. Fusion **56**, 106004 (2016).

[18] A. Pimazzoni, Ph.D. thesis, Università degli Studi di Padova, 2014, http://tesi.cab.unipd.it/46495/.

[19] R. Nocentini, U. Fantz, P. Franzen, M. Froeschle, B. Heinemann, R. Riedl, B. Ruf, D. Wuenderlich *et al.*, Fusion Eng. Des. **88**, 913 (2013).

[20] M. Nocente, M. Tardocchi, I. Chugunov, R. Pereira, T. Edlington, A. Fernandes, D. Gin, G. Grosso, V. Kiptily, A. Murari *et al.*, Rev. Sci. Instrum. **81**, 10D321 (2010).

[21] M. Nocente, M. Tardocchi, A. Olariu, S. Olariu, R. Pereira, I. Chugunov, A. Fernandes, D. Gin, G. Grosso, V. Kiptily *et al.*, IEEE Trans. Nucl. Sci. **60**, 1408 (2013).

[22] J. F. Ziegler, M. D. Ziegler, and J. P. Biersack, Nucl. Instrum. Methods Phys. Res., Sect. B **268**, 1818 (2010).

[23] W. Möller, Nucl. Instrum. Methods Phys. Res. **209**, 773 (1983).

[24] J. Kim, Nucl. Technol. **44**, 315 (1979).

Paper III

Nuclear Inst. and Methods in Physics Research, A 912 (2018) 36–38

Contents lists available at ScienceDirect

Nuclear Inst. and Methods in Physics Research, A

journal homepage: www.elsevier.com/locate/nima

Response of a telescope proton recoil spectrometer based on a YAP: Ce scintillator to 5–80 MeV protons for applications to measurements of the fast neutron spectrum at the ChipIr irradiation facility

S. Feng [a,*], C. Cazzaniga [b,*], T. Minniti [b], M. Nocente [a,c], C. Frost [b], G. Gorini [a,c], A. Muraro [c], S. Romano [d], M. Tardocchi [c]

[a] *Dipartimento di Fisica "G. Occhialini", Università di Milano-Bicocca, Milano, Italy*
[b] *ISIS Facility, STFC, Rutherford Appleton Laboratory, Didcot, UK*
[c] *Istituto di Fisica del Plasma, Consiglio Nazionale delle Ricerche, Milano, Italy*
[d] *Istituto Nazionale di Fisica Nucleare, Laboratori Nazionali del Sud, Catania, Italy*

ARTICLE INFO

Keywords:
Neutron spectroscopy
Proton recoil telescope
Scintillators

ABSTRACT

A telescope proton recoil spectrometer consisting of a 500 μm thick silicon detector and a 2.54 cm × 2.54 cm YAP:Ce inorganic scintillator has been developed to measure the neutron spectrum at ChipIr, a fast neutron beam line that has recently started operations at the ISIS neutron source in the UK. The spectrometer has been tested with protons in the range 5–80 MeV at the INFN-LNS cyclotron accelerator. The light yield of the YAP scintillator to protons has been characterized relative to gamma-rays of same energies and found to scale linearly with the proton energy in the whole range. Background rejection using a ΔE-E technique by combining data from the silicon and YAP:Ce detectors has also been tested successfully.

1. Introduction

The new beam-line ChipIr has been built at the ISIS neutron source of the Rutherford Appleton Laboratory (UK) for neutron irradiation of electronic and avionic devices and systems [1]. ChipIr is designed to provide a fast neutron spectrum that mimics the atmospheric one with approximately $10^8 - 10^9$ times higher intensity at ground level [2]. The neutron energy spectrum and the flux spatial distribution of fast neutron beam-lines (e.g. ChipIr) are determined on the basis of Monte Carlo calculations that try to reproduce the complexity of nuclear and intra-nuclear interactions up to 800 MeV. Direct measurements of these quantities are needed for the characterization of the neutron flux, to benchmark the simulations, and for a better understanding of the underlying physics of this type of facilities.

A Telescope Proton Recoil spectrometer (TPR) has been developed for measuring the fast neutron spectrum in the energy range 10 MeV $< E_n <$ 120 MeV [3]. The TPR system is composed by a plastic scatterer to convert neutrons into recoil protons and a high resolution proton spectrometer. The latter is based on a YAP:Ce fast inorganic scintillator with an energy resolution in the range 5%–10% at 0.6 MeV and a fast decay time (< 50 ns) to minimize pileup for operations at high background counting rates (say, 100 kHz - 1 MHz background induced by environmental γ-rays) [4]. The scintillator is used in coincidence with a silicon (Si) detector (ΔE measurement) for background reduction and particle discrimination [5]. In order to characterize the performance of YAP:Ce scintillator as a proton spectrometer, measurements of its light yield to protons have been previously performed [4] at the Uppsala tandem accelerator in the energy range 4–8 MeV and at the Legnaro Tandem ALPI-PIAVE accelerator in 9–20 MeV energy range [6]. In those tests, a 2.54 cm × 0.2 cm thick YAP crystal was used and the whole detector concept was latter assessed for the first time at the VESUVIO beam line [3,7].

In this work, we extend the characterization of the light yield of a 2.54 cm × 2.54 cm (diameter × height) YAP:Ce scintillator to protons with energies up to 80 MeV, such as those needed to determine the neutron spectrum up to 150 MeV at ChipIr. In particular, we determine the linearity of the light yield in this energy range and discuss the results in view of applications at ChipIr.

---

[*] Corresponding authors.
E-mail addresses: fengs9115@gmail.com (S. Feng), carlo.cazzaniga@stfc.ac.uk (C. Cazzaniga).

https://doi.org/10.1016/j.nima.2017.10.026
Received 29 September 2017; Received in revised form 10 October 2017; Accepted 10 October 2017
Available online 18 October 2017
0168-9002/© 2017 Elsevier B.V. All rights reserved.

2. Experimental setup

The TPR neutron spectrometer consists of a 2.54 cm × 2.54 cm YAP:Ce scintillator and a Si detector (2.54 cm × 0.5 mm). The entrance of the YAP scintillator was covered by a 30 μm thick Al foil for the optimization of light collection. The Si detector was also covered by a layer of 30 μm thick Al foil on two sides to shield from light and electromagnetic noise.

The YAP scintillator was coupled to a Hamamatsu R9420–100–10mod Photo-multiplier-tube (PMT) and operated with negative voltage at 650 V so to cover the whole proton energy range. The Si detector was equipped with a low-noise current preamplifier (CIVIDEC C2). The detector is reverse biased at +170 V. All signals were fed directly into a 500 MSamples/s digitizer (CAEN DT5730) and were saved by triggering the signals on YAP scintillator. The waveforms are then analyzed off-line for coincidence and pulse height analysis.

The measurements have been performed with 62 MeV and 80 MeV proton beams using the cyclotron accelerator at INFN-LNS. Aluminum foils of different thicknesses have been used to reduce the energy of protons impinging on the TPR spectrometer and obtain measurement points in the 5–80 MeV range. As the flux of the direct proton beam would be too intense to measure, a Rutherford scattering configuration has been used to reduce the flux on detectors. This was obtained by using a 0.25 mm thick polyethylene target as a scatterer to produce recoil protons from the primary beam. The TPR spectrometer was then placed at a distance of 30.8 cm from the target with an angle of 27° with respect to the incident proton beam. The angle was chosen to be large enough so that the detectors and their supporting structures did not intercept the beam but, at the same time, so to ensure a high enough signal on the detector.

3. TPR coincidence measurements

3.1. Background rejection and particle discrimination

Two events, recorded by the Si detector (ΔE) and by the YAP:Ce scintillator (E) with a same trigger, are considered to be coincident if the time interval Δt between them falls within an acceptance window. The center of this time window T_c was determined by observing the peak which stands out from a continuum of random coincidences in a histogram of Δt vs coincidence events. We obtained T_c = 27.6 ns and 30.4 ns for measurements at proton energies of 62 MeV and 80 MeV, respectively, with corresponding widths of 10 ns and 12 ns.

The energies deposited by charged particles on the two detectors allow to produce identification (ID) maps mathematically described by the Bethe formula [8,9], where the bending radius of each ID depends on the charge and mass of the ion species. This makes particle identification possible, such as shown by the ΔE–E contour plot in Fig. 1. Here we can easily distinguish protons as main contributors to the most intense ID, which stands out from a structure-less background due to γ-rays. Above the proton signature, there are then other particles which are separated by the different charge and mass: deuterons, tritons, ^{3}He and α. The intensity of these signatures is however less pronounced than protons, as the lower interaction cross section compared to nuclear elastic scattering and higher stopping power in air, Al foils, and Si detector.

3.2. Measured pulse height spectra

Pulse height spectra (PHS) on the YAP scintillator were obtained after coincidence analysis. Fig. 2 shows the PHS with incoming protons at 62 MeV and 80 MeV without Al foils in front of the spectrometer. The most important feature of the PHS is the peak at the maximum pulse height position, that is the contribution of proton elastic scattering on carbon (Peak$_C$). The contribution of scattering on hydrogen (Peak$_H$) and inelastic scattering on carbon can also be observed. As Peak$_C$ has the highest energy and best resolution, we decided to use the position of this peak to determine the relative light yield of the YAP:Ce detector as a function of the incident proton energy (see Section 4.3). We can further notice that the shape of the peak is not Gaussian, as one would expect for a well collimated beam [6]. Detailed analysis reveals that it could be resulted by protons scattering on air (see Section 4.2). The statistical error on the PHS position Peak$_C$ is about 0.5%–2.3%.

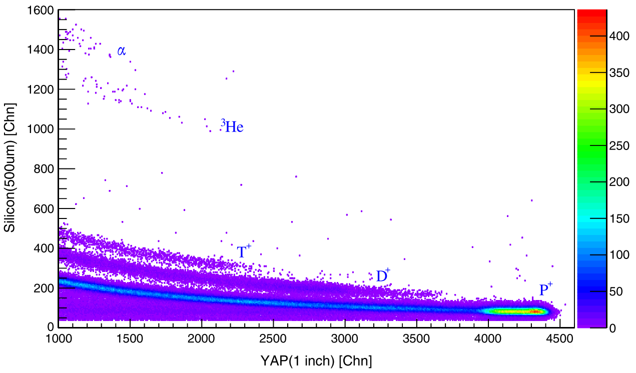

Fig. 1. $\Delta E - E$ contour plot of coincidence events measured by the TPR. Elongated structures ("bananas") due to particles produced from the interaction of protons with the polyethylene target can be clearly seen.

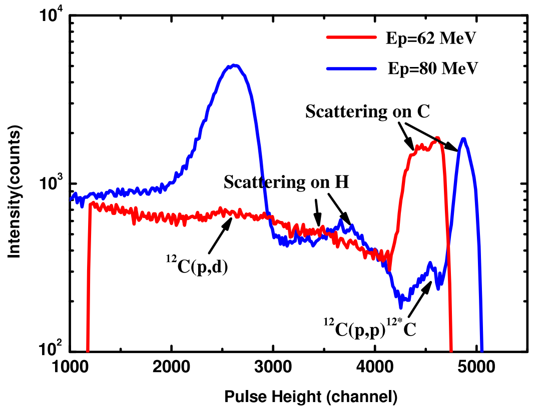

Fig. 2. Measured PHS on the YAP scintillator with 62 MeV and 80 MeV proton beams.

4. Analysis and results

4.1. Calculations of incident proton energy

Al foils of different thicknesses were placed in front of the TPR system to obtain a range of different proton energies on the TPR from the two beam energies (62 and 80 MeV) available with the cyclotron accelerator. The proton energy on the YAP scintillator after the Al foils was calculated with two independent methods that were found to be consistent. The first method was the simulation using the MCNPX code [10] with the la150h library [11]. This determines the transport of protons including scattering on the target and struggling in the Al energy degrader and air. With the second method, the energy of the scattered protons on carbon (on polyethylene) was derived analytically based on the kinematical scattering model. Proton energies lost in air, target, Al foils and silicon detector were determined based on the Pstar library [12]. The two methods provided consistent results within 1%.

4.2. PHS analysis

The PHS has been analyzed by fitting the highest energy peak with Gaussian functions. Fig. 3 shows an example of a fit for a measurement

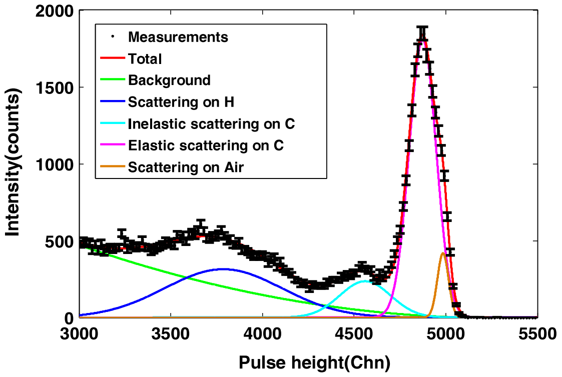

Fig. 3. Fit of the experimental data with different components that contribute to the measured spectrum, as indicated in the legend. An empirical polynomial fit is used to described the background.

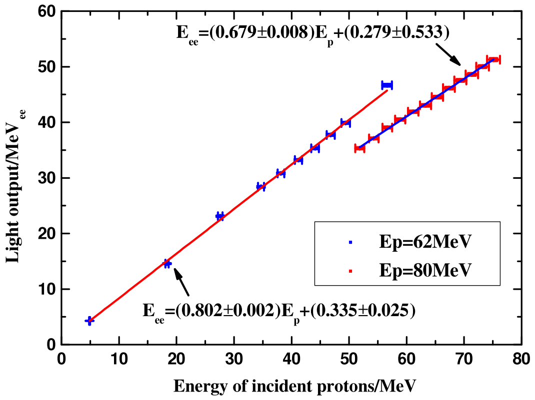

Fig. 4. ΔE–E contour plot of coincidence events measured by the TPR.

with 80 MeV protons. In the analysis of each PHS we considered components due to: (a) elastic scattering on carbon and on hydrogen; (b) inelastic scattering on carbon; (c) scattering on air and (d) a continuous background that is empirically described by a polynomial. The position of the ^{12}C elastic scattering peak is the most important parameter as it is used to determine the relative light yield (see Section 4.3). At an energy lower by 4.44 MeV with respect to the ^{12}C elastic scattering peak we then found a further peak from inelastic scattering on carbon, where the energy difference corresponds to the first excited state of the ^{12}C nucleus. As oxygen and nitrogen have higher masses than ^{12}C, scattering by air determines a barely visible peak at even higher energies than scattering on carbon.

Concerning the peak broadening, kinematics predicts wider peaks when scattering occurs on lighter elements. This is why the elastic scattering peak on hydrogen is significantly larger than that on ^{12}C.

4.3. Calibrations and light output

In order to obtain the relation between proton energy and relative light yield, we must provide the PHS with an energy scale. In our experiment we decided to adopt the equivalent electron energy (MeV_{ee}) scale, so that the light yield for protons at an energy E_p is expressed relative to γ-rays of same energy $E_\gamma = E_p$. To this end, we have calibrated the PHS with ^{137}Cs (0.662 MeV) and ^{60}Co (1.17 and 1.33 MeV) γ-ray sources prior to the proton measurements. A linear relation between pulse height in channels (Chn) and the electron equivalent energy (E_{ee}) $E_{ee} = 1.0523 \times 10^{-2} Chn - 0.02$, as determined by the γ-ray calibration, has been used to calibrate the PHS.

With this input, from the position of the ^{12}C elastic peak in the PHS and in MeV_{ee} units, we were able to determine the curve of the relative light yield of the YAP scintillator as a function of the proton energy, as shown in Fig. 4. We find that the relative yield is linear for the set of data obtained with beam energies of both 62 MeV ($R^2 = 0.9988$) and 80 MeV($R^2 = 0.9989$).

Even though the slopes differ for the two data sets, measurements obtained with a proton beam of 62 MeV show a relative light output of $(80.2 \pm 0.2)\%$, while measurements obtained with a proton beam of 80 MeV provide a relatively reduced light output of $(67.9 \pm 0.8)\%$. After an analysis of the possible causes we concluded that the problem was a shift of the PMT gain from the first to the second set of measurements, that were performed on different days. The calibrations with gamma sources were done on the same day as the first set of measurements, so it is reasonable to assume that the relative yield determined with these data is the most accurate. As changes of the PMT gain are important and have been already observed in the measurements reported in this paper, we have now implemented a LED source driven by an external pulser in the detector to monitor the long term stability of the PMTs for applications at ChipIr.

5. Conclusion

A YAP:Ce scintillator based TPR spectrometer has been tested using protons in the energy range 5 to 80 MeV by means of the cyclotron accelerator at INFN-LNS. Background rejection and particle discrimination capabilities have been successfully demonstrated using time coincidence and ΔE–E measurements. The relative light yield of the YAP scintillator was measured to be about 80% (with 10% uncertainty) with respect to γ-rays of same energy. Most importantly, the light yield scales linearly with the proton energy in the whole range we have tested. This demonstrates the possibility to use a YAP:Ce scintillator as the proton spectrometer in a TPR detector concept for measurements of the neutron spectrum up to 150 MeV at ChipIr.

Acknowledgments

This work has been carried out within the framework of PANAREA and has received funding support from the National Natural Science Foundation of China (Grant No. 11505216). The authors would like to thank the accelerator group at INFN-LNS for performing the irradiations.

References

[1] C.D. Frost, et al., 2009 IEEE International Reliability Physics Symposium, 2009, pp. 952–955.
[2] M.S. Gordon, et al., IEEE Trans. Nucl. Sci. 51 (6) (2004) 3427–3434.
[3] C. Cazzaniga, et al., Prog. Theor. Exp. Phys. (7) (2015) 073H01.
[4] C. Cazzaniga, et al., Nucl. Instrum. Methods A 751 (2014) 19–22.
[5] G.F. Knoll, Radiation Detection and Measurement, John Wiley & Sons, 2010.
[6] C. Cazzaniga, et al., Nucl. Instrum. Methods A 820 (2016) 85–88.
[7] C. Cazzaniga, et al., J. Instrum. 8 (11) (2013) P11008.
[8] H. Bethe, Ann. Phys. 397 (3) (1930) 325–400.
[9] D.E. Groom, et al., Eur. Phys. J. C 15 (1–4) (2000) 163–173.
[10] G. McKinney, et al., American Nuclear Society-Topical Meeting in Monte Carlo, 2005.
[11] M.B. Chadwick, LA-UR-99-1222.
[12] M.J. Berger, et al., http://physics.nist.gov/Star.